FUEL REFORMATION AND HYDROGEN GENERATION IN VARIABLE VOLUME MEMBRANE BATCH REACTORS WITH DYNAMIC LIQUID FUEL INTRODUCTION

A Dissertation
Presented to
The Academic Faculty

by

Thomas Myungyul Yun

In Partial Fulfillment
of the Requirements for the Degree
Doctor of Philosophy in the
School of Mechanical Engineering

Georgia Institute of Technology
May 2015

FUEL REFORMATION AND HYDROGEN GENERATION IN VARIABLE VOLUME MEMBRANE BATCH REACTORS WITH DYNAMIC LIQUID FUEL INTRODUCTION

Approved by:

Dr. Andrei G. Fedorov, Advisor
School of Mechanical Engineering
Georgia Institute of Technology

Dr. Peter A. Kottke
School of Mechanical Engineering
Georgia Institute of Technology

Dr. Caroline L. Genzale
School of Mechanical Engineering
Georgia Institute of Technology

Dr. Timothy C. Lieuwen
School of Aerospace Engineering
Georgia Institute of Technology

Dr. Christopher W. Jones
School of Chemical & Biomolecular Engineering
Georgia Institute of Technology

Date Approved: March 12, 2015

ACKNOWLEDGEMENTS

I would like to first acknowledge the support and guidance of my advisors, Dr. Andrei Fedorov and Dr. Peter Kottke, throughout both projects and my graduate career. While their academic guidance has been exemplary, it has been their patience, generosity, and genuine interests in my success and well-being for which I am truly grateful.

I have been very fortunate to have a great team at Multiscale Integrated Thermofluidics Research Lab at Georgia Tech. Many thanks to our terrific team members, especially to David Anderson for providing insightful suggestions on my research.

Lastly, I would like to thank my wife, Dr. Sunghye Chang, my lovely kids, Ellie and Colin and my parents Dr. Chung-Bang Yun and Heesuck Yun for their steadfast love, trust, and sacrifice throughout my graduate studies.

I acknowledge the support from NSF, GTRI, DARPA and the Georgia Institute of Technology though out my graduate studies for numerous funded projects.

TABLE OF CONTENTS

LIST OF TABLES

LIST OF FIGURES

LIST OF SYMBOLS AND ABBREVIATIONS

Symbols

A = reactor cross-sectional area

B = diffusion coefficient matrix for Maxwell Stefan derivation of diffusive flux

c_i = concentration of species *i*

$\bar{c}_v$ = molar specific heat constant volume

$\bar{c}_{pi}$ = molar specific heat of species *i*

D_{memb}= membrane permeability

D_{ij}= binary diffusion coefficient for species i and j

$\tilde{D}_{ij}$= Maxwell-Stefan diffusion coefficient for species i and j

D_{iM}= multi-component mass diffusion coefficient for species *i* in gas mixture

$D_{M,avg}$= average of multi-component mass diffusion coefficients

d_{cat}= catalyst layer thickness

d_{gap}= gap between membrane and permeation block for sweep gas flow

E_{in}= energy input

H = reactor height

h_i = enthalpy for species *i*

$h_{m\text{-}s}$ = heat transfer coefficient of convective flow of heated sweep gas over membrane

h_{film} = liquid film height

J_i = diffusive flux of species *i*

$J_{H2,Perm}$= H_2 yield

$\dot{J}_{H2,perm}$=rate of H_2 permeation through membrane

$J''_{H2,perm}$ =flux of H_2 permeation through membrane

K = evaporation constant

k_i = thermal conductivity of species i

L_{cat} =specific catalyst loading

$LHVi$ = lower heating value of species *i*

N_i = number of moles of species *i*

$\dot{N}_{sweep}$ = sweep gas flow rate

Nu = Nusselt number

P = pressure

p_i = partial pressure of species *i*

Q_{in} = heat input

R = gas constant

R_{drop} = radius of droplet
R_t = contact resistance between catalyst and membrane
$\dot{R}_{ıJ}$ = rate of mole change due to reactions
$r_j =$ rate of reactions for j
S_A = specific surface area of catalyst
Sh = Sherwood number
T = temperature
t = time
t_{cycle} = time for batch reactor cycle
U_p = piston velocity
$u_{fg,i}$ = internal energy for evaporation of species *i*
u_i = internal energy for species *i*
V = volume
v = velocity (molar based)
*v** = transformed velocity (molar based)
W_{in} = work input
x_{CH_3OH} = fuel conversion
Y_{H_2} = fuel conversion, and hydrogen yield efficiency
*z** = transformed coordinate for non-dimensionalized position

Greek symbols
δ_{memb}= membrane thickness
ε_{cat} = catalyst porosity
$\eta_{reformer}$ =efficiency of reformer efficiency
θ_{avg} = permeance reduction factor due to non H2 species
ρ_{cat} = catalyst density
τ = time scale
ω = volumetric power density
ΔH_j^o = heat of reaction j under standard state (25^{o}C and 1atm.)

Subscripts
i = H_2, CH_3OH, H_2O, CO_2, or CO
j = reactions (MSR/MD/WGS)
MSR = methanol steam reforming reaction
MD = methanol decomposition reaction
WGS = water gas shift reaction

max = Maximum
init = Initial
eff = effective
cat = Catalyst
memb = Membrane
ret = retentate side
C.V. = constant volume operation
C.P. = constant pressure operation
N = north
S = south
P = point
diff = diffusion
evap = evaporation
perm = permeation
rxn = reaction
m = methanol
w = water

Superscripts
n = new
o = old

Abbreviations
CFR : Continuous-Flow Reactor
CHAMP : CO2 H2 Active Membrane Piston
DDIR : Direct Droplet Impingement Reactor
PBMR: Packed Bed Membrane Reactor
MD : Methanol Decomposition
MSR : Methanol Steam Reforming
WGS : Water Gas Shift

SUMMARY

In recent years, the need for high performance power sources has increased dramatically with the proliferation of ultra-compact electronic systems for mobile communication, man-portable and versatile military equipment, and electric vehicles. Volume- and mass- based power density are two of the most important performance metrics for portable power sources, including hydrogen generating fuel reforming systems (onboard) for hydrogen fuel cells. Two innovative multifunctional reactor concepts, CO_2/H_2 Active Membrane Piston (CHAMP) and Direct Droplet Impingement Reactor (DDIR), are combined for the purpose of hydrogen generating fuel reforming system (onboard) for fuel cells. In CHAMP-DDIR, a liquid fuel mixture is pulse-injected onto the heated catalyst surface for rapid flash volatilization and on-the-spot reaction, and a hydrogen selective membrane is collocated with the catalyst to reduce the diffusion distance for hydrogen transport from the reaction zone to the separation site. CHAMP-DDIR allows dynamic variation of the reactor volume to optimally control the residence time and reactor conditions, such as pressure and temperature, thus improving both the reaction and separation processes.

A comprehensive CHAMP-DDIR model, which couples key physical processes including 1) catalytic chemical reactions, 2) hydrogen separation/permeation at membrane, 3) liquid fuel evaporation, and 4) heat and mass transport, has been developed to investigate the behavior of this novel reactor system, aiming at maximizing the volumetric power density of hydrogen generation from methanol/water liquid fuel. The relationships between system design parameters and the rate-limiting process(es), i.e., reaction, permeation, and transport, which govern reactor output, have identified. Experimental characterization of the prototype reactor has been performed for laboratory demonstration of the concept and model validation. Both model predictions and experiments successfully demonstrate the unique practical performance improvements of CHAMP-DDIR through combining time-modulated fuel introduction and the active change of reactor volume/pressure.

This work has led to a number of fundamental insights and development of engineering guidelines for design and operation of CHAMP-DDIR class of reactors, which can be extended to a broad range of fuels and diverse practical applications.

CHAPTER 1

INTRODUCTION

1.1 Motivation for Development of New Fuel Processing Reactor Concept

In recent years, the need for high performance power sources has increased dramatically with the proliferation of ultra-compact electronic systems for mobile communication, man-portable and versatile military equipment, and electric vehicles [1, 2]. Batteries have served as the main power source, partly because advances in portable electronics and improvements in the performance of batteries proceeded at roughly the same pace until the 1990s. However, the ability of batteries to meet more challenging demands has gradually decreased because of two significant shortcomings of battery technology: the relatively low weight-based energy density (150 to 250 Wh/kg for lithium-ion batteries [3], versus a need of approximately 1900 Wh/kg to compete with the gasoline internal combustion engine [4], for example) and relatively long-recharge times. These shortcomings have fueled a need for alternative high-energy-density portable power supplies [4-6]. One promising substitute for batteries is a hydrogen fuel cell using stored hydrogen as fuel, which offers energy densities ranging from 500 to 1,000 Wh/kg. Another even higher energy density alternative is use of hydrogen fuel cells with hydrogen fed from onboard fuel reforming of liquid hydrocarbons (5.6 kWh/kg for methanol and 12.6 kWh/kg for butane)[7, 8]. Hydrogen produced from the onboard reforming of liquid fuels can also be an efficient feed for internal combustion engines [9, 10]. Comparison of tank-to-wheel efficiencies (η_{TTW}) for a conventional internal combustion spark ignition engine and on-board fuel reforming (gasoline based) fuel cell powered (proton-exchange membrane FC) vehicle in recent study showed that the efficiency of fuel cell based vehicles (η_{TTW}=26.6%) are higher than that of the internal combustion engine ($\eta_{TTW,ICE}$=12.6%)[11]. In addition

to displaying inherent high-energy-density, mobile systems which exploit the onboard reforming of liquid fuels can take advantage of an existing infrastructure, and are thus suitable for fast and easy refueling [12, 13]. For instance in military and space applications, high energy density onboard power supply systems that meet stringent weight, volume, and power criteria are highly valued.

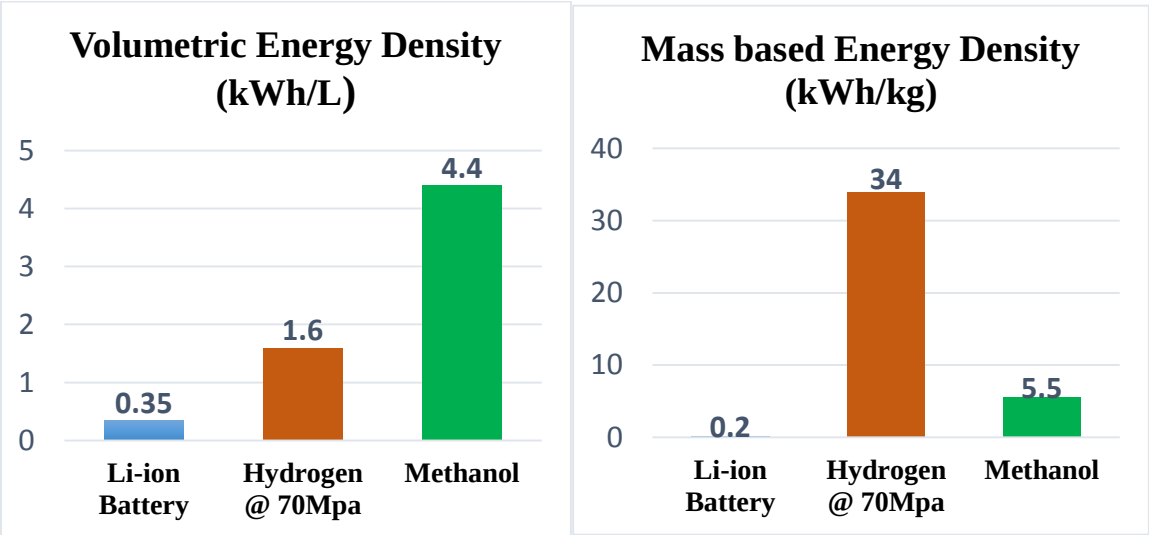

Figure 1.1 Volume and mass based energy density comparisons for power sources

Knowing that fuel reforming systems based on liquid fuel allow high energy density, it is important to identify the specific design which also provides high power density, both on a volume and mass basis, for mobile/portable applications. Therefore, development of a high power density fuel processor for production of hydrogen at relatively small-scales (<100kW) is the subject of the present work.

To achieve this goal, a new, dynamically-controlled reactor, which combines the variable volume operation of CHAMP (CO_2/H_2 Active Membrane Piston)[14, 15] with direct injection of liquid fuel of DDIR (Direct Droplet Impingement Reactor)[16, 17], is developed and analyzed. The primary goal is identification of conditions for the highest volumetric power (hydrogen yield) density. In the resulting CHAMP-DDIR, a liquid fuel mixture is pulse-injected onto the heated catalyst surface for rapid flash volatilization and

on-the-spot reaction, and a hydrogen selective membrane is collocated with the catalyst to reduce the diffusion distance for hydrogen transport from the reaction zone to the separation site[18, 19]. Uniquely, CHAMP-DDIR allows dynamic variation of the reactor volume to optimally control the residence time and reactor conditions (pressure and temperature), thus improving both the reaction and separation processes. Furthermore, the CHAMP-DDIR offers compelling opportunities to achieve the maximum volumetric power density as well as on-demand dynamic variation in hydrogen throughput without sacrificing fuel conversion.

As a case study for CHAMP-DDIR, this thesis focuses on methanol steam reforming, which is widely studied as one of the most viable methods for distributed hydrogen generation[20] because of its relatively mild reforming conditions. Of primary importance for reactor design is development of comprehensive regime maps showing how the controllable parameters translate to the particular mode of reactor operation and corresponding performance. This in turn is supported by experimental evidence showing the utility of these maps in CHAMP-DDIR design and operation.

1.2 Research Scope

We performed a comprehensive investigation of the CHAMP-DDIR reactor, a direct liquid fuel injection/variable volume batch reactor integrated with a hydrogen selective membrane. The overall research objective, of developing the necessary understanding of the processes driving reactor performance to ultimately determine the capability of this new reactor concept, was accomplished through the completion of three tasks:

Task 1. Develop a comprehensive theoretical framework of reactor operation, embodied in a series of reduced-order physical/mathematical models

In order to successfully establish a design methodology for this new class of reactors, it is important to first understand the underlying processes determining reactor performance. This thesis work focuses on understanding the complex interplay between fuel delivery, evaporation, heat/mass transport, reaction, and separation in a batch membrane reactor, under changing thermodynamic conditions. Theoretical analysis, development of mathematical models of increasing complexity, and simulations are performed to gain fundamental insights into interactions among relevant transport, separation, and reaction phenomena.

Task 2. Using a prototype CHAMP-DDIR, obtain experimental validation of model predictions to support process improvement via CHAMP-DDIR operation

The prototype CHAMP-DDIR consists of an actively-controlled micro injector for liquid fuel atomization, a dynamically-modulated reactor volume, and hydrogen selective membrane. It is used for hydrogen production via the methanol steam reforming reaction. The prototype reactor demonstrates the ability to realize performance improvement through two modes of CHAMP-DDIR operation: (i) pulse-modulated fuel injection and (ii) batch reaction with dynamically-adjusted reactor volume. The impact on performance of the different modes is quantified. The experimental results obtained with the prototype also demonstrate a need for a more rigorous model for accurate exploration of the design and operation space. The prototype reactor results are used to explore the accuracy of the more comprehensive reactor model through comparison of predicted and measured hydrogen production rate, reactor pressure, and temperature.

Task 3. Using an experimentally validated model, perform a detailed study of the reactor parametric space and operating regimes

The experimentally validated model is used to identify the relationship between CHAMP-DDIR design and operating parameters and the rate-limiting processes that govern reactor output. As part of this process, the role of effects of heat and mass transfer limitations on

CHAMP-DDIR performance are investigated by comparing the predictions among multiple cases with varying levels of idealization or approaches to approximation of actual transport behavior. Ultimately, design maps are established in terms of key reactor process variables, such as pressure, temperature, dynamic fuel feed rate, catalyst loading, membrane characteristics, and reactor dimensions, with power density as the performance metric. These maps define operating regimes and identify the dominant parameters that govern transitions between regimes.

1.3 Overview of Chapters

Chapter 2 reviews the state-of-the-art in portable fuel reforming hydrogen production technologies. Several shortcomings of these technologies are described and the new CHAMP-DDIR is explained with a focus on how it addresses those shortcomings. Additionally, the key underlying physical processes of CHAMP-DDIR (fuel evaporation, species transport, catalytic reaction, and selective permeation) are defined and operational procedures are discussed.

In chapter 3, two theoretical reactor models for CHAMP-DDIR analysis were investigated. First, idealized CHAMP-DDIR simulations, without heat and mass transfer limitations in the reactor volume, are used to determine the theoretical limits on power density for various operational conditions. Second, a CHAMP-DDIR model which accounts for the effects of mass transport limitations and bulk temperature changes in time, is employed to evaluate possible performance improvement through combining time-modulated fuel introduction and the active change of reactor volume.

In chapter 4, CHAMP-DDIR is experimentally demonstrated. Two unique modes of CHAMP-DDIR operation, pulse-modulated fuel injection and batch reaction with dynamically-adjusted reactor volume, are investigated, and their performance quantified

using metrics such as hydrogen yield and volumetric power density. Performance quantification from measurement is via comparison with a conventional batch reactor.

In chapter 5, a comprehensive reactor model which carefully considers the effects of heat and mass transfer, including rigorous treatment of multi-component species diffusion, is presented. The model is validated against experimental results through comparison of predicted and measured hydrogen production rate, reactor pressure, and temperature. The experimentally validated model is used to identify the relationship between CHAMP-DDIR design and operating parameters and the rate-limiting processes that govern reactor output. In addition, effects of heat and mass transfer limitations on CHAMP-DDIR performance are investigated by comparing the predictions among multiple cases with increasing level of complexity used for modeling the transport phenomena within the reactor.

Lastly, chapter 6 outlines the recommended directions of future efforts and defining the areas requiring further development. This chapter concludes with a statement of the original contributions of this work to the field of portable fuel reforming and summarizes the key conclusions drawn from both the experimental and modeling work.

CHAPTER 2

PORTABLE FUEL REFORMING AND DEVICE CONCEPT

The state-of-the-art in portable fuel reforming hydrogen production technologies is reviewed in this chapter. Several shortcomings of these existing technologies are identified and the new multifunctional reactor CHAMP-DDIR concept is introduced with a focus on how it addresses those shortcomings of previous fuel reforming devices. In addition to illustrating distinguished practical benefits of CHAMP-DDIR, the key underlying physical processes of CHAMP-DDIR (fuel evaporation, species transport, catalytic reaction, and selective permeation) are defined and operational procedures are discussed.

2.1 Review of Portable Power Sources and Hydrogen Generation

Some of the key requirements for a fuel reforming reactor for portable applications are (i) high power density (both volume and mass based)[20-22], (ii) ability to operate with dynamically varying hydrogen throughput without sacrificing conversion efficiency [23] and (iii) rapid start-up/ shut-down (i.e. low temperature and effective mass/heat transport)[24, 25]. These requirements for portable applications stand in contrast to the main concerns for large industrial-scale fuel reforming chemical plants, for which the focus is on maximizing the energy conversion efficiency and minimizing the cost [22]. This fundamental difference in objectives leads to drastically different approaches to reactor design. Multifunctional reactors, which synergistically combine different unit processes [26, 27] are attractive approaches to achieve the objectives of small-scale fuel reformers.

2.1.1 Fuel processing technology for hydrogen generation

The three most common catalytic reactions used for processing hydrocarbons and hydrogen generation fuels are (i) partial or preferential oxidation, (ii) autothermal reformation, and (iii) steam reforming [10, 28]. Partial/preferential oxidation and autothermal reformation

both introduce air into the fuel stream, and the fuel/air mixture reacts exothermally, producing the heat required for the reforming reaction to occur. The steam reforming reaction is endothermic and requires an external heat input. While each technology offers its own advantages [29-31], catalytic steam reforming provides benefits over other methods, because it offers the highest theoretical hydrogen yield (per mole of fuel), requires moderate operating temperatures for catalysis, and avoids dilution with excess nitrogen, thus improving efficiency of separating H_2 from the products [28, 31]. In addition, capturing the byproduct CO_2 can be most efficient with steam reforming, the reformate stream is highly enriched in CO_2 (and amenable to capture), especially when hydrogen from the product is separated (i.e. membrane reactor).

2.1.2 Methanol steam reforming

Methanol is widely studied as one of the most viable fuels for producing hydrogen, especially in portable/distributed applications, due to the following advantages: it reforms in mild reaction conditions (low temperature), it does not require desulfurization; and, it is more easily transported than methane or other gaseous fuels [32-34]. Attractively, catalytic conversion of methanol to hydrogen occurs at moderate temperatures for such reactions as partial oxidation (200-230 °C), steam reforming (200-300 °C), and methanol decomposition (up to 400 °C). Although energy density of methanol is not as high as some other fuels, such as butane or gasoline (those fuel can be more beneficial than methanol when reformed through partial oxidation), for steam reforming reactions which require water as part of the fuel stream, total energy density of fuel water mixture is higher than those for butane or gasoline [35]. Of particular interest, the steam reforming of methanol yields the highest moles of hydrogen per mole of fuel (compared to other reforming pathways), and occurs via the following overall endothermic reactions over well-developed and inexpensive catalysts (e.g. $CuO/ZnO/Al_2O_3$, $CuZrO_2$, and Cu/ZnO) [36]. The methanol steam reforming (MSR) reaction is given by Eq. (2.1),

$$CH_3OH + H_2O \rightleftharpoons 3H_2 + CO_2, \ \Delta H^o_{MSR} = 49.2 \text{ kJ/mol} \quad (2.1)$$

Methanol decomposition (MD), Eq. (2.2), and the water gas shift reaction (WGS), Eq. (2.3), are two additional reaction pathways that occur concurrently with methanol steam reforming:

$$CH_3OH \rightarrow 2H_2 + CO, \ \Delta H^o_{MD} = 90.4 \, kJ/mol \quad (2.2)$$

$$H_2O + CO \rightleftharpoons H_2 + CO_2, \ \Delta H^o_{WGS} = -41.2 \, kJ/mol \quad (2.3)$$

It should be noted that three reactions in Eqs. (2.1)-(2.3) are not thermodynamically independent since reaction (2.1) is the sum of the other two reactions.

2.1.3 Requirements for portable / small-scale fuel processing devices

For fuel reforming systems, there are several important performance requirements, including ease of operation, high fuel conversion, high energy conversion efficiency, low cost, compactness of balance-of-plant components, and high selectivity to hydrogen [22, 35, 37, 38]. For component level design, power density is among the most important metrics and is the focus of this analysis. For system level design, other metrics should also be considered, such as energy density [39]. The dominant design objective of maximizing power density for portable applications is in contrast to the main concern for large-scale fuel reforming chemical plants, for which the focus is on maximizing the energy conversion efficiency and minimizing the cost. This fundamental difference in objectives leads to drastically different approaches to optimal design and operation of reactors.

2.1.4 Portable MSR reactors for power density maximization

Several reports have discussed methanol steam-reforming fuel flow reformers in the context of power density or related criteria, such as the reactor size or hydrogen productivity. The packed-bed Pd membrane reactor (PBMR) model simulations by Harold and Nair revealed that the hydrogen productivity (rate of permeate hydrogen produced per reactor volume) achieves a maximum value at an intermediate value of a space velocity

(flow rate of fuel per reactor volume), implying, a trade-off between reactor size, fuel conversion and hydrogen production [40, 41]. This study also showed evidence for hydrogen productivity being affected by different rate limiting processes: permeation limited by the dependence on the Pd membrane thickness; or reaction limited by variation in catalyst loading (amount of catalyst per unit amount of reactant). Another study of PBMR by Israni et al. found that both hydrogen utilization and productivity increase with temperature and retentate pressure [42]. In addition, the study also revealed that the hydrogen productivity increases with decreased inlet space velocity until the methanol conversion approaches 100%, after which a further reduction in space velocity has negative effect on productivity (since the reactor volume is not fully utilized). Varady et al. performed a parametric study of an isothermal plug-flow methanol steam-reforming reactor and found a similar correlation in which increasing power density comes at a cost of reduced fuel conversion and energy efficiency [17]. All these studies provide important insights into the relationship between power density and other performance metrics, such as hydrogen yield, fuel conversion, hydrogen utilization, and energy efficiency.

2.2 Review of Reactor Design Concept

2.2.1 Multifunctional reactors

Multifunctional reactors, which synergistically combine different unit processes executed in a single or a few components, are a notable approach to achieve power density maximization. Examples of multifunctional reactor design include (i) membrane reactors, where selectively removing hydrogen results in increased rates of production as well as a pure hydrogen stream [43-45], (ii) microchannel reactors with wall-coated catalyst, where catalyst activity is enhanced and reactant/product transport limitations are minimized [46, 47], (iii) heat exchanger reactors, where heat transfer is enhanced by efficient coupling of

heat sources [48-51], and (iv) “direct” liquid fuel conversion reactors, where the external vaporizer is eliminated without sacrificing the high energy storage density of liquid fuel [52].

The design of high power density reformers requires innovative combinations of multifunctional components that (i) reduce the reactor volume by utilizing high-energy density fuel, i.e., fuel in liquid phase [5, 53], (ii) minimize the number of balance-of-plant components and mitigate heat and mass transfer limitations [20, 26], (iii) promote desired catalytic reactions by controlling the residence time and thermodynamic state (pressure, temperature, and species concentrations) [54], and (iv) remove products via species-selective separation to achieve conditions for a desired shift in reaction equilibrium [40, 45]. The direct droplet impingement reactor (DDIR) was introduced by Salge and Schmidt for hydrogen generation from a variety of liquid fuels through high-temperature catalytic oxidation [52, 55], and was subsequently extended by Varady and Fedorov to portable methanol steam reforming applications [16, 17, 56]. It is a notable example of the first two above mentioned approaches - DDIR is a multifunctional reactor which exploits introduction of an atomized liquid fuel directly onto the heated catalyst such that fuel droplets rapidly vaporize upon contact and react on the same catalyst surface to form the desired products. Similarly, the $\underline{C}O_2/\underline{H}_2$ $\underline{A}$ctive $\underline{M}$embrane $\underline{P}$iston (CHAMP) concept, which is a batch-membrane reactor with variable volume that operates in a transient mode, takes advantage of new ideas of dynamic catalytic reaction control to achieve the third and fourth objectives [14, 15, 57, 58]. The capability of CHAMP to actively change the reactor volume throughout the fuel conversion cycle enables optimal control of residence time and reactor conditions (pressure and temperature), thus improving both the reaction and separation processes.

2.2.2 Direct Droplet Impingement Reactor (DDIR)

Figure 2.1 shows a schematic of a DDIR. The main innovation of DDIR is the introduction of atomized liquid fuel directly onto the heated catalyst layer such that fuel droplets rapidly vaporize upon contact and react on the same catalyst surface to form the desired products. One of the important benefits of DDIR compared to a microchannel-based reactor is that problems with pressure oscillation and flow rate variation are circumvented in the DDIR by avoiding two-phase microchannel flow, which is difficult to control. The original work on DDIR by Varady and Fedorov was driven by the need i) to develop a basic understanding of liquid fuel reforming, including models of droplet transport, impingement, and vapor phase transport/ reaction and ii) to validate the model predictions with supporting experiments on a unit cell reactor performed with precise control over droplet characteristics [16, 17]. The analysis was conducted for a single unit cell of the fixed catalyst bed reactor in a steady-state operation and droplet transport, impingement, and vapor transport were assumed to occur sequentially and independently for simplification of the analysis. In the study, an in-depth investigation of each process was performed and sub-models of these processes were validated with experiments and predictions from literature [59-62]. Ultimately, the comprehensive reaction-transport model provided increased insight into the influence of critical DDIR parameters, such as the unit cell aspect ratio, throughput, droplet size, delivery rate, impingement location, and heat losses, on reactor performance.

The validity of an assumption of instantaneous fuel evaporation is supported by the results of the original DDIR study by Varady and Fedorov[16], which considered the different modes of fuel evaporation including partial or complete in-flight droplet evaporation and vaporization of the fuel film accumulated on the surface of the heat catalyst layer upon impingement.

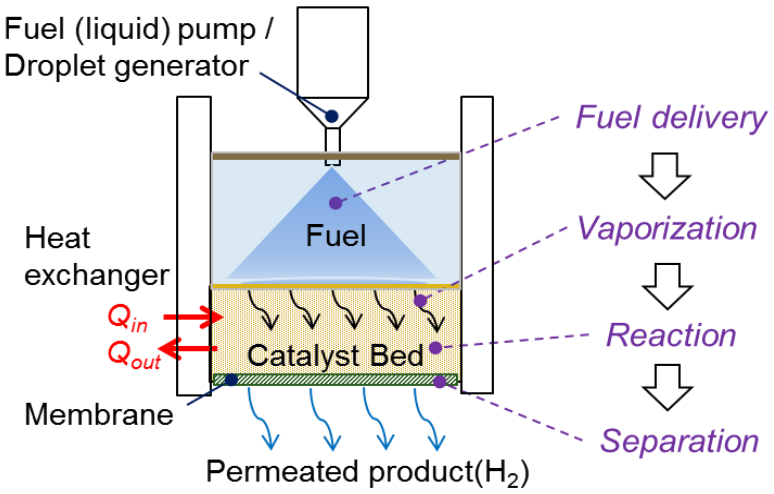

Figure 2.1 Schematic of Direct Droplet Impingement Reactor (DDIR)

2.2.3 CO2/H2 Active Membrane Piston (CHAMP)

Figure 2.2 shows a schematic of a CHAMP reactor. It is a batch-membrane reactor with variable volume that operates in a transient mode. In contrast to conventional continuous-flow reactors (CFR) that run in a steady-state mode, a unique feature of the CHAMP approach is in an active change of the reactor volume that enables precise control of reactor pressure and temperature throughout the fuel conversion cycle. This attribute allows for optimal control of residence time and reactor conditions to improve the reaction kinetics, transport, and separation processes. CHAMP reactors also incorporate membranes that shift the reaction equilibrium in a favorable direction by selective removal of reaction products from the reaction chamber, resulting in an increase in the fuel reforming and water-gas shift reaction rates and a high-purity hydrogen stream for power generation by the fuel cell or an IC engine. Damm and Fedorov studied the ideal performance (i.e. with no transport limitations) of a CHAMP reactor and compared it with that of an ideal CFR for methanol steam reforming hydrogen production [14]. In their study, simplified models of the CHAMP reactor showed its superiority to a CFR reactor in terms of hydrogen yield efficiency and fuel conversion. The performance enhancement of CHAMP over CFR is achieved by trapping the mixture in the reaction chamber and applying active control of

reactor pressure to enhance permeation of hydrogen. The other important benefits for CHAMP reactor are the possibility for on-demand dynamic variation in hydrogen throughput without sacrificing fuel conversion and production of a pure hydrogen stream (without CO content) permeating from hydrogen selective membrane.

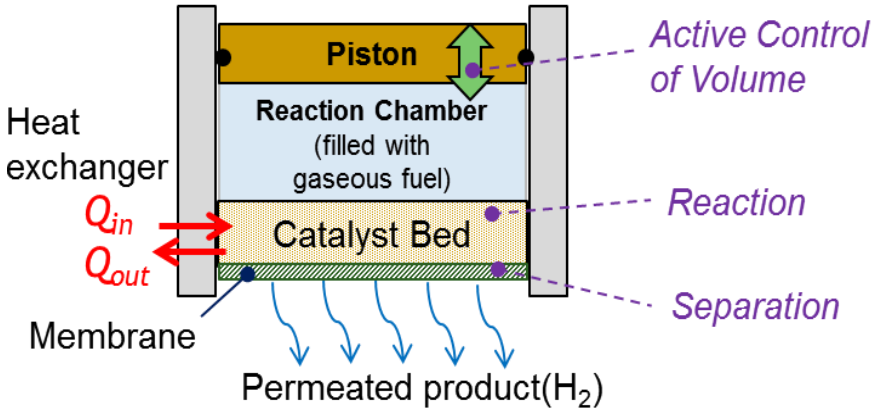

Figure 2.2 Schematic of CO2/H2 Active Membrane Piston reactor (CHAMP)

2.3 CHAMP-DDIR

Both DDIR and CHAMP prototype reactors have been built on the laboratory scale to demonstrate the advantages and practicability of each reactor concept. Furthermore, the key benefits of both CHAMP and DDIR have been experimentally validated [14-17]. Synergistically combining the unique advantages of each reactor concept in an integrated CHAMP-DDIR reactor is thus feasible and motivates theoretical and experimental studies of this new fuel processing approach with the potential to achieve the superior power density of hydrogen generation.

Motivated by the potential benefits of combining the CHAMP approach with DDIR for high power density fuel processing, the focus of this dissertation is an investigation of this new multifunctional reactor for hydrogen generation via liquid carbon-based fuel reforming for small-scale distributed power applications. CHAMP-DDIR combines direct

droplet impingement and on-contact rapid evaporation/reaction of fuel on a heated catalyst with a variable volume batch reactor integrated with hydrogen selective membrane aiming to achieve the maximum volumetric power density, as well as on-demand dynamic variation in hydrogen throughput without sacrificing fuel conversion.

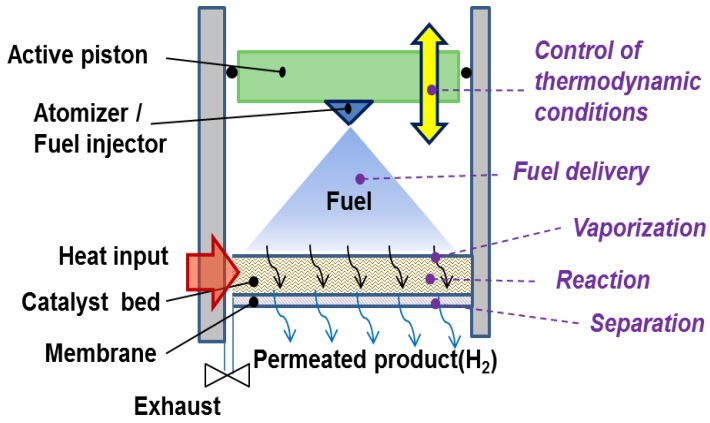

Figure 2.3 A basic embodiment of CHAMP–DDIR reactor.

A basic configuration of the CHAMP-DDIR is depicted in Figure 2.3. The atomizing nozzle for fuel dispersion is integrated with the active piston, whose motion enables precise control of reactor thermodynamic conditions throughout the fuel conversion cycle. This attribute allows for optimal control of residence time and reactor conditions to improve the reaction kinetics, transport, and separation processes. The catalyst layer is placed on the opposite side of the reactor chamber from the moving piston, and heated with an external heat source. The amount of heat supplied should be sufficient to evaporate the liquid fuel mixture rapidly and to drive endothermic reactions. Underneath the catalyst layer, a hydrogen selective membrane is incorporated. The in-situ hydrogen separation at the membrane shifts the equilibria of reversible reactions, i.e., MSR, Eq. (2.1) and WGS, Eq. (2.3), towards more hydrogen production, increasing forward rates for both reactions while providing a high-purity hydrogen stream for power generation by a fuel cell or an internal combustion engine.

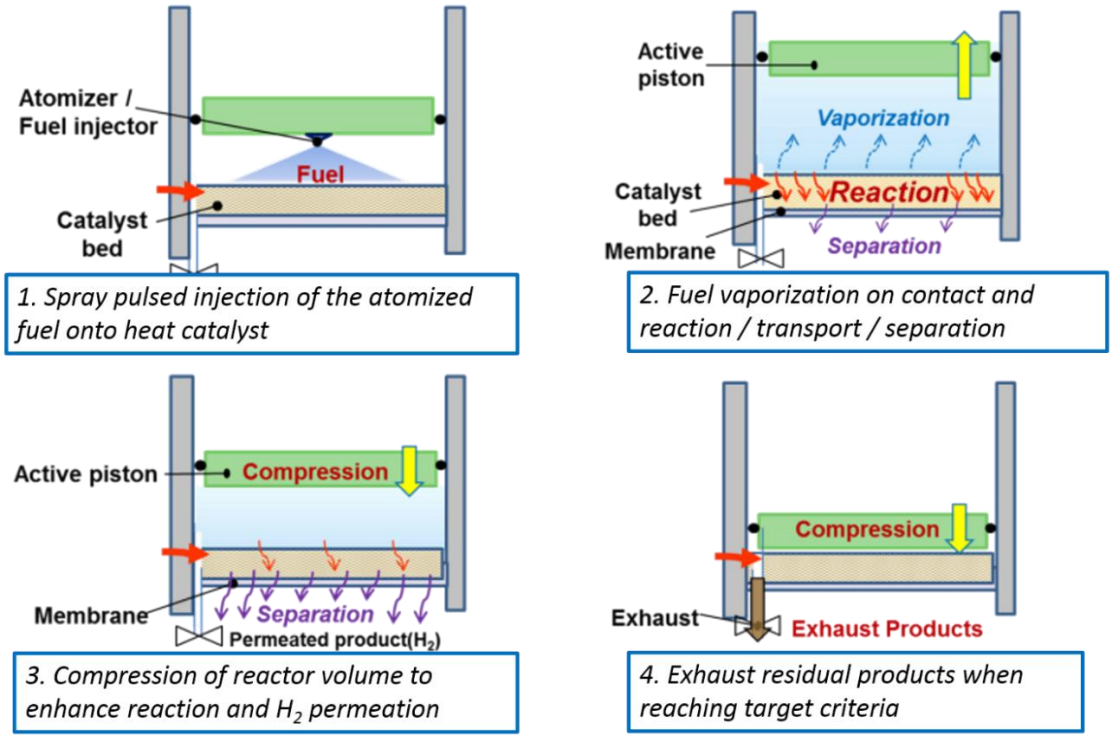

Figure 2.4 Four sequential stages during a cyclic operation of CHAMP-DDIR. The key underlying physical processes include fuel evaporation, species transport, catalytic reaction, and selective permeation under dynamic variation of thermodynamic conditions.

The four sequential steps in a CHAMP-DDIR cycle are depicted in Figure 2.4.

(1) The liquid reactant mixture drawn from a fuel reservoir is atomized to directly impinge on the heated catalyst surface. The fuel can be injected in pulses of varying frequencies and duty cycle during the reaction to control the total amount and temporal distribution of fuel introduction. This pulse-modulated injection benefits reactor performance by promoting efficient evaporation of fuel, maintaining the elevated temperature for enhanced reaction/permeation. It further allows for a smaller reactor volume to accommodate a given fuel amount without exceeding pressure limits [19].

(2) Flash volatilization of the injected fuel occurs on the heated catalyst surface. At the same time, the vaporized fuel reforms to generate hydrogen which permeates through the selective-membrane. As reactions and permeation progress, total pressure in the reaction

chamber continuously varies in response to change in total number of moles for all species, chamber volume, and temperature.

(3) Anytime during the cycle, the reactor chamber can be compressed to increase the concentration of remaining reactants and products. Thus pressure can be temporally controlled to provide enhanced driving force for the permeation process, resulting in maintaining the hydrogen throughput of the reactor at an increased level. As a result, on-demand control of residence time (cycle time) and thus the hydrogen yield rate can be achieved via volume modulation.

(4) Once the reaction and separation processes reach target levels (such as meeting desired hydrogen yield or fuel conversion criteria), the remaining gases are exhausted from the reaction chamber to complete the cycle.

2.4 Conclusions

A compact and efficient (high volumetric power density) power source is a critical component for most portable and mobile devices. One promising portable power source is a fuel cell fueled by hydrogen produced from the onboard reforming of liquid fuels. Multifunctional reactors, which synergistically combine different unit processes executed in a single or a few components, are a demonstrated approach to achieve power density maximization.

In this chapter, a new multifunctional reactor concept, CHAMP-DDIR, is introduced, which synergistically combines the unique advantages of two multifunctional reactor concepts, (i) CHAMP; variable volume batch style membrane reactor, and (ii) DDIR; on-contact rapid evaporation/reaction on catalyst via direct liquid fuel injection. The combined CHAMP-DDIR aims to achieve the maximum volumetric power density, as well

as on-demand dynamic variation in hydrogen throughput without sacrificing fuel conversion.

Theoretical and experimental investigation of this new multifunctional reactor for hydrogen generation via liquid carbon-based fuel reforming for small-scale distributed power applications will be discussed in the next chapters.

CHAPTER 3

REACTOR PERFORMANCE METRICS AND MODELING METHODOLOGY

This chapter presents the modeling approach of the CHAMP-DDIR to assess its achievable power density via variable volume operation and direct liquid fuel introduction. Two theoretical reactor models for CHAMP-DDIR analysis were investigated in this chapter. First, idealized CHAMP-DDIR simulations, without heat and mass transfer limitations in the reactor volume, are used to determine the theoretical limits on power density for various operational conditions. Second, a CHAMP-DDIR model which accounts for the effects of mass transport limitations and bulk temperature changes in time, is employed to evaluate possible performance improvement through combining time-modulated fuel introduction and the active change of reactor volume. Prior to introducing the detailed model, metrics of reactor performance will be reviewed followed by the discussion for fundamental physical processes occurring in CHAMP-DDIR. Then both models are introduced including their assumptions, governing equations, and boundary/initial conditions. Finally, the results of the theoretical analysis are presented and discussed to validate the claimed conceptual advantages of CHAMP-DDIR.

3.1 Metrics of Reactor Performance

A compact, efficient, and high performance power source has become a critical component for most portable and mobile devices, as power consumption in small-scale devices has increased dramatically [1, 5]. Similarly, for power sources which use hydrogen as a fuel (e.g., PEM fuel cells), a compact and efficient fuel reformer is needed to convert high energy density liquid fuel into hydrogen [53, 63]. In particular, power density (on both per unit mass- and volume basis) is one of the most important metrics for portable fuel

processors. Therefore, volumetric power density will be the main metric of reactor performance in this study. Other important metrics are hydrogen yield efficiency and fuel (methanol) conversion.

3.1.1 Volumetric power density

For the cyclic operation of the batch CHAMP-DDIR reactor, volumetric power density based on a conversion cycle, ω is defined in Eq. (3.1)

$$\omega = \frac{J_{H_2,perm} LHV_{H_2} - \mathrm{E_{in}}}{\mathrm{V}_{max} \cdot t_{cycle}} \tag{3.1}$$

Volumetric power density for a cycle is defined as the difference of the total number of moles of hydrogen that permeate out of the reactor (H_2 yield), $J_{H_2,perm}$, multiplied by the lower heating value of hydrogen, LHV_{H2}, and the total energy input to the system, E_{in}, all divided by the product of the maximum reactor volume during the cycle, V_{max}, and the cycle period, t_{cycle}. This calculation of power density is similar to the definition of thermal efficiency of a reformer introduced by Lutz $\eta_{reformer} = (J_{H_2,perm} LHV_{H_2} - \mathrm{Q_{in}})/ N_{\mathrm{Fuel}} LHV_{\mathrm{Fuel}}$ [64]. The total energy input during a cycle, E_{in}, is a combination of both external work input, W_{in} by piston compression, and heat input, Q_{in}, for evaporating the liquid fuel mixture, driving the reactions, and maintaining reactor temperature.

In cases when hydrogen conversion efficiency specific to power conversion systems (e.g. hydrogen fuel cell, combustor) needs to be accounted for, it can be used as a multiplier of the term $J_{H_2} LHV_{H_2}$ in Eq. (3.1), thus effectively reducing the realized power density. In addition, the volume and efficiency of balance-of-plant (BOP) components are not included in our calculations of power density, with an implicit assumption that the BOP components are not bottlenecks in achieving high power density hydrogen generation and can be selected to support a chosen optimal reactor design/operation. The discussion of BOP considerations in CHAMP-DDIR system is expanded in Appendix. A.

3.1.2 Hydrogen yield efficiency

The H_2 yield efficiency is the ratio of actual hydrogen yield ($J_{H_2,perm}$) to the ideal quantity of hydrogen that could be generated from fuel mixture. The H_2 yield efficiency can also be expressed as the product of fuel conversion, hydrogen selectivity, and hydrogen recovery. For the steam-reforming chemistry studied here, i.e., described by reaction Eqs. (2.1)-(2.3), the ideal hydrogen yield is three times the initial quantity of methanol, and thus the H_2 yield efficiency is given by

$$Y_{H_2} = J_{H_2.perm}/3N_{CH_3OH,init} \tag{3.2}$$

3.1.3 Fuel conversion

Fuel conversion is the ratio of extent (in moles) of methanol converted ($N_{CH_3OH,init} - N_{CH_3OH,final}$) via chemical reactions to initial moles of methanol ($N_{CH_3OH,init}$).

$$x_{CH_3OH} = 1 - N_{CH_3OH,final}/N_{CH_3OH,init} \tag{3.3}$$

3.2 Model Formulations for Individual Processes in CHAMP-DDIR

In order to successfully establish a design methodology for this new class of reactors, it is important to first understand the underlying processes determining reactor performance. These processes include liquid fuel introduction and evaporation, heterogeneous catalytic reactions, species transport, and separation, which are all coupled in the transient operation of CHAMP-DDIR. Concurrent, multi-dimensional analysis of all these processes can lead to a computationally expensive model. In addition, such a model could be too convoluted, so that it may offer little information about process controlling parameters. Therefore, a series of reduced-order models are constructed which combine sub-models for fundamental processes. Individual theoretical models for reaction kinetics, hydrogen permeation at membrane, and liquid fuel evaporation (which are commonly applied to all CHAMP-DDIR

models in this study) will be discussed in this section, and modeling of transport process will be discussed separately where each reactor model is introduced.

3.2.1 Reaction kinetics

This study is focused on conversion of methanol to hydrogen which take place via steam reforming over a $Cu/ZnO/Al_2O_3$ catalyst. Of the numerous kinetic studies and kinetic models for methanol steam reforming (MSR), methanol decomposition (MD), and water-gas-shift (WGS) reactions are available in the literature, e.g., [65-67], the kinetics model of Peppley et al., Eqs. (3.4)-(3.6), was chosen for this work due to its demonstrated utility and extensive experimental validation. In particular, the empirical model parameters were developed over a range of temperatures (160 $^oC < T < 260^oC$), pressures (1 atm < P < 10 atm), and methanol conversion (4-100%) that encompasses the expected CHAMP-DDIR operational range [68]:

$$r_{MSR} = \frac{k_{sr} K^*_{CH_3O^{(1)}} \left(p_A / p_D^{1/2}\right)\left(1 - p_D^3 p_C / K_{sr} p_A p_B\right) C_{S_1}^T C_{S_{1a}}^T}{\left(1 + K^*_{CH_3O^{(1)}} \left(p_A / p_D^{1/2}\right) + K^*_{HCOO^{(1)}} p_C p_D^{1/2} + K^*_{OH^{(1)}} \left(p_B / p_D^{1/2}\right)\right)\left(1 + K^{1/2}_{H^{(1a)}} p_D^{1/2}\right)} S_A \quad (3.4)$$

$$r_{MD} = \frac{k_d K^*_{CH_3O^{(2)}} \left(p_A / p_D^{1/2}\right)\left(1 - p_D^2 p_F / K_d p_A\right) C_{S_2}^T C_{S_{2a}}^T}{\left(1 + K^*_{CH_3O^{(2)}} \left(p_A / p_D^{1/2}\right) + K^*_{OH^{(2)}} \left(p_B / p_D^{1/2}\right)\right)\left(1 + K^{1/2}_{H^{(2a)}} p_D^{1/2}\right)} S_A \quad (3.5)$$

$$r_{WGS} = \frac{k_{wgs} K^*_{OH^{(1)}} \left(p_F p_B / p_D^{1/2}\right)\left(1 - p_D p_C / K_{wgs} p_F p_B\right)\left(C_{S_1}^T\right)^2}{\left(1 + K^*_{CH_3O^{(1)}} \left(p_A / p_D^{1/2}\right) + K^*_{HCOO^{(1)}} p_C p_D^{1/2} + K^*_{OH^{(1)}} \left(p_B / p_D^{1/2}\right)\right)^2} S_A \quad (3.6)$$

In Eqs. (3.4)-(3.6), the *k*'s are the Arrhenius rate constants [m^2/s-mol], *K*'s are equilibrium constants, *C*'s are surface concentrations of adsorption sites [mol/m^2], S_A is the specific surface area of the catalyst [m^2/m^3], and *p*'s are partial pressures of each of the species [bar] (A = CH_3OH, B = H_2O, C = CO_2, D = H_2, and F = CO) [68].

3.2.2 Hydrogen permeation through selective membrane

Hydrogen flux is calculated using the model for hydrogen permeation across a Pd-Ag membrane developed by Israni et al.[69]. The model assumes that diffusion of H atoms through Pd-Ag lattice is the rate limiting process for the transport of H_2 across the membrane (i.e., follows Sievert's Law) and accounts for the reduction of permeance due to adsorption of other than H_2 species (CH_3OH, H_2O, CO_2, and CO) on the membrane surface:

$$J''_{H2,perm} = \frac{D_{memb}}{\delta_{\text{memb}}} \theta_{avg} \left(p^{0.5}_{ret,H2} - p^{0.5}_{perm,H2} \right) \tag{3.7}$$

In Eq. (3.7), membrane permeance, $\frac{D_{memb}}{\delta_{\text{memb}}}$, is a function of temperature and membrane thickness, and the permeance reduction factor, θ_{avg} is 1 when membrane is exposed to pure hydrogen and decreases with an increase of non-hydrogen species partial pressures owing to the competitive adsorption of the available membrane surface sites[69]. In the original model by Israni et al., the multiplier θ is semi-empirically found based on steady-state behavior, and so can only be approximately applied to dynamically varying CHAMP-DDIR operation. Since transient effects of adsorption for non-H_2 species on Pd-Ag membrane surface are not known, a time average value, θ_{avg}, is used in the current reactor membrane model.

Hydrogen flux is also proportional to the difference in square root of hydrogen partial pressures on either side of the membrane (retentate side $P_{ret,H2}$ and permeate side $P_{perm,H2}$). Partial pressure of hydrogen on the permeate side is determined by mass conservation for the control volume at the permeate side of membrane assuming that permeated hydrogen is perfectly mixed with sweeping gas that introduced at a constant flow rate. (See Appendix B for $p_{perm,H2}$ calculation.)

3.2.3 Evaporation of liquid fuel during injection

Based on the previous DDIR studies by Varady and Fedorov, fuel droplet evaporation in DDIR can occur in two modes: (i) in-transit during the fuel droplets traveling from the fuel injector to the catalyst layer and (ii) on the catalyst surface after forming a thin liquid fuel layer [16, 17, 56]. For mode (i) the droplet evaporation time scale is given by

$$\tau_{evap,drop} = \frac{R_{drop}^2}{K} \tag{3.8}$$

where R_{drop} is an initial radius of a droplet, and K is the evaporation constant, which can be either heat transfer or mass transfer limited [70]. For heat transfer limited evaporation,

$$K = \frac{k_g}{\rho_l C_{p,g}} Nu_d ln\left(\frac{c_{p,g}(T_g - T_d)}{h_{fg}} + 1\right) \tag{3.9}$$

and for the mass transfer limited case,

$$K = \frac{\rho_g D_g}{\rho_l} Sh_d ln\left(\frac{1-y_{f,\infty}}{1-y_{f,s}}\right) \tag{3.10}$$

In Eqs. (3.9) and (3.10), ρ_l and ρ_g are the density of liquid and gas, respectively, $c_{p,g}$ is the specific heat of gas, k_g is the thermal conductivity of gas, h_{fg} is the latent heat of evaporation, and D_g is the gas diffusion coefficient. The dimensionless heat and mass transfer coefficients, Nusselt number, Nu_d and Sherwood number, Sh_d, are estimated from the correlations of Ranz and Marshall, $Nu_d = 2 + 0.552\mathrm{Re}_d^{1/2}\,\mathrm{Pr}_d^{1/3}$ and $Sh_d = 2 + 0.552\mathrm{Re}_d^{1/2}\,\mathrm{Sc}_d^{1/3}$, respectively.[71]

For mode (ii), the evaporative time scale for a thin liquid film is

$$\tau_{evap,film} = \frac{\rho_l h_{film}^2 h_{fg}}{k_g(T_\infty - T_S)} \tag{3.11}$$

where h_{film} is the film thickness and T_S is saturation temperature. [72]

It is important to note that if the timescale for evaporation is faster (more than one order) than other time scale (reaction or permeation), it can be considered as an instantaneous process.

3.3 CHAMP-DDIR Reaction-Transport-Separation Models

Two simplified theoretical reactor models with increasing complexities are developed. The first model, which is idealized CHAMP-DDIR simulation by neglecting heat and mass transfer limitation within the reactor, is used to assess the theoretical limits of CHAMP-DDIR performance for various practical operating conditions. Specifically, the volumetric power density was chosen a main performance metric since it is one of the most important metrics for portable fuel reformers. Then, the second model, inclusion of mass transport limitation and bulk temperature changes in time, is employed to evaluate possible performance improvement through combining time-modulated fuel introduction and the active change of reactor volume.

Both models are based on a previously reported model [14, 15] for CHAMP analysis of hydrogen production by methanol steam reforming on $Cu/ZnO/Al_2O_3$ catalyst (Figure 2.3). They differ from the previous work in (i) the membrane location (it is collocated with the catalyst to minimize mass transfer resistance), (ii) incorporation of a more accurate model for H_2 permeation that includes the reduction of permeance due to adsorption of non-H_2 species on the membrane surface, (iii) inclusion of transient temperature variation (due to fuel evaporation, reaction, permeation, volume variation, and heat input) in the non-idealized model, and, most importantly, (iv) in the focus, which is to identify the impact of reactor design and operating parameters on power density. In this section, both mathematical models are discussed first, and their simulation results will be followed in the next section.

3.3.1 Modeling assumptions

While the two models differ from one another in their complexity, both models share the following assumptions: (i) at the temperatures and pressures under consideration, all components of mixture in the reactor can be treated as ideal gases; (ii) at any given time, a uniform pressure exists in the reactor due to fast equilibration (as compared to the time scale dictated by the reaction kinetics);[15] (iii) hydrogen permeation across the membrane is diffusion-limited with reduction of permeance due to adsorption of other than hydrogen species on membrane surface;[69] (iv) rates of catalytic reactions are computed using an extensively-validated, empirically-determined state of the art kinetic model;[68] and, (v) vaporization occurs instantly (as compared to the reaction kinetics time scale) as fuel is introduced to the reactor.[16]

As discussed in the section 3.2.3 and further detailed in Appendix C, for the simulated CHAMP-DDIR reactor conditions, the fuel evaporation time scale is much faster (by 3 orders of magnitude) than the reaction kinetics and permeation time scales, supporting a simplified treatment of fuel vaporization as instantaneous.

3.3.2 Model description: idealized (isothermal and perfectly mixed) reactor model

The resulting one-dimensional idealized reactor models are based on the model parameters and geometry shown in Figure 3.1. One side of the reaction chamber with a cross-sectional area A is a moving wall (piston) that results in varying the chamber height (and reactor volume) as *H(t).* On the other side of the reaction chamber, a porous catalyst layer of porosity ε_{cat}, density ρ_{cat} and thickness d_{cat} is integrated with a hydrogen selective membrane with thickness δ_{memb}. During a fuel conversion cycle, the number of moles of species $N_i(t)$ (i denotes species index) changes as a function of time. The five species considered are methanol, water, carbon dioxide, hydrogen, and carbon monoxide. The total pressure in the reactor chamber, *P(t)*, is determined by the ideal gas law as function of time-varying reactor volume and number of moles of all species. The cycle begins with an initial

reactor volume filled with a methanol and water vapor mixture (1:1), assuming instant vaporization of fuel upon introduction.

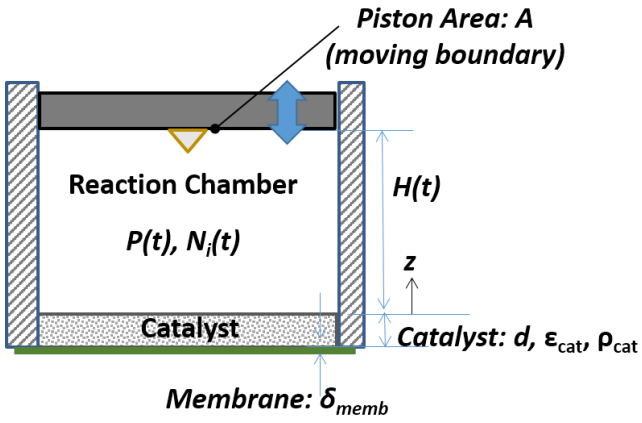

Figure 3.1 CHAMP-DDIR schematics showing dimensions and major domains for model formulation.

3.3.2.1 Additional assumptions for idealized model

The additional simplifying assumptions for the idealized model are (i) transport limitations are not considered within the reactor volume (spatially uniform concentrations for each species at a given time), and (ii) isothermal conditions (both spatial and temporal) exist throughout reaction chamber, catalyst layer and the thin membrane. The CHAMP-DDIR reactor at constant temperature does not necessarily yield the best performance. The motivation for use a constant temperature case in the initial idealized assessment is to isolate the effect of the temperature magnitude (in an average sense) from the dynamic aspects of the temperature change on the reactor performance. This simplification also facilitates a clearer understanding of fundamental relationships between the temperature and reactor performance (such as hydrogen yield or power density of the reactor), which could be difficult to ascertain from the results of an extensive parametric optimization aimed at finding an optimal temperature trajectory, which would be case/design-specific. There are also some practical reasons supporting the utility of isothermal operation (both in time and space), which are particular to CHAMP-DDIR

(i) Due to CHAMP-DDIR's transient nature, its thermal condition can be controlled in the time-domain (rather than the space-domain for continuous-flow reactors) by supplying heat to balance energy changes due to reaction, permeation, and heat losses during each phase of the cycle to maintain constant temperature [14, 15].

(ii) CHAMP-DDIR design features a low aspect ratio (gap height/reactor lateral extent) reactor structure with fuel ejectors separated by a small gap from the catalyst/membrane [56], thereby minimizing both the lateral (wall) heat losses and temperature variation across the gap due to the small thermal diffusion length.

3.3.2.2 Idealized Model Governing Equations

The governing equations for the idealized model are equations of species conservation:

$$\textbf{Species Molar Balance: } \boldsymbol{dN_i/dt = \sum_j \dot{R}_{ij} - \dot{J}_i} \qquad \textbf{(3.12)}$$

$$CH_3OH: \ dN_{CH3OH}/dt = \rho_{cat} A d_{cat}(-r_{MSR} - r_{MD}) \qquad (3.12.a)$$

$$H_2O: \ dN_{H2O}/dt = \rho_{cat} A d_{cat}(-r_{MSR} - r_{WGS}) \qquad (3.12.b)$$

$$CO_2: \ dN_{CO2}/dt = \rho_{cat} A d_{cat}(r_{MSR} + r_{WGS}) \qquad (3.12.c)$$

$$H_2: \ dN_{H2}/dt = \rho_{cat} A d_{cat}(3r_{MSR} + r_{WGS} + 2r_{MD}) - J"_{H2,perm} A \qquad (3.12.d)$$

$$CO: \ dN_{CO}/dt = \rho_{cat} A d_{cat}(r_{MD} - r_{WGS}) \qquad (3.12.e)$$

Eqs. (3.12) and (3.12.a)-(3.12.e), specify that the rate of change of number of moles N_i for species *i* within the reactor is equal to the sum of the rates of mole change due to reactions $\dot{R_{ij}}$ (for species *i* due to all reactions *j*), minus the rate of permeation through the membrane $\dot{J}_i$. The reaction kinetics and permeation models for finding $\dot{R_{ij}}$ and $\dot{J}_i$ are introduced previously in this chapter.

Since the fuel, which is a 1:1 mixture of CH_3OH and H_2O, is assumed to vaporize instantly, the initial conditions for the species mole balances are $N_{CH3OH}=N_{H2O}=0.5N_{fuel}$ and $N_{H2}=N_{CO2}=N_{CO}=0$ (or $=10^{-6}$ initial small moles was used in numerical computations to

avoid singularities in the kinetic expressions). Total reactor pressure follows ideal gas behavior and depends on changes of total number of moles, reactor volume (~temporary varying height), and temperature.

$$\mathrm{P}_{tot}(t) = \frac{N_{tot}(t)RT}{(H(t)+d\cdot\varepsilon\mathrm{cat})A} \tag{3.13}$$

For numerical solution of the model equations, each equation in (3.12) was explicitly integrated forward in time. Details of numerical solution implementation are provided in Appendix D.

3.3.2.3 Energy conservation for power density calculation

The total amount of energy input per cycle, E_{in}, is required to calculate the volumetric power density Eq. (3.1). Energy input, which is a combination of both work input by piston compression and heat input for evaporating the liquid fuel mixture, driving reactions, and achieving the desired final temperature, is calculated from the first law of thermodynamics

$$E_{in} = \underbrace{\sum_i^{species\ N}\left[(N_i u_i)_{final} - (N_i u_i)_{init}\right]}_{\substack{change\ in\ internal\ energy \\ within\ reactor\ volume}} + \underbrace{\int_{t_{init}}^{t_{final}} \dot{J}_{H2} h_{H_2}\, dt}_{\substack{energy\ left\ from\ reactor \\ with\ permeated\ H_2}} \tag{3.14}$$

where N_i, h_i, and u_i, are number of moles, enthalpy, and internal energy for *i* th species.

3.3.3 Model description: reactor model with dynamic temperature variation and mass transfer effects

This slightly more complex model considers the effects of mass transport limitations and time varying temperature during a transient reaction cycle. The model therefore not only accommodates analysis of more realistic operating scenarios of the variable volume batch reactor, but also allows consideration of the impact of dynamic introduction of liquid fuel.

3.3.3.1 Additional assumptions

In this model, species transport is modeled considering both diffusion and advection, while a single, "lumped" temperature is used to describe the temperature of the catalyst,

membrane, and gas in the reactor. Mass diffusion is modeled using Fick's law, with effective multi-component diffusion coefficients for each species. The effective diffusion coefficient of each species in mixture varies with composition, and it was calculated for each component diffusing through the mixture using an average mixture composition in the reactor corresponding to 50% methanol conversion. In determining the initial temperature it is assumed that the fuel is vaporized instantaneously at the moment before the simulation begins, resulting in a low initial lumped temperature. During the simulations, a constant heat input, $\dot{Q}_{IN}$, is applied, and $\dot{Q}_{IN}$ is found iteratively so that at the end of a cycle the total amount of heat input required for complete fuel vaporization and to drive the endothermic reactions while maintaining a target average reaction temperature has been supplied.

3.3.3.2 Enhanced Model Formulation

The governing equations for the idealized model are equations of species mass conservation applied to differential control volumes, and an equation of overall energy conservation applied to the entire reactor control volume:

$$\frac{\partial C_i}{\partial t} + \frac{\partial (C_i U)}{\partial z} = D_i \frac{\partial^2 C_i}{\partial z^2} \tag{3.15}$$

$$\frac{\partial}{\partial t}\left[(\rho c_v)_{eff} T\right] = \dot{Q}_{IN} - \sum_{j=1}^{RXN} \Delta H_j r_j(t) \tag{3.16}$$

C_i and D_i are the molar concentration and the diffusion coefficient of species i, and U is the molar average velocity of the species. Since the diffusion coefficient of a species i through the multicomponent mixture, D_i ,varies with composition, as well as molar flux of each component, Eq. 3.17 was used to find an approximate value for the D_i.[73] Assuming that species A, for example, is diffusing through a stagnant mixture of A, B, C, D, and E,

$$D_A = \frac{1 - x_A}{x_B/D_{AB} + x_C/D_{AC} + x_D/D_{AD} + x_E/D_{AE}} \tag{3.17}$$

The velocity is found from integrating the continuity equation for total molar concentration, $\frac{\partial c_{tot}}{\partial t} + c_{tot}\ \frac{\partial U}{\partial z} = 0$, (this simplification is possible by assuming spatially uniform pressure within the reactor and recognizing that the sum of the diffusive fluxes for all species must be zero) [15]. Integration yields $U(z) = \ \frac{-1}{C_T}\frac{dC_{tot}}{dt}z + constant$, and the constant can be found by applying boundary conditions at either of the two ends, at z=0 or z=H(t), leading to an identical result since the time rate change of total concentration in the reactor, $\frac{dc_{tot}}{dt}$, couples to the rate of transmembrane permeation $\dot{j}_{H2}$ at one boundary and the speed of piston motion $\frac{dH}{dt}$ at another boundary via $\frac{dc_{tot}}{dt} = \frac{1}{H}\left[\rho_{cat} d(2r_{MSR} + 2r_{MD}) - \dot{j}_{H2} - c_{tot}\frac{dH}{dt}\right]$.

Eq. (3.16), which imposes overall energy conservation, does not consider the impact of phase change of the liquid fuel, because effects of reaction and liquid fuel evaporation are treated separately due to the difference in their time scales. Thus, whether for the initial condition, or following fuel injection when multiple injections are simulated, an instantaneous temperature change during fuel injection is imposed:

$$\Delta \boldsymbol{T} = -\sum_{\boldsymbol{i=1}}^{\boldsymbol{M,W}} N_i \boldsymbol{u}_{\boldsymbol{fg,i}} / (\boldsymbol{\rho c_v})_{\boldsymbol{eff}} \tag{3.18}$$

For this simplification, there is an implicit assumption that the reduction of temperature due to evaporation, which occurs at the catalyst surface, instantaneously propagates through the entire volume of gas mixture in the reactor, which implies infinitely large gas phase thermal diffusivity, or at least that the Fourier number (based on reactor thickness H) is very large on a time scale of reactor kinetics.

In Eqs. (3.16) and (3.18) $(\rho c_v)_{eff}$ is an effective heat capacity, which combines ρc_v of catalyst layer and total gas species and varies in time due to changes in concentrations of each species in reactor, ΔH_j and r_j are enthalpy change of reaction and its rate for jth

reaction, *M* and *W* denote methanol and water, and $u_{fg,i}$ is latent internal energy of vaporization for each fuel species.

The governing equations that determine the species concentrations require boundary conditions at the reactor top and the catalyst surface, as well as initial conditions. The boundary condition at the catalyst/membrane surface (z = 0) is defined in terms of the flux of species, due to the consumption (negative flux, relative to z) or production (positive flux) of a product via the reactions and permeation. The boundary condition at the impermeable moving wall is the flux relative to the moving piston boundary (Table 3.1).

The initial conditions for the governing equations, Eq. (3.15) are,

$$C_{CH3OH,0} = C_{H2O,0} = 0.5\frac{P_{init}}{RT_{init}}, \qquad C_{CO2,0} = C_{H2,0} = C_{CO,0} = 10^{-6}\,[\frac{mol}{m^3}]$$

The small initial amounts of carbon dioxide, hydrogen, and carbon monoxide are provided to avoid singularities in the kinetic expressions at very short times.

Table 3.1 Boundary Conditions for Enhanced CHAMP-DDIR Model

boundary conditions @ *z=0:*	**boundary conditions @ *z=H(t):***
$C_{CH3OH}U\|_{z=0} - D_{CH3OH}\frac{\partial C_{CH3OH}}{\partial z}\|_{z=0} = \rho_{cat}d_{cat}(-r_{MSR} - r_{MD})$	$C_{CH3OH}U\|_{z=H(t)} - D_{CH3OH}\frac{\partial C_{CH3OH}}{\partial z}\|_{z=H(t)} = 0$
$C_{H2O}U\|_{z=0} - D_{H2O}\frac{\partial C_{H2O}}{\partial z}\|_{z=0} = \rho_{cat}d_{cat}(-r_{MSR} - r_{WGS})$	$C_{H2O}U\|_{z=H(t)} - D_{H2O}\frac{\partial C_{H2O}}{\partial z}\|_{z=H(t)} = 0$
$C_{CO2}U\|_{z=0} - D_{CO2}\frac{\partial C_{CO2}}{\partial z}\|_{z=0} = \rho_{cat}d_{cat}(r_{MSR} + r_{WGS})$	$C_{CO2}U\|_{z=H(t)} - D_{CO2}\frac{\partial C_{CO2}}{\partial z}\|_{z=H(t)} = 0$
$C_{H2}U\|_{z=0} - D_{H2}\frac{\partial C_{H2}}{\partial z}\|_{z=0} = \rho_{cat}d_{cat}(3r_{MSR} + r_{WGS} + 2r_{MD}) - J"_{H2,perm}$	$C_{H2}U\|_{z=H(t)} - D_{H2}\frac{\partial C_{H2}}{\partial z}\|_{z=H(t)} = 0$
$C_{CO}U\|_{z=0} - D_{CO}\frac{\partial C_{CO}}{\partial z}\|_{z=0} = \rho_{cat}d_{cat}(r_{MD} - r_{WGS})$	$C_{CO}U\|_{z=H(t)} - D_{CO}\frac{\partial C_{CO}}{\partial z}\|_{z=H(t)} = 0$

3.4 Simulation Results with CHAMP-DDIR Models

3.4.1 Analysis: idealized isothermal, perfectly mixed reactor model

In this model, which ignores transport limitations in the gas phase but includes a realistic membrane permeation model and catalyst kinetics, pressure, temperature, membrane thickness, specific membrane area, specific catalyst loading are identified as the key design and operation variables which can be controlled aiming to achieve the highest volumetric power density for CHAMP-DDIR under a constraint of a target H_2 yield efficiency.

3.4.1.1 CHAMP-DDIR Constant-Pressure vs. Constant-Volume Operation.

Representative simulation results from the idealized model for variable-volume (applying compression to maintain constant pressure at P_{max}) and constant-volume modes of operation are compared in Figure 3.2 for temporal changes in pressure, volume, hydrogen permeation rate, and hydrogen yield efficiency over residence time. For both modes of operation, simulation conditions are 500K for temperature, 3 bar for initial pressure, and a 99% H2 yield efficiency for cycle end criterion. Other model parameters are listed in Table 3.2.

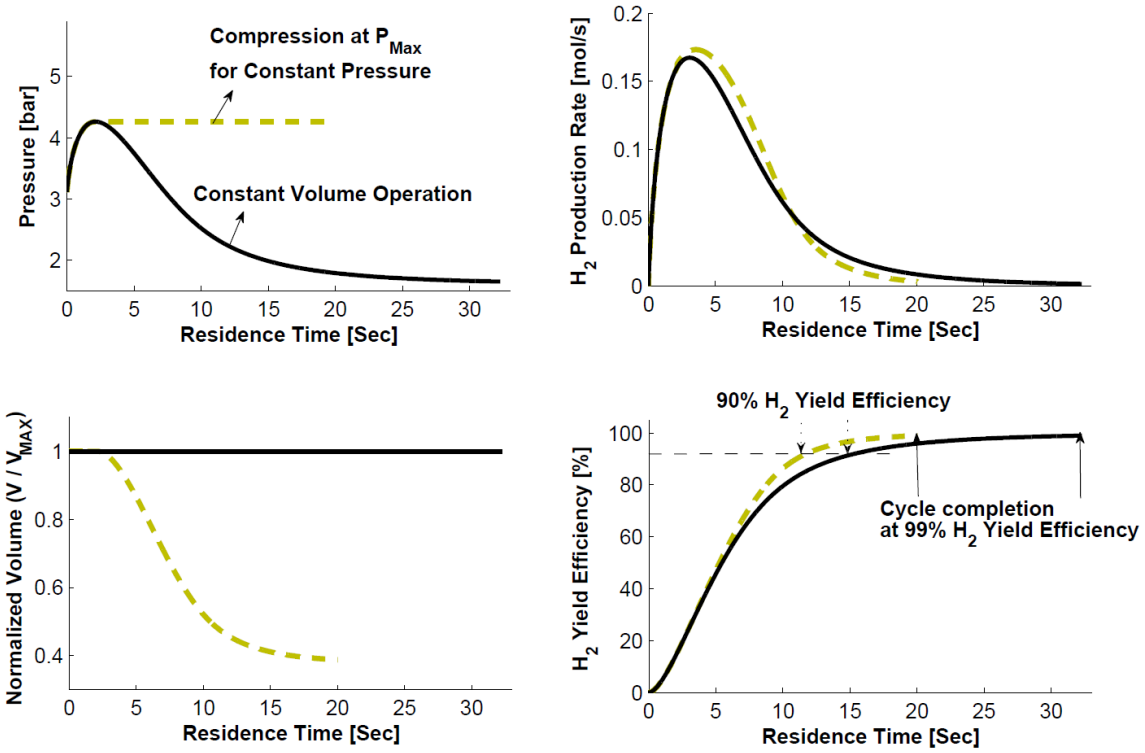

Figure 3.2 Comparison of representative simulation results for variable- and constant- volume modes of operation. Plots include temporal variation of parameters a) pressure, b) volume, c) hydrogen production rate, and d) hydrogen yield efficiency. The end criteria for each cycle simulation is 99% H2 yield efficiency

Table 3.2 Baseline parameters and default values for reactor model simulations.

Model parameters	**Value [units]**
Initial reactor size, H_{init}	0.015 [m]
Membrane thickness, δ_{memb}	1×10^{-5} [m]
Catalyst layer thickness, d_{cat}	5×10^{-4} [m]
Density of catalyst, ρ_{cat}	1300 [kg/m^3]
Porosity of catalyst, ε_{cat}	0.5 [-]
Specific surface area of catalyst, S_A	102×10^3 [m^2/kg]

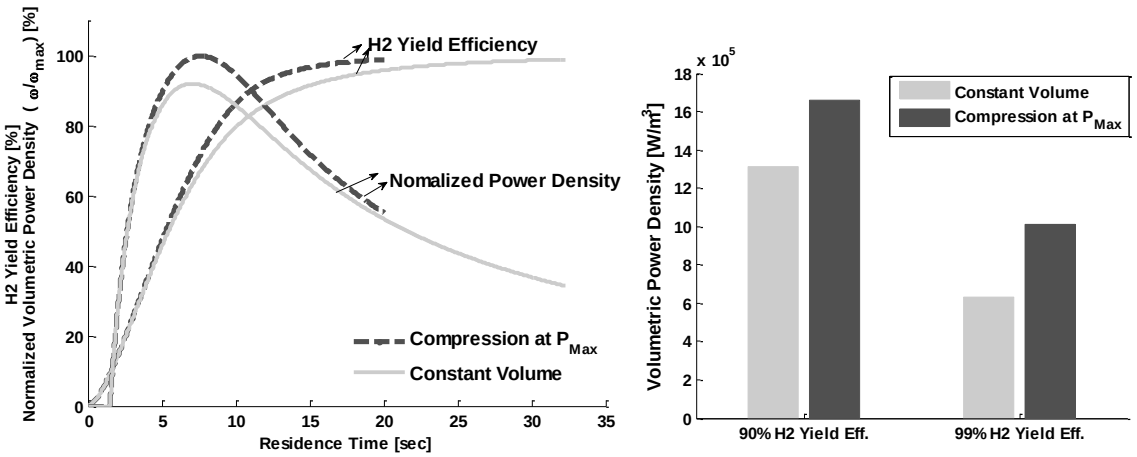

Figure 3.3 Variation of volumetric power density and H2 yield efficiency for variable-volume and constant-volume modes of operation. A tradeoff between power density and fuel utilization is revealed for both cases. The normalized power density (ω/ω_{max}) in the the left plot is scaled by the maximum value (ω_{max}) obtained among all of the simulated cycles (which is ω for 7.6sec long cycle with volume compression).

For both constant and variable volume operations, pressure increases initially because of an increase in the total number of moles by reactions. In the constant volume operation, pressure starts to decrease when the molar rate of hydrogen removal exceeds the net molar production rate in the reactor.

In contrast, in the variable-volume operation the volume is actively reduced (via forced piston motion) to maintain the pressure constant at its allowed maximum ($P_{max,C.V.}$) . The elevated hydrogen partial pressure in variable volume operation drives the permeation of hydrogen at a higher rate and enables more rapid completion of the reaction cycle as compared to constant volume operation. For the simulations depicted in Figure 3.3, the cycle completion time (at 99% H_2 yield efficiency) for variable volume operation (19.8sec) is about 40% shorter than that for constant volume operation (33sec.) Of course, the hydrogen production rate can be further enhanced by compressing the volume to increase pressure above $P_{max,C.V.}$ However, maximum allowable pressure is an important practical consideration in the design and operation of the reactor, in particular to maintain membrane integrity.

The capability of CHAMP to actively change the reactor volume throughout the fuel conversion cycle enables optimal control of residence time and reactor conditions (pressure and temperature), thus improving both the reaction and separation processes.

Another aspect to note is that the compression work for piston is included in the volumetric calculation for constant pressure operation. When comparing energy input for compression ($W_{piston} = \int PdV$) to energy output of reactor from generated hydrogen ($W_{H_2} = J_{H_2} LHV_{H_2}$), W_{piston} is only ~3% of W_{H_2} for the simulated case in Figure 3.3 (at 99% H_2 yield efficiency), while compression results in 27% gain in volumetric power density (compared to non-compression cycle).

3.4.1.2 Tradeoff between power density and fuel utilization.

Temporal variations of volumetric power density for each mode of operation are plotted with H_2 yield efficiency in Figure 3.3. Comparison of power densities for constant volume and constant pressure modes of operation reveals that variable volume operation maintaining pressure in the reaction chamber at a high value provides a significant improvement in power density. The advantage is due to the reduced cycle time (for the same H_2 yield) resulting from enhanced H_2 production rates, primarily due to enhanced permeation, driven by compression. In addition, an interesting tradeoff between power density and hydrogen yield efficiency over residence time is revealed. The maximum power density occurs when short cycle times are achieved at the expense of fuel utilization (and yield efficiency). This tradeoff is accentuated when compression is not used to maintain high permeation driving force (e.g., solid curves in Figure 3.3) as significantly longer residence times are required to "extract" hydrogen (and thus power) out of the reactor at the end of the cycle when its low partial pressure decreases the driving force for permeation across the membrane. Since an increase in a residence time results in higher heat losses, power density will further decrease with increasing residence time if heat losses from reactor wall are considered in the model[74]. Although the chief objective of portable

fuel processing is to increase power density, operating the reactor for maximum power density is impractical due to low utilization of fuel. Thus, hereafter we examine reactor performance in the context of maximizing power density, but, in keeping with common practice [45, 75], balance the goal of power density and adequate fuel utilization to maintain at least 90% hydrogen yield.

3.4.1.3 Theoretical Limits of Achievable Volumetric Power Density by CHAMP-DDIR.

With the idealized model, pressure, temperature, volume, membrane thickness, specific catalyst loading, specific membrane area and residence time are selected as control parameters to find optimal conditions resulting in the highest volumetric power density for CHAMP-DDIR. Power density maximization can be achieved via enhanced hydrogen production, lower energy input, smaller reactor volume, and shorter reaction cycle.

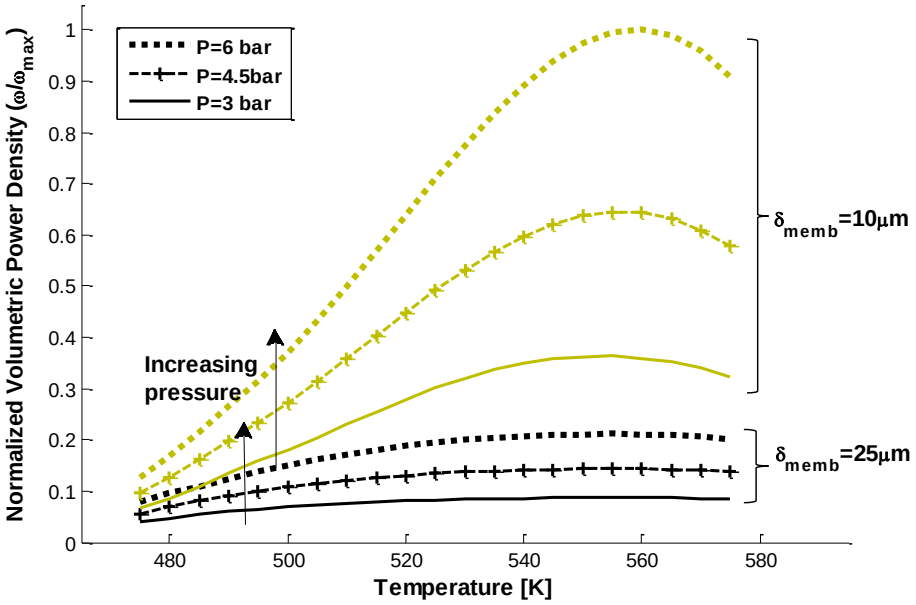

Figure 3.4 Volumetric power densities for 90% yield efficiency as functions of temperature and pressure for two different membrane thicknesses (δ_{memb}). Volumetric power density is normalized with respect to the maximum value (ω_{max} =3.11×10^6 W/m^3 at P=6 bar, T=555 K and δ_{memb} =10 μm) among all simulated conditions depicted in the figure.

In Figure 3.4, volumetric power densities of an ideal CHAMP-DDIR cycle for 90% hydrogen yield efficiency are plotted within the allowed temperature range of the catalyst, 475-575K, for copper and zinc oxide based catalysts ($Cu/ZnO/Al_2O_3$). Different curves are for varying membrane thicknesses (10, 25μm) and reaction pressures (3, 4.5, 6 bars). For a consistent comparison of power density the following simulation conditions were applied for all cases: (1) constant pressure operation with fixed initial volume, and (2) all simulated cycles start with the same amount of fuel and the initial reactor volume is determined by the ideal gas law for the given pressure. Option (2) is chosen rather than another alternative approach, fixing the initial reactor volume and varying the fuel amount to match the specified pressure, which we also examined for completeness. Both approaches result in identical trends, albeit with slight quantitative differences due to their difference in initial volume or amount of fuel, so only predictions for simulations based on the same amount of injected fuel (and variable initial reactor volume to match the pressure) are described next.

Power density increases monotonically with higher reactor pressure and thinner membrane due to the increase in transmembrane hydrogen flux (resulting in a higher hydrogen production rate). This effect is expected (from Sievert's law) and indicative of permeation-limited behavior. In addition, the faster removal of hydrogen shifts the reaction rates in the favorable direction (enhanced forward rates for both methanol steam reforming and water-gas shift reactions). For each operational pressure and membrane thickness, an optimum temperature for maximizing the power density exists within the allowed temperature range of the catalyst. The presence of the optimum temperature for volumetric power density is due to competing temperature effects. Both the MSR reaction and permeation rates increase with temperature, and at lower range of operating temperatures this is the main driver for rising power density. Opposing this trend are two effects: (i) from the ideal gas law, volume increases linearly with temperature (at constant pressure and molar content); and, (ii) more heat input is required to maintain the reactor at an elevated

temperature. Both effects (i) and (ii) mitigate, and eventually overwhelm, the benefits of higher temperature on power density, and their effect is more pronounced when the permeation rate is lower, i.e., for thicker membrane, for which the optimum temperature is lower than for thinner membranes.

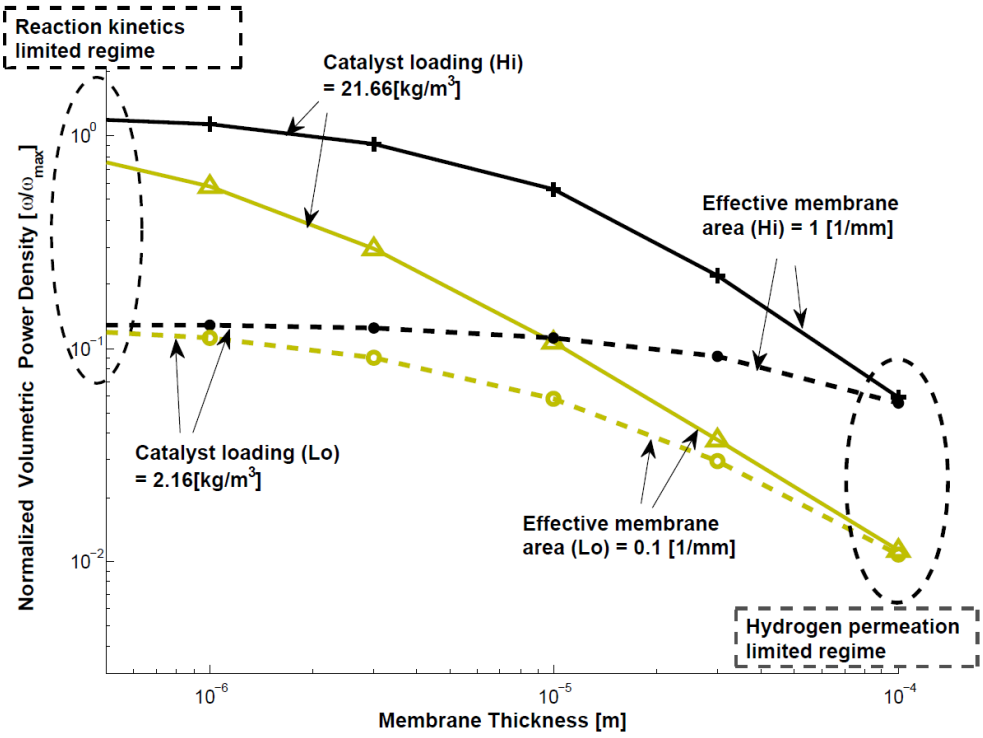

Figure 3.5 CHAMP-DDIR power density transition from reaction kinetics-limited regime to hydrogen permeation-limited regime as function of the membrane thickness (δ_{memb}), specific membrane area (A_{memb}), and catalyst loading (L_{cat}). The simulated reactor conditions are constant pressure operation at 5 bar and 525K. Volumetric power density is normalized by the maximum value (ω_{max} =2.71×10^6 W/m^3, L_{cat}=21.66 kg/m^3, A_{memb}=0.1[1/mm], and δ_{memb} =0.5 μm) among all simulated condition.

Along with temperature, membrane thickness and specific membrane area directly affect hydrogen permeation rate and thus the power density. Since the permeation model assumes that hydrogen permeation across the membrane is diffusion-limited, with the membrane thickness being the diffusion distance, the hydrogen permeation rate is inversely proportional to the membrane thickness. The permeation rate is proportional to specific membrane area, defined as membrane area divided by reactor volume (A_{memb}/V). Similarly,

specific catalyst loading ($L_{cat} = Ad\,\rho_{cat}\varepsilon_{cat}$/V), which is defined as catalyst loading per unit volume of reactor, directly affects reaction rates. Figure 3.5 depicts the combined effects on power density of changing membrane thickness, specific membrane area, and specific catalyst loading, and reveals the limiting processes at the extreme combinations of parameters.

In general, increased permeation rates due to (i) a thinner membrane and (ii) higher specific membrane area, as well as increased reaction rates due to (iii) higher specific catalyst loading, all result in higher power density. However, the relative importance of changes in these three parameters depends upon which of them is most responsible for limiting reactor performance. In the reaction kinetics-limited regime, changes in the specific membrane area and membrane thickness have only a minor effect on the power density (see convergence of all dashed lines in the limit of small membrane thickness). On the other hand, in the hydrogen permeation-limited regime, changes in the catalyst loading (from low ρ_{cat}=*2.16 kg/m*^{3} to high ρ_{cat}=*21.66 kg/m*^{3}) have a negligible effect on the power density (see pair-wise convergence of continuous and dashed lines at large membrane thicknesses).

Specific membrane area (A_{memb}/V) is equivalent to the inverse of maximum reactor height, so variation of this parameter will also impact mass transfer resistance inside the reactor volume. The idealized model does not consider any mass transfer effects in the reactor bulk, but this effect will be discussed in the next section.

3.4.1 Analysis: enhanced reactor model accounting for dynamic temperature variation and mass transfer effects

The idealized kinetic reactor model, which provided several important insights on power density maximization, is enhanced through inclusion of i) the effect of mass transport limitation and ii) temporal temperature change (spatially uniform) during a transient reaction cycle. Since volume variation is one key feature of CHAMP-DDIR operation, the inclusion of mass transport limitation can be more important considering additional

advection of species driven by piston motion as well as change in a diffusion length by volume compression. In addition, inclusion of temperature change in the model enables a better characterization of the impact of transient liquid fuel introduction on reactor performance. Although direct impingement of liquid fuel on the catalyst has significant benefits,[16] one of its potential shortcomings is the temperature drop of catalyst and membrane due to the evaporation of fuel droplets on the catalyst surface (catalyst quenching). This significant penalty cannot be captured with the idealized isothermal model. The magnitude of decrease in temperature, as thermal energy transferred from the catalyst, gas, and membrane supplies the required latent heat of evaporation, is proportional to the amount of fuel being vaporized. One strategy to mitigate the potential negative impact of vaporization induced temperature decrease is to modulate the fuel introduction, i.e., use multiple injections during a single cycle, and thus prevent a large temperature drop at the beginning of cycle. A coupled transport-kinetics model, Eqs. (3.15)-(3.16), is used to investigate the process improvement via variable volume and pulse modulated fuel injection and to conduct a general parametric study of the reactor operating space, all in terms of power density as a metric for optimization.

3.4.1.1 Representative Predictions with Enhanced Model.

In Figure 3.6, three sets of results depict separately the effects of transient temperature change and mass transfer limitations for one particular reactor geometry, component dimensions, and catalyst loading. The results in Figure 3.6 indicate that internal mass transfer resistance due to gas phase diffusion of species within the reactor volume slows down the rate of hydrogen production in general, and results in reduced volumetric power density. It is interesting to note that a non-negligible internal mass transfer initially increase the hydrogen production rate over that predicted by the ideal model at the very beginning of the cycle. This is because the diffusive transport resistance allows hydrogen generated at the catalyst surface to build up rather than diffusing instantly throughout the reactor

volume, thus promoting more rapid permeation, and highlighting a benefit of the CHAMP-DDIR configuration depicted in Figure 3.1 in which the catalyst and membrane are adjacently located.

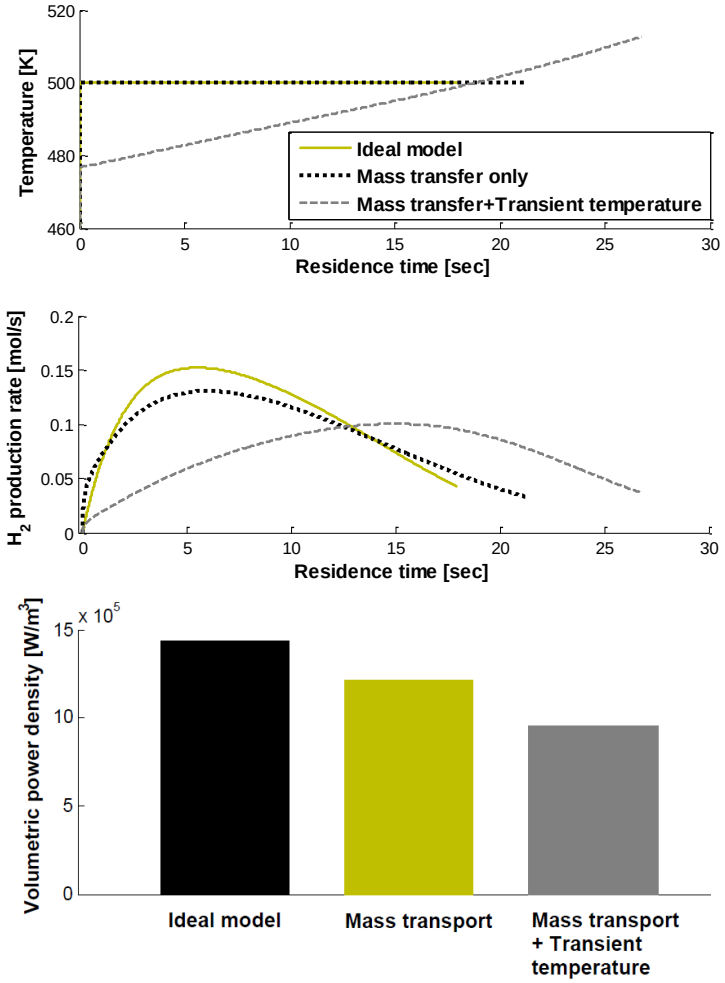

Figure 3.6 Predictions for variations of temperature, hydrogen production rate, and volumetric power density from three different CHAMP-DDIR models; i) no mass/heat transfer effects, ii) with inclusion of mass transfer only, and iii) considering both mass transfer and transient temperature. Constant volume operation with height fixed at 0.015m, 10μm membrane thickness, and 90% yield efficiency criteria is used for all simulations. All cycles start at 4 bar initial pressure, with the same amount of fuel injected at the beginning of a cycle. Temperature in computations using an ideal model and the mass transport only model is kept constant at 500K. Temperature evolution for the mass transfer/transient temperature model is determined from conservation of energy.

3.4.1.2 Effect of Mass Transfer in the Reactor Chamber.

The impact of diffusional mass transfer on volumetric power density is assessed in the context of variable volume operation. Figure 3.7 shows predictions of volumetric power

densities with varying effective maximum reactor height (V_{max}/A_{memb}), and therefore varying diffusion distance within the reactor. The decrease in power density with higher maximum effective reactor height is expected, from the study of idealized model, since the reactor chamber height scales as an inverse of membrane area (V/A_{memb}, see Figure 3.7). When the assumption of uniform concentrations (perfect mixing) in reactor volume is relaxed and replaced by the transient one-dimensional species transport equations, i.e., Eq. (3.15), the decline in power density with higher effective height is further accentuated due to increased resistance for mass transfer. When the effective reactor height is the smallest ($<10^{-3}$ m), the diffusion resistance in the reactor volume is negligible as compared to the membrane resistance, and so the effect of the mass diffusion limitation in the gas phase is insignificant and results with and without mass transfer included in the model are nearly identical. The results depicted in Figure 3.7 therefore confirm what one would expect, that power density decreases with increasing effective reactor height due to both decreased specific membrane area and an increased resistance for mass transport.

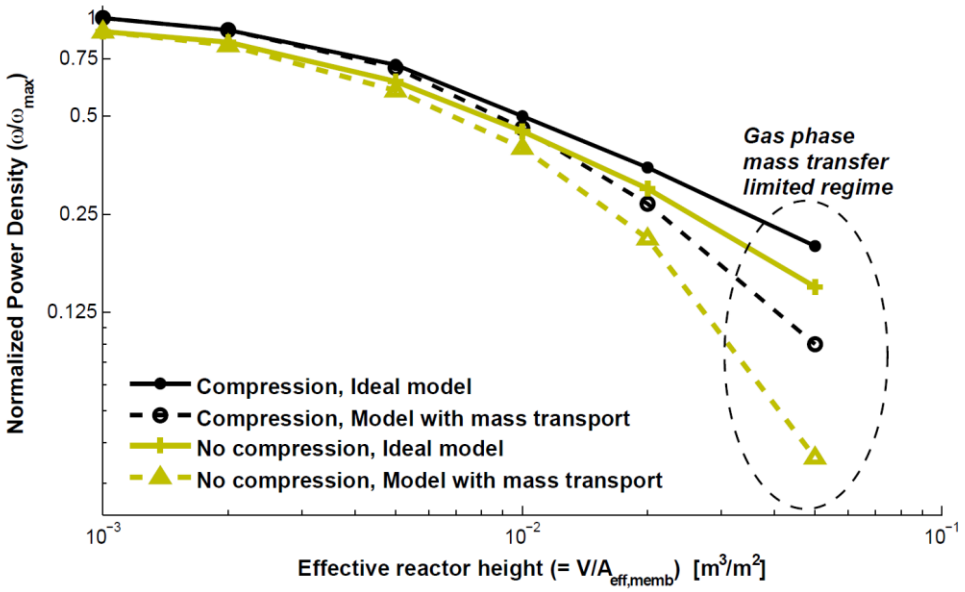

Figure 3.7 Impacts of mass transfer and volume change on power density of CHAMP-DDIR. All simulated cycles start at P_{init}=4bar. For compression operations, volume is varied to maintain the total reactor pressure at 4bar. Operations without compression are constant volume mode. Temperature is kept constant at 500K and membrane thickness is 10μm. Volumetric power density is normalized by its maximum value (ω_{max} =1.91×10^6 W/m^3 at V_{max}/A_{memb} =10^{-3}[m]) among all simulated conditions.

When modeling reactor operation with compression and including mass transfer resistance, an additional benefit of variable volume operation on power density is revealed. Specifically, compression reduces the reactor height and therefore reduces the internal mass transfer resistance. Comparing the predicted power density between ideal model and enhanced model, the advantage achieved via variable volume operation is more pronounced for greater $V_{max}/A_{memb,}$ because of the larger reduction in diffusion distance.

3.4.1.3 Effect of Temperature Drop Due to Fuel Evaporation.

A significant reduction in both reaction and permeation rates can be caused by the large temperature drop due to fuel evaporation during direct injection of liquid fuel. In the example depicted in Figure 3.8, the temperature drops from 525K to 503 K immediately when fuel is introduced at the beginning of cycle: the reaction rate for steam reforming (with given initial species concentrations) at 503K is only about 30% of that at 525K, and permeation rate with pure hydrogen for the given membrane at 503K is 87% of that at 525K. As a result, the hydrogen production rate predicted by the model that considers both mass transfer and transient temperature evolution is much lower than that predicted by isothermal models (with and without mass transfer) until the temperature level is restored via external heating. As a result, due to slower reaction and permeation, the total cycle completion time for the same yield efficiency is significantly longer, and thus a reduction in power density is observed.

In order to mitigate this detrimental impact, several improvements to reactor operation can be applied to maintain the catalyst and membrane temperature at the elevated level, including (i) controlling external heat input to maintain the ideal temperature profile, (ii) utilizing the thermal mass of the reactor, and (iii) modulating fuel injection. The first mitigation method, to control external heat input to match the ideal (isothermal) temperature profile, is suitable considering the practical advantage of a batch reactor

system. Fundamentally, the heat supply in CHAMP is more optimal (i.e., avoids excessive overheating and hot spots due to conjugate heat transfer and spatial variation in reaction rates) and is easy to implement via basic feedback control strategies to achieve desired thermal condition as compared to classical continuous flow (CF) reactors.

However, even with the relative ease of time-varying heat input implementation, a highly accurate control of temperature is difficult to achieve in practice due to the thermal mass of components and resulting finite thermal response rates. The second method, which is utilizing the heat stored in the thermal mass of reactor, can also be beneficial to maintain the reactor temperature at a higher level. The current model that includes temperature variation assumes that the entire heat input required for fuel evaporation is extracted from stored thermal energy within the thin catalyst layer and gaseous mixture, which is a worst-case approximation, as no heat stored in the reactor structure is taken into consideration.

Of the three possible mechanisms for reactor thermal control, fuel injection modulation is the most easily implemented. This mitigation method directly controls the main source of the temperature drop, which is direct injection of liquid fuel. In this approach, the large temperature drop caused by a single injection is avoided by splitting the injection into multiple pulses.

3.4.1.4 Time-Modulated Fuel Injection.

The impact of the modulated fuel injection is shown in Figures 3.8-3.10. For these results, the duty cycle and frequency of modulated fuel injection have not been optimized, but rather chosen to illustrate the advantage of the injection technique on volumetric power density. For the constant volume operation shown in Figure 3.8, when the fuel was introduced in four equal dose injections spread over three seconds, the average pressure is lower and average temperature is higher than when the entire amount of fuel is introduced in a single injection. While a higher temperature is beneficial for increasing both MSR reaction and membrane permeation rates, the lower pressure negatively effects hydrogen

permeation and thus the power density. Nevertheless, for the simulated conditions, the positive effect of higher temperature is just sufficient to surpass the negative effect of lower pressure, yielding a 3.5% improvement in power density. This trend is not persistent through all possible split injection scenarios. In addition to a decrease in average pressure, delay of the fuel delivery can be another detrimental factor for power density caused by the split injection. If the time over which the injections occur is made too long, then although the average temperature can be maintained at a higher level, the delay in fuel supply and reduction in permeation rate due to lower pressure can lead to a reduced power density.

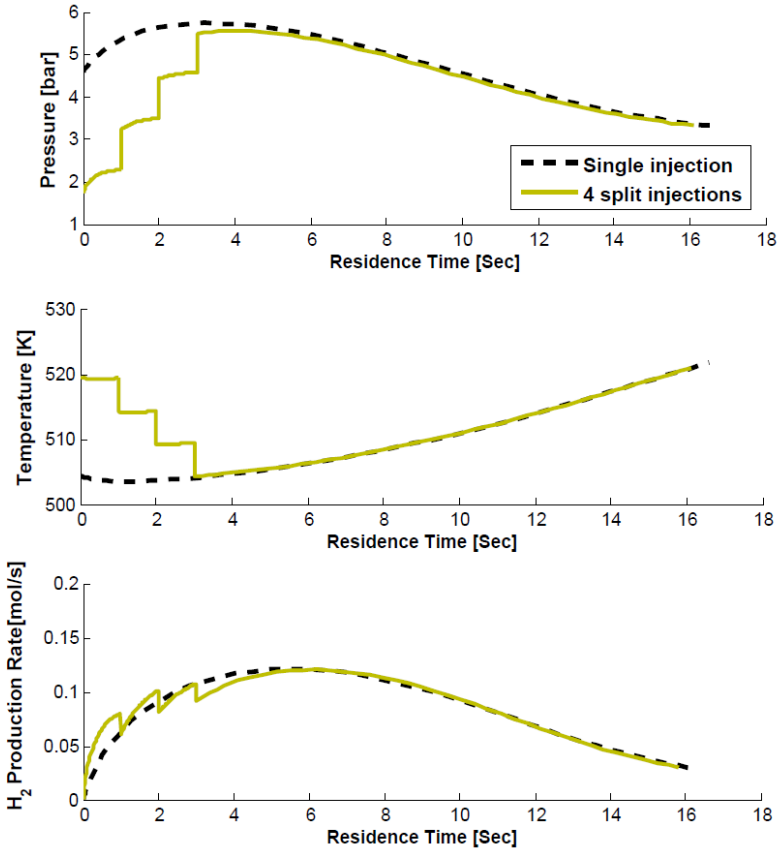

Figure 3.8 CHAMP-DDIR model simulations of modulated fuel introduction for constant volume operation with reactor chamber height fixed at 0.015m. Simulations are performed for the same total amount of fuel injected into the reactor, contrasting single injection (dashed line) vs multiple injections (solid line), at 525K initial temperature, 10μm membrane thickness, and 90% hydrogen yield efficiency as the cycle end criteria

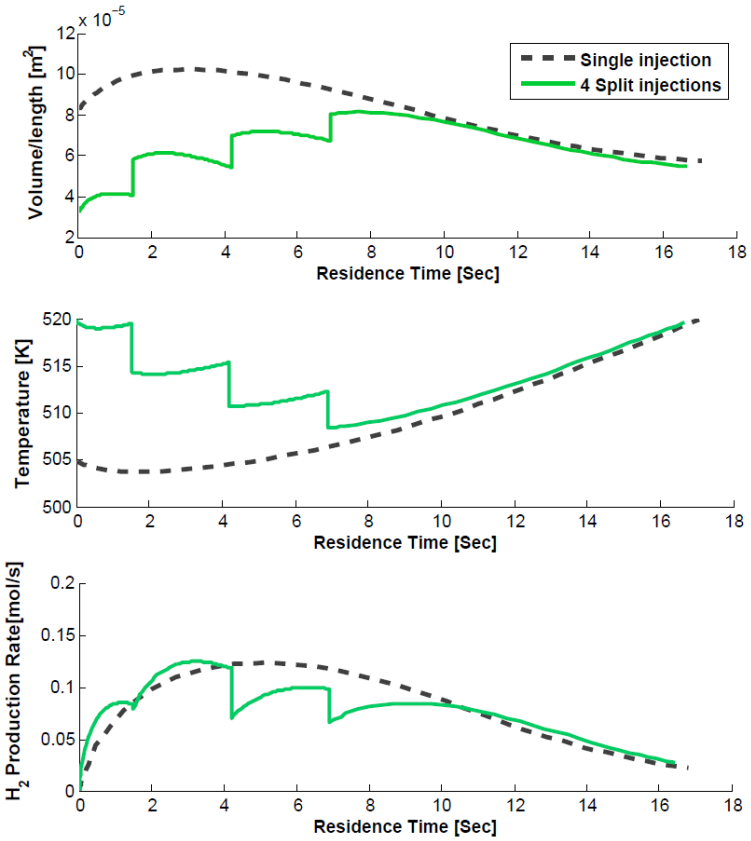

Figure 3.9 CHAMP-DDIR model simulations of modulated fuel introduction for constant pressure operation at 5 bar. Two simulations (single injection vs. four split injections) use the same total amount of fuel, 525K initial temperature, 10μm membrane thickness, and 90% hydrogen yield efficiency as the cycle end criteria.

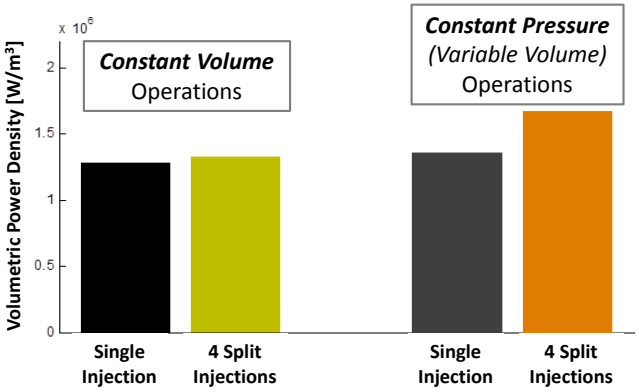

Figure 3.10 Volumetric power densities for constant volume (Figure 3.8) and constant pressure (Figure 3.9) operations with the same total amount of fuel introduced into the reactor, but using different number of injection dozes. Most enhancement of volumetric power density is achieved by applying modulated fuel introduction in combination with volume compression to maintain high pressure in the reactor chamber.

When modulated fuel injection is combined with variable volume operation, such as the constant pressure mode of operation, the required reactor volume becomes the dominant parameter that determines volumetric power density. For the constant pressure operation shown in Figure 3.10, the maximum required volume during the conversion cycle is significantly reduced (by as much as 22%) when the fuel injection is split into multiple pulses. This reduced volume as well as higher hydrogen production rate (due to higher average temperature) results in potentially significant increases in the volumetric power density. In Figure 3.10, resulting power densities are shown for the case studies analyzed in Figure 3.9 with a 25% increase in power density predicted when the injected fuel was split into four injections over 9 second time interval. Comparison of volumetric power densities for the constant volume (Figure 3.8) and constant pressure (Figure 3.9) operations indicates that volume compression enables mitigation of the reduced pressure and delay in fuel delivery accompanying split injection observed in constant volume operation and brings a substantial advantage in power density. Further improvement in power density might be achieved by exploring comprehensive multi-dimensional optimization across the entire set of operational parameters, such as frequency and duty cycles for fuel injection modulation, piston trajectory for volume/pressure modulation, and heat input for temperature control.

3.5 Conclusions

In this chapter, a comprehensive assessment of volumetric power density, with systematic methods of evaluation based on first principles of coupled reaction-transport phenomena for various CHAMP-DDIR operating conditions is performed. The assessment with an idealized (perfectly mixed and isothermal) reactor model revealed that

- A tradeoff exists between power density and hydrogen yield (fuel utilization). Hence, power density should be evaluated in the context of a constraint imposed by a minimal acceptable hydrogen yield.
- Volumetric power density increases monotonically with increasing pressure and catalyst loading and decreasing membrane thickness, especially in the permeation-limited regime
- An optimal reactor temperature, with respect to volumetric power density, exists within the allowed temperature range of the catalyst (e.g. maximum power density occurs around 555K when varying temperature between 475 and 575K and pressure between 3-6 bar) due to competing temperature effects: MSR reaction and hydrogen permeation rates increase with temperature (positive effects), but the required reactor volume and heat input also increase (negative effects) with temperature.

An extended CHAMP-DDIR analysis, which accounts for the effects of mass transport limitation and bulk temperature change in time, was performed for further assessment of the impact of practically relevant physical phenomena on the reactor power density. Two main conclusions have been reached:

- Improvement in volumetric power density can be made when variable volume operation is combined with modulated fuel introduction, because multiple fuel injections enable higher reaction/permeation rates by preventing a large temperature drop resulting from evaporation of a large quantity of fuel introduced in a single injection, and taking advantage of dynamic volume compression during a batch cycle to reduce the reactor volume and to maintain an elevated reactor pressure beneficial for both reaction and permeation rates.
- In practically realized fuel reforming systems, such as commonly used CFRs, transport limitations are critically important and often substantially reduce the power density of fuel-to-hydrogen conversion. The CHAMP-DDIR class of reactors provides

effective means for managing these challenges by directly delivering a fuel mixture to the catalyst surface for rapid flash volatilization and on-a-spot reaction (DDIR) as well as reducing the diffusion distance for desired product(s) transport from the reaction zone to separation/utilization site (CHAMP). Collectively, this results in a possibility to dramatically increase hydrogen production rate and thus improve the volumetric power density, approaching an ideal limit set by the intrinsic reaction kinetics and membrane separation capacity.

CHAPTER 4

EXPERIMENTAL INVESTIGATION

In this chapter, the results of experiments with a prototype CHAMP-DDIR reactor are described. A laboratory-scale CHAMP-DDIR, consisting of a variable volume piston-cylinder reactor chamber and an actively-controlled micro injector for liquid fuel atomization, is used with a Pd-Ag foil membrane and $Cu/ZnO/Al_2O_3$ catalyst to steam reform methanol for hydrogen generation. Two modes of CHAMP-DDIR operation, pulse-modulated fuel injection and batch reaction with dynamically-adjusted reactor volume, are investigated, and their performance is quantified using metrics such as hydrogen yield and volumetric power density, and compared with those for a baseline operation (single fuel injection with fixed reactor volume). The experimental results reveal that (i) residence time for the same hydrogen yield can be reduced by compression of the reactor volume during the conversion cycle, and (ii) the maximum required reactor volume can be significantly reduced by multi-shot split fuel introduction. Both the reduction in required cycle time and the reduction in required reactor volume increase the volumetric power density of CHAMP-DDIR.

4.1 Experimental Apparatus

Figure 4.1 shows a schematic diagram of the prototype reactor, while Figure 4.2 has photographs of the reactor and related experimental apparatus. The reactor has four major components: (i) main reactor block (made of stainless steel 17-4) that holds the catalyst, hydrogen selective membrane, thermocouples, and a pressure transducer, (ii) reactor cylinder (usually PEEK, although glass and steel were also used) that acts as a reaction chamber whose volume can be changed by a moving piston, (iii) heater/permeation block (aluminum alloy 7075) that holds cartridge resistance heaters to supply heat to the entire

reactor and passages to carry permeated hydrogen with sweep gas to the mass spectrometer, and (iv) piston block (PEEK) which incorporates a fuel injection nozzle and whose motion is actively controlled by a linear actuator. The dimensions of reaction chamber are 17.5mm inner diameter, 2.5mm minimum and 20mm maximum height (volume varying from 0.6cc to 4.8cc). Dead volume for the flow and instrumentation ports is 1.2cc. Therefore the maximum volume of reactor is 6.0cc. O-ring seals on the piston and blocks are made of high temperature perfluoroelastomers (FFKM) with a maximum temperature limit of 575K.

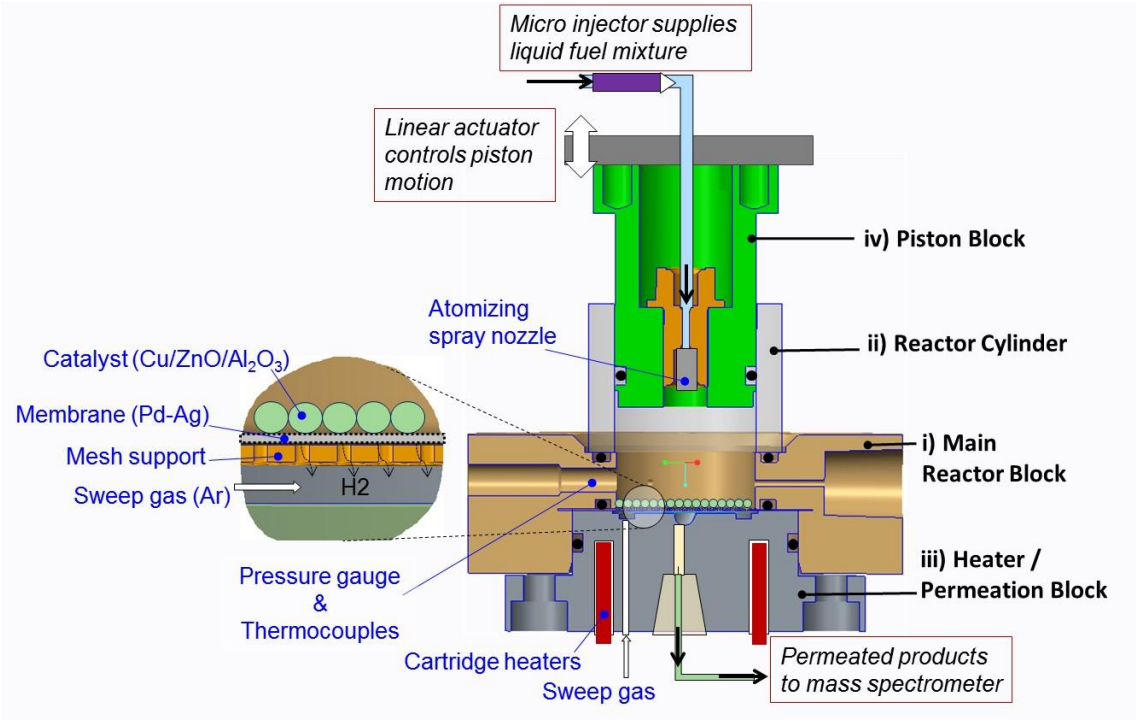

Figure 4.1 Schematic of the CHAMP-DDIR prototype. The inset shows a close up view of the evaporation/reaction/permeation site where catalyst and membrane are collocated. Hydrogen produced at the catalyst permeates through the membrane and is carried to mass spectrometer with argon sweep gas. The liquid fuel is 1:1 molar mixture of methanol and water. The piston block position is actively controlled and hydrogen production rate, pressure, and temperature are monitored and recorded during the reaction cycle.

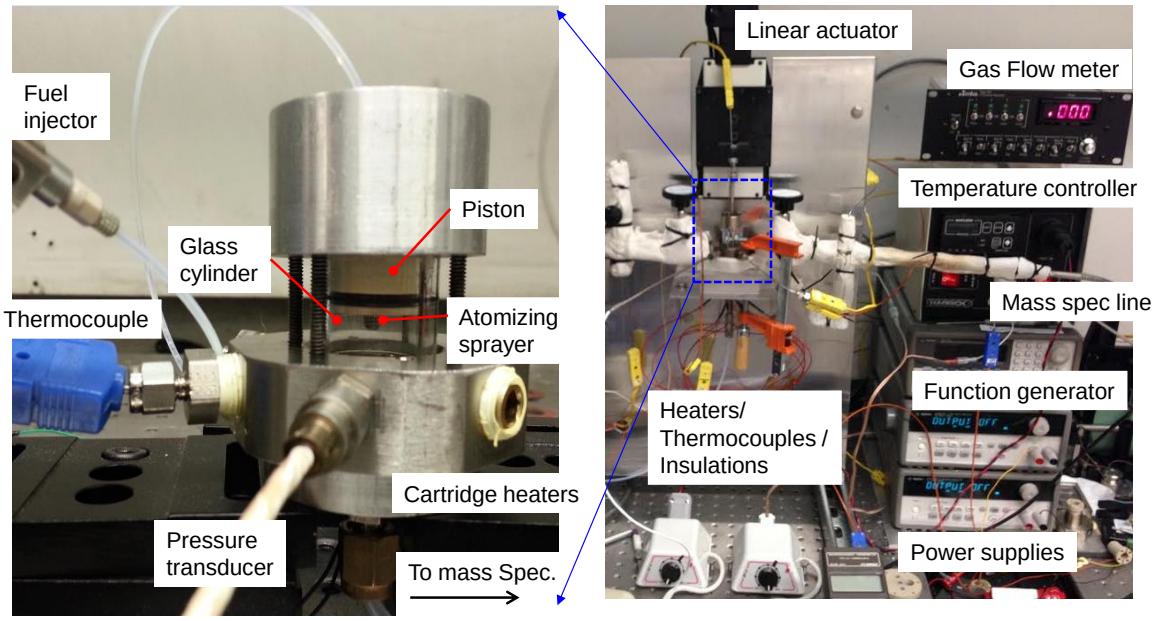

Figure 4.2 Pictures of CHAMP-DDIR prototype. Right figure shows the entire reactor system including control/measure devices (Gas flow meter, temperature controller, power supplies, heater power controller, thermometers, etc.) and left figure shows details of reaction chamber (same domain depicted in Figure 4.1)

4.1.1 Catalyst

$Cu/ZnO/Al_2O_3$ catalyst (BASF F3-01) was used to facilitate the MSR reactions. The catalyst was crushed and sieved to diameter of 200-250 μm to minimize inter- and intra-particle diffusion resistance but allow good gas distribution [76]. A uniform layer consisting of 0.5 g of catalyst was spread over the 2.45cm^2 membrane cross section (~0.1g/cm^2). The reaction temperature was varied between 473-533 K, which is within the recommended operational range for catalyst. Within this range, the reaction rate for the endothermic methanol steam reforming increases with higher temperature. The copper-based catalyst deactivates over 573 K [77].

Prior to loading in the reactor, the $Cu/ZnO/Al_2O_3$ catalyst was reduced by flowing a gas mixture of hydrogen and argon (10/90) over the catalyst at 453K for 1 hour at a flow rate of 200 sccm, per the manufacturer's directions. During the catalyst reduction process, the

catalyst temperature drops, due to the reduction being an endothermic process, and the mole fraction of hydrogen exiting the chamber is decreased due to consumption in the reduction process. Therefore, a rise in both hydrogen concentration and temperature indicates completion of catalyst reduction.

4.1.2 Hydrogen selective membrane

A 25μm thick Pd-Ag alloy membrane (75 wt% Pd, Alfa Aesar) was used to selectively remove hydrogen from the reactor. The membrane, cut into a 25mm diameter disk from Pd-Ag foil, was supported on a perforated 0.62mm thick stainless steel plate inside the reactor block (Figure 4.2). The supporting plate, designed to allow the thin Pd-Ag membrane foil to support a 10^6 Pa differential pressure, was fabricated by drilling staggered holes (0.5mm diameter) to achieve a 40% open area. The membrane was sealed using a high temperature O-ring made of Chemraz between the main reactor block and the permeation block.

The Pd-Ag membrane required pre-conditioning for enhanced permeation by heating at 1000 K for 1 hour prior to use [78]. After this conditioning process, performed in air in a furnace, the Pd-Ag foil turns to a light green metallic color. Once the membrane is conditioned and installed in the reactor, it should not be exposed to air or pure hydrogen at low temperature (below 425K). Even though the silver content (25%) in the membrane is known to lower the critical temperature for hydrogen embrittlement (the spinodal decomposition temperature of pure Pd is 573K)[79], it was observed that Pd-Ag membranes hardened after being used in the reactor. This issue was mitigated by, at the completion of each set of experiments, maintaining the reactor above 475K while flowing Ar on both sides of the Pd-Ag membrane for 15 minutes to reduce the dissolved hydrogen content of the membrane.

Whenever a new Pd-Ag membrane is installed, the permeance of hydrogen for the specific membrane is experimentally characterized via a pure hydrogen permeation test. For this

test, the hydrogen permeation rate, obtained using a mass spectrometer, and reactor pressure evolution were monitored after filling the reaction chamber with pure hydrogen at 3-5bar. This process of membrane characterization is important since the variance in permeance across different membranes was about 10%, even with membranes that have been conditioned identically and were from the same manufacturing batch.

4.1.3 Pulse-modulated liquid fuel injector

For introducing the liquid methanol/water fuel mixture with precise modulation of injection amount and time, a micro solenoid valve from Lee company (VHS 10050X) was used. The microvalve allowed pulse-injection of fuel volumes as small as 0.05μL per single pulse, with a 0.5 ms response time. The liquid fuel transmitted by the microvalve was sprayed into the reactor chamber from an atomizing nozzle (Lee company, airless nozzle). The atomized fuel formed a cone-shaped population of droplets traveling from the atomizing nozzle to the catalyst surface inside the reaction chamber. From the data sheet of atomizing nozzle, the spray angle of the droplet cone was between 50° and 55°, and the diameter of individual droplets was between 50 μm and 100 μm depends on injection pressure. The initial distance between the nozzle tip and the catalyst layer was ensured to be smaller than 2cm, a value chosen to allow droplets impinge over the entire catalyst layer without hitting the chamber side walls when accounting for the droplet cone angle. The glass version of reactor cylinder, shown in Figure 4.3, enabled visualization of droplet spraying and impingement zones during the injection of fuel (and ensured all fuel droplets reached the heated catalyst surface and instantaneously evaporated).

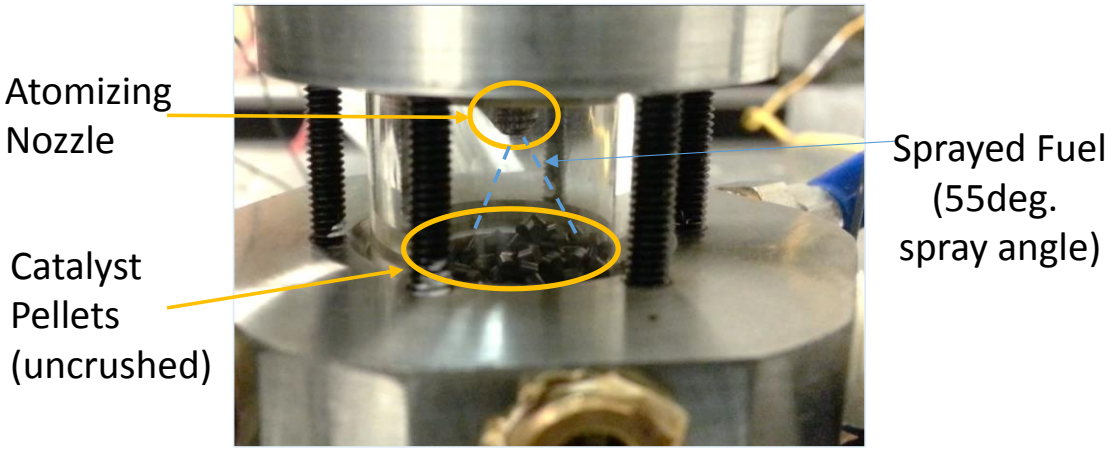

Figure 4.3 Glass reactor cylinder enables visualization of droplet injection/fuel evaporation process. Picture was taken at the moment of spray (over 30ms). Immediate evaporation of the injected fuel with corresponding pressure rise is visually observed during fuel injection experiments.

4.1.4 Variation of reactor volume

Volume variation in CHAMP-DDIR was achieved by moving the piston with a linear actuator. The linear actuator is composed of stepper motor (NEMA 17), a linear stage (Newmark NLS4), and a motor motion controller (Newport NCS-A1). Its maximum load is 289 N (60 lbs), which allows compression of the reactor chamber to 12×10^5 Pa considering 2.45cm^2 reactor cross section. In experiments, the maximum pressure in the chamber was limited by the mechanical strength of the thin membrane foil and kept below 5×10^5 Pa (safety factor = maximum allowable pressure/ pressure ~ 2). The motion of the linear actuator was controlled via a custom developed LabView program, employing either piston velocity control or reactor pressure feedback control and using input from the pressure transducer. The inner diameter of reaction chamber is 17.5mm, height varies from 2.5mm to 20mm (volume varying from 0.6cc to 4.8cc). Dead volume includes compressed volume in reaction chamber and flow and instrumentation ports, and the total volume is 1.2cc (20% of total volume, hence the maximum compression ratio is about 5.)

4.1.5 Heating and insulation

Four cartridge heaters (15W each, Sun Electric) were embedded into the heater/permeation block to supply heat to the reaction chamber. The main purpose of the heaters is to control the temperature of the collocated catalyst and membrane. A 24 V automatic temperature controller (Harrick ATV-1) was used to control power to the cartridge heaters. The heaters were operated in either target temperature mode or constant power mode. The heater/permeation block, made of aluminum (chosen for its high thermal conductivity), was continuously heated and also provided a path for flow of the argon sweep gas (Figure 4.1). The high temperature sweep gas provided convective heating of the membrane and, through it, the catalyst and impinging liquid fuel. Ceramic fiber insulation blankets (Wetpack, RSI Fibre) covered the reactor block and cylinder for insulation. One of the advantages of the CHAMP-DDIR prototype design derived from its low aspect ratio (height-to-diameter) is that the specific (per unit volume) area of the external walls are minimized, so the heat losses from the reactor chamber are significantly reduced.

4.1.6 Measurement of reaction conditions

Hydrogen production rate, fuel feed rate, temperature, and pressure are the main parameters that were monitored in real time during the CHAMP-DDIR cycle. Hydrogen production rate was measured with a mass spectrometer (Hiden Analytical Quadrapole HPR-20) by analyzing permeated hydrogen carried with the sweep gas. Argon was used as a sweep gas (flow rate of 50~250 sccm) to maintain low partial pressure of hydrogen on the permeate side of the membrane. The H_2 sampled during a reaction cycle was mixed with the sweep gas, and the H_2 generation rate were calculated using pre-acquired calibration data for the known sweep gas feed rate.

In order to get accurate quantitative data using the quadrupole mass spectrometer frequent calibration must be performed to calculate the relative sensitivity of the mass spectrometer to the gas species of interest [80]. This calibration involves supplying the mass

spectrometer with a gas mixture of known composition and monitoring the gas composition reported by the mass spectrometer to find relative sensitivity.

The injection fuel feed rate was adjusted with the micro solenoid valve controller (Spike and Hold Driver) by applying a pulsed voltage signal from a function generator (Agilent 33250A). The injection amount was also measured from reading of a syringe (Hamilton 500μL, 1750RN) that served as a fuel reservoir. Local temperatures in the reactor were measured with K-type thermocouples (OMEGA) in three locations - inside the catalyst layer, in the heating block, and in the piston block close to the top of reactor chamber. For monitoring pressure change in the reaction chamber, a miniature ruggedized pressure transducer, Kulite XTEL-190, was installed on the main reactor block. A custom designed LabView program was used to communicate with a data acquisition unit (Agilent 34972A), the mass spectrometer, and the linear actuator controller and to enable real-time measurement visualization as well as data storage.

4.1.7 Measurement uncertainties and error propagation

The measurement of temperature, pressure, fuel injection amount, and hydrogen production rate have associated uncertainties that must be considered when reporting results. The K-type thermocouples (OMEGA CHAL-0005) have a reported accuracy of ±2.2°C for the temperature range of the experiments per specification provided by manufacturer. The reported accuracy of pressure transducer is ±0.085bar (0.5% of 17 bar full scale output of sensor). Estimating the uncertainty of hydrogen production rate required more detailed error propagation analysis. The precision of the fuel injector (for the amount of injection in single pulse) was assessed by taking measurements of injected volume for 25 times (to achieve 10μL per dose). The mean and standard deviation for the 25 measurements were 10.0μL and 0.3μL. Hydrogen permeation rate, $\dot{J}_{H2}$, was calculated by multiplying relative partial pressure of H_2 (over partial pressure of Ar), p_{H2}/p_{Ar}, from mass spectrometer reading by the Ar molar flow rate, $\dot{J}_{Ar}$, and dividing by the relative

sensitivity (due to ionization cross-section of different species) of mass spectrometer signal to H_2, RS_{H2}.

$$\dot{J_{H2}} = \frac{(p_{H2}/p_{Ar})}{RS_{H2}} \dot{J_{Ar}} \tag{4.1}$$

Consequently, the uncertainty in $\dot{J_{H2}}$ was ±2.87% which was calculated from the error in flow rate of the sweep gas (±2.5% for 200sccm) and the error in mass spectrometer's partial pressure readings (±1%),

$$e_{\dot{J_{H2}}} = \sqrt{\left[\left(\frac{\partial \dot{J_{H2}}}{\partial p_{H2}}\right) e_{p_{H2}}\right]^2 + \left[\left(\frac{\partial \dot{J_{H2}}}{\partial p_{Ar}}\right) e_{p_{Ar}}\right]^2 + \left[\left(\frac{\partial \dot{J_{H2}}}{\partial \dot{J_{Ar}}}\right) e_{\dot{J_{Ar}}}\right]^2} \tag{4.2}$$

4.2 Baseline Experimental Procedure

The procedure for performing an experimental run for a CHAMP-DDIR baseline cycle was as follows (also refer to Figures 2.3 and 4.1):

i) The entire reactor system including reaction chamber and flow paths was purged with argon, the piston was moved to the specified initial position (2cm above the catalyst layer when fully retracted), and all valves were closed. Argon sweep gas was continuously flowing on the permeate side of the membrane. The reactor was heated to a pre-assigned temperature.

ii) A controlled amount of liquid fuel was spray-injected into the reaction chamber by applying a pulsed voltage signal to the micro valve controller.

iii) As soon as liquid fuel had evaporated on the catalyst surface, reaction and permeation took place concurrently. At the same time, the reactor height was adjusted with the linear actuator to achieve a desired pressure trajectory. During this step, permeated hydrogen was continuously swept by the argon gas and sent to the mass spectrometer, while pressure and temperatures in reaction chamber were monitored and recorded.

iv) Once the reaction and separation processes reach target completion criteria (such as desired hydrogen yield or fuel conversion), the remaining gases were exhausted from the reaction chamber to complete the cycle. The exhaust gases were sent to the mass spectrometer to be analyzed for the extent of methanol conversion. The piston was moved to its lowest position to minimize volume while argon expelled the remaining products. Once argon fills the dead volume of the reactor, a new cycle was ready to start. The experiment was repeated several times to ensure reproducibility of results.

4.3 Experiment Results

With the CHAMP-DDIR prototype, we investigated the effect of volume variation during cycle and dynamic modulation of fuel injection separately to assess the benefits of each mode. For this purpose, four sets of tests were performed. The first set included baseline constant volume operation for two different temperatures. The second set was variable volume operation with three volume/pressure trajectories. For the third and fourth test sets, time-modulated fuel injections were applied with varying duty cycle/frequencies (3rd) and several different fixed reactor volumes (4th).

4.3.1 Baseline experiment - constant reactor volume, single fuel injection

For the baseline CHAMP-DDIR experiment, constant volume operation with a single shot fuel injection (12μL) was conducted. Throughout each reaction cycle, the reactor was heated with constant power and data for two different heating power levels resulting in average catalyst temperatures 474K and 496K were recorded. Figure 4.4 shows representative results for the reactor's pressure, temperature at catalyst, hydrogen production rate, and hydrogen yield efficiency, Y_{H_2}, which is the ratio of actual hydrogen yield, J_{H_2}, to the ideal quantity of hydrogen that could be generated from fuel mixture via MSR, i.e., $3\,N_{CH_3OH,init}$: $Y_{H_2} = J_{H_2}/3N_{CH_3OH,init}$. These results are useful both to

benchmark performance when considering other operating modalities, and also to establish a firm understanding of the physical processes that occur throughout the cycle.

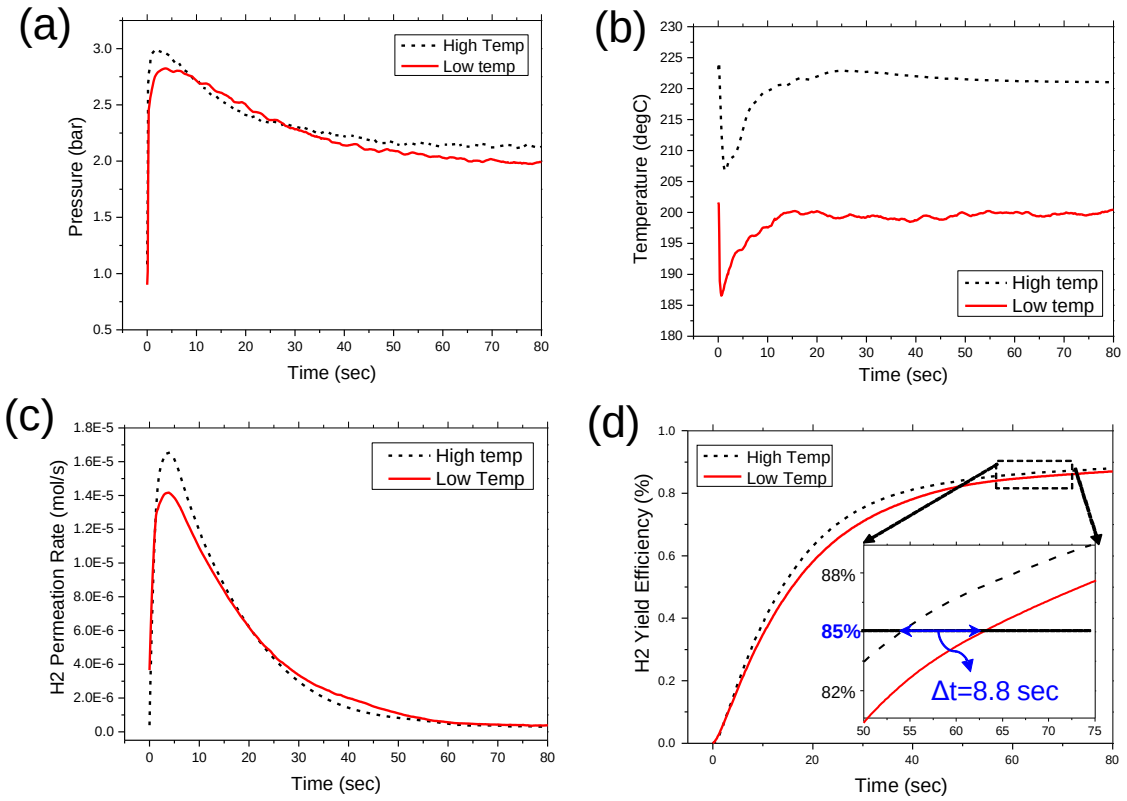

Figure 4.4 Constant volume experiment results: (a) pressure, (b) temperature at catalyst, (c) H_2 permeation rate, and (d) H_2 yield efficiency, for two different heating conditions. The average catalyst temperatures of two runs were 474 K (denoted as "low temp") and 496 K (denoted as "high temp"). 12μL of fuel (1:1 molar mixture of methanol and water) was injected at the beginning of cycle for both runs. Piston height was fixed at 2cm above the catalyst layer and the resulting reactor volume was 6cc. The inset in (d) shows the cycle time for 85% H_2 yield efficiency with higher temperature operation is 8.8sec shorter than with lower temperature operation, corresponding to 14.5% increase in hydrogen yield rate.

As seen in Figure 4.4a, pressure increases initially. This is due to combined effects of the vaporization of the liquid fuel and an increase in the total number of moles in the reactor due to the stoichiometry of the catalytic reactions, which is predominately methanol steam reforming. These two effects exceed the pressure reduction that would have occurred due to decreasing temperature, induced by heat consumption needed for heating the injected (cold) fuel and its vaporization as well as energy input required by the endothermic

reactions. Eventually, pressure starts decreasing because the molar rate of hydrogen removal through the membrane exceeds the net molar production rate in the reactor, which dominates the effect of the concurrent temperature rise due to continuous external heating (Figure 4.4b). For the higher temperature run, the average and final pressures are higher, and the resulting higher rates for reaction, increased membrane permeability, and larger driving force for permeation associated with higher hydrogen partial pressure collectively produce a greater maximum rate of pressure decrease.

The temperature of CHAMP-DDIR, displayed for the two baseline operation cases in Figure 4.4b, is temporarily sunk by processes that lower the energy of the system, such as evaporation of the fuel, endothermic reaction, and heat losses, but eventually recovered to a desired nearly constant level in constant volume operation by heat supplied from the heaters. For a given fuel amount the magnitude of heat input required for evaporation and reaction are of a similar magnitude ($\Delta H_{Water,evap}$=40.66kJ/mol, $\Delta H_{Methanol,evap}$=32.94kJ/mol, and ΔH_{MSR}=49.2kJ.mol), but the time scale predicted for evaporation is 3 orders of magnitude smaller than that for reaction time scale [19]. As a result, the catalyst temperature drops immediately after the fuel sprayed on to it, as the catalyst provides the majority of energy input for evaporation [16]. The magnitude of the catalyst temperature drop was about 17K, which indicates that about 60% of the energy required to heat and vaporize the fuel is drawn directly from the catalyst. The remainder is supplied from the reactor wall and heater block and the heated gas in the reactor volume. After the initial temperature drop, the catalyst temperature recovers by the heat supplied from heaters, which exceeds the heat consumed by the endothermic steam reforming reaction and lost to the surroundings. After about 15 seconds, temperature almost fully reaches the initial temperature and is stabilized.

The temperature uniformity was assessed by comparing measurements from multiple locations in the reactor, including the top of the reaction chamber, bottom of the reaction

chamber (at catalyst), the reactor side wall, and the heater block below the membrane. When the piston in the reactor is fully retracted to 2cm above the catalyst layer, the catalyst temperature, which is at the bottom of the reaction chamber, was about 40 K higher than the temperature measured at the top of the reactor chamber. This 20 K/cm gradient results primarily from heat losses through the reactor side walls, and is significant; nevertheless, the impact of the axial temperature gradient on the reaction and permeation rates is minimized because the heaters supply heat from the bottom of the device, where the membrane and catalyst are collocated. The major effects of temperature on the reactor performance are through the rate constants of chemical reactions and permeability of the membrane, which are controlled by the local temperature at the collocated catalyst/membrane, and not the bulk temperature. By applying heat directly adjacent to the membrane/catalyst layer, effective thermal control is obtained, resulting in an elimination of heat transfer limitations on performance in its traditional meaning. However, non-uniformity in temperature does impact the reactor performance indirectly through its influence on the reactor bulk pressure and diffusion coefficients of species in the gas phase. A practical benefit of the thermal non-uniformity, with the lowest reactor temperature at the piston, manifests in the minimization of evaporation and boiling of the liquid fuel in the injection line prior to atomization, ensuring more precise control of the injected volume. The latest design ensures the temperature of the fuel path in the piston is maintained below the saturation temperature of methanol. (The error in the volume of fuel injection is about 3%.) Comparing the results of the two baseline cycles at different average temperatures, the hydrogen production rate (Figure 4.4c) was initially higher in the higher temperature cycle due to increased rates for both endothermic MSR reaction and permeation, and these higher production and hydrogen separation rates have lasting effect on the performance throughout the cycle. As a result, the time to reach 85% of hydrogen yield efficiency (the ratio of actual hydrogen yield to the ideal quantity of hydrogen that could be generated

from fuel mixture) with high temperature operation was 14.5% shorter than that with low temperature (Figure 4.4d), which accordingly enhances the volumetric power density.

4.3.2 Variable reactor volume, single injection experiments

From the findings in the previous study which classified CHAMP-DDIR's operational regimes with theoretical analysis, the hydrogen yield is limited by permeation through the membrane under the operating conditions of these experiments. The driving force for permeation of hydrogen through the membrane is the difference in partial pressure of hydrogen across the hydrogen selective membrane. As hydrogen becomes depleted in the reactor, the permeation rate decreases. Momentarily, by compressing the volume of the reactor, the hydrogen permeation rate can be maintained above the baseline (constant volume) rate. To demonstrate this effect, experiments were performed with the piston moving down during the cycle in order to maintain an elevated partial pressure of hydrogen.

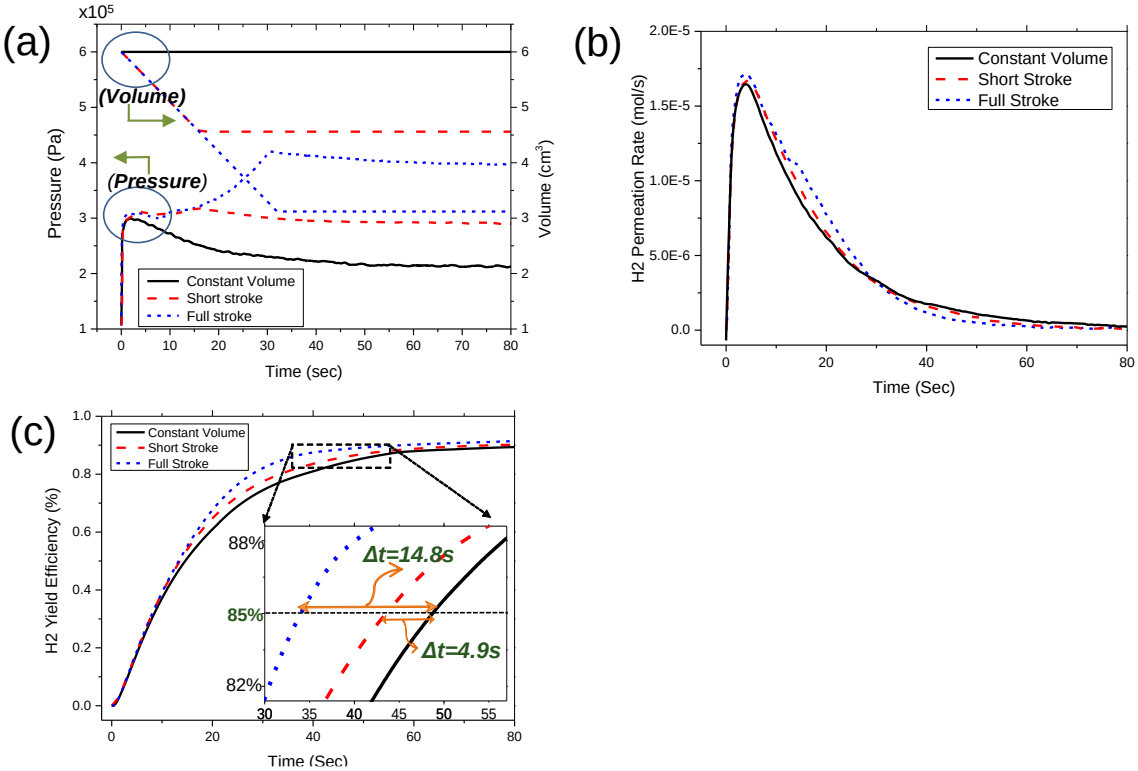

Figure 4.5 Variable volume operation experimental results: (a) pressure and volume, (b) H2 permeation rate, and (c) H2 yield efficiency. Initial reactor volume was 6cc for all three runs with reactor volume and pressure varied, following the trajectories depicted in (a). The average temperature was 496 K and injected fuel amount was 12μL for all runs. The inset in (c) shows the cycle time for 85% hydrogen yield efficiency with a short stroke compression cycle and a full stroke cycle, which are reduced by 4.9 sec (11%) and 14.8 sec (29%), respectively, compared to that of constant volume operation.

In Figure 4.5, reactor pressure, hydrogen production rate, and hydrogen yield efficiency are compared for experiments with different volume change trajectories: (1) constant volume operation with a piston height extended to 2cm above bottom/catalyst surface, (2) variable volume operation with the piston moving down from its top position (2cm above catalyst) at 0.4mm/sec during the first 16sec following fuel injection, resulting in a 24% reduction in reactor volume; and, (3) variable volume operation with the piston moving down from 2cm at 0.4mm/sec during the first 32sec following fuel injection, resulting in a 48% reduction in reactor volume. The shorter duration compression maintained the reactor

pressure close to constant at the maximum pressure achieved in constant volume operation. The same amount of fuel, 12μL, was injected in all experiments.

A clear enhancement of the hydrogen permeation rate is observed when the volume is compressed in a mid-cycle. This is primarily due to the increased partial pressure of hydrogen in the reactor, which increases the driving force for permeation. As a result, variable volume operation enabled shorter cycle times for the same amount of hydrogen yield. For example, the time for 85% hydrogen yield efficiency with the short stroke cycle (2) and the full stroke cycle (3) were reduced by 11% and 29%, respectively, as compared to that of constant volume operation. This reduction in cycle completion time translates into an improvement in volumetric power density, $\omega = \left(J_{H_2} LHV_{H_2} - \mathrm{E_{in}}\right)/\left(\mathrm{V}_{max} \cdot t_{cycle}\right)$, defined as the total number of moles of H_2 that permeate out of the reactor (H_2 yield), J_{H_2}, multiplied by the lower heating value of hydrogen, LHV_{H2}, minus the total energy input to the system, E_{in}, divided by the product of the maximum reactor volume during the cycle, V_{max}, and the cycle period, t_{cycle}. In calculating the power density, the total energy input, E_{in}, is the sum of the work for piston compression ($\mathrm{W_{piston}} = \int \mathrm{PdV}$) and the required heat for evaporation, endothermic reaction and raising fuel temperature to target level for the reaction (T_{rxn}). Figure 4.6 compares the volumetric power density for different target hydrogen yield efficiencies for the three different volume trajectories, experimentally assessed in Figures 4.4 and 4.5.

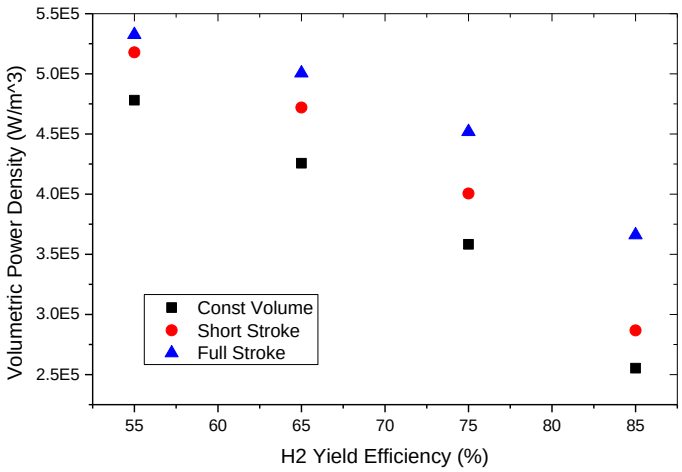

Figure 4.6 Comparison of volumetric power density for fixed volume and variable volume operations at various H_2 yield efficiencies. The highest power density was achieved with the full stroke compression (48% reduction in initial reactor volume) operation primarily as a result of enhanced permeation accompanying increased hydrogen partial pressure. For 85% hydrogen yield efficiency, volumetric power densities were improved by 17% when the reactor volume was varied to maintain at the maximum pressure for the constant volume run, and by 42% when the reactor was compressed to reach 40% higher pressure than the maximum pressure for the constant volume run.

In addition to demonstrating the improvement in volumetric power density with variable volume operations, Figure 4.6 also corroborates a predicted, in chapter 3, tradeoff between volumetric power density and hydrogen yield efficiency, with increasing power density coming at the cost of reduced H_2 yield efficiency. Importantly, this tradeoff is mitigated when compression is used to maintain a high permeation driving force, obviating the requirement for long residence times to extract hydrogen at the end of the cycle when its low partial pressure decreases the driving force for permeation across the membrane. One of the observations from first the two sets of constant/variable volume experiments was that the initial amount of fuel injected determines the maximum pressure (at the constraint of reactor volume) and also the magnitude of the temperature drop. The maximum pressure is a limiting constraint on reactor operation due to membrane stability, and temperature drop lowers rates of catalytic reaction and membrane permeation. This motivated an

investigation on the impact of reactor performance of dynamically modulated fuel introduction.

4.3.3 Split injection of fuel in time-modulated pulses

One of the main objectives for time-modulated fuel injection is to prevent significant reduction in both reaction and permeation rates caused by the large temperature drop at the catalyst due to fuel evaporation during direct injection of liquid fuel. Instead of introducing the entire amount of fuel in one injection, by splitting the fuel introduction into multiple doses with optimized injection frequency and duty cycle, the elevated catalyst temperature can be maintained. We performed two series of experiments to investigate the impact of fuel injection modulation with results depicted in Figures 4.7 and 4.8.

4.3.3.1 Constant reactor volume with various split injection experiment

The first set of experiments for time modulated fuel injection was performed with fixed reactor volume and results are shown in Figure 4.7. The three trajectories shown in the plots differ in a sequences of fuel introduction: (1) single-shot injection, 15μL of fuel injected at the beginning of the cycle, (2) three split injections of 5μL each with a 2.5sec wait interval; and, (3) three split injections of 5μL each with a 5sec wait interval between consecutive injections. All experiments started with the same initial catalyst temperature, 475 K, and all had the same constant heating power applied throughout the cycle.

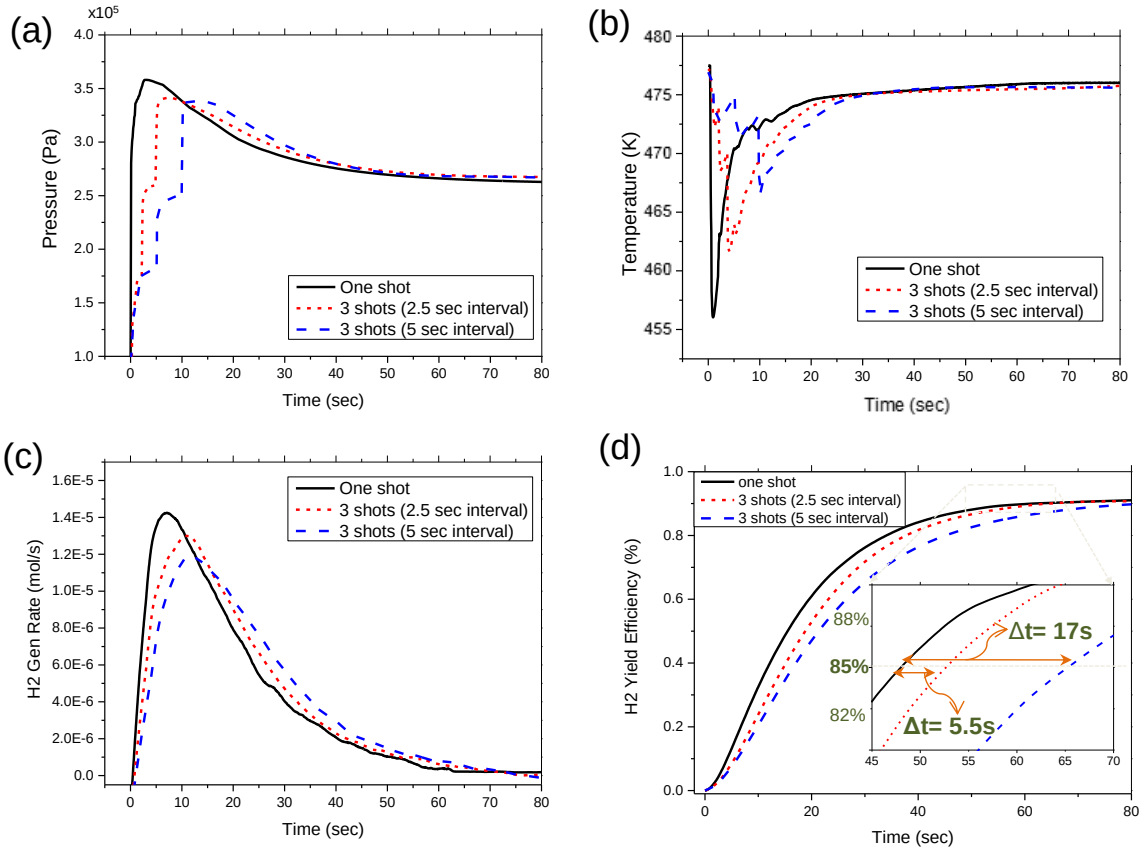

Figure 4.7 Time-modulated fuel injection with constant volume operation experimental results: (a) pressure, (b) temperature at catalyst, (c) H_2 permeation rate, and (d) H_2 yield efficiency, for three different fuel injection conditions. Total 15μL of liquid fuel was introduced with different duty cycles and frequencies for each run. The reactor volume was 6cc (kept constant) and initial temperature at catalyst was 475 K. For all runs, pressure and temperature responded immediately to fuel introductions. Hydrogen production was fastest with one shot injection compared to split injection runs due to higher average (and maximum) pressure and zero delay in residence time for introducing the total volume of fuel at once.

As can be seen in Figures 4.7a and 4.7b, when fuel was injected into the reactor, its vaporization caused a nearly instantaneous increase in pressure and decrease in catalyst temperature, and the magnitude of those changes were approximately proportional to the amount of fuel injected. For single-shot injection, the maximum pressure during the cycle was 3.65×10^5 Pa, which was higher than the pressure attained during either of two split shot injection experiments. Similarly, the initial temperature drop was larger at 21 K, and the temperature recovery time (the time from the initial injection until the catalyst temperature rose back to 473 K) was faster at 14sec, as compared to split injection cases.

The effect of multiple injections is that the sharp pressure rise and a catalyst temperature decrease is spread out over longer time and their magnitudes are diminished. Thus, although the maximum drop in temperature was reduced to 15 K (3 injections in 5 sec. time span) and 10 K (3 injection in 10 sec. time span) from 21 K (1 injection) through injection modulation, thus alleviating the reduction in reaction and permeation rates, there was also lower average pressure and longer temperature recovery time. Combined with the delay in availability of reactants at high concentration, these latter effects adversely affected reaction and permeation for the split-injection runs.

Comparison of the hydrogen generation rate behavior, Figure 4.7c, with the catalyst temperature and pressure evolution, Figures 4.7a and 4.7b, shows that the rate of H_2 production did not respond immediately to the rapid changes in catalyst temperature or reactor volume pressure. These experiments are performed in the membrane permeation dominated regime [19], and so hydrogen generation was determined primarily by the membrane permeance, a strong function of temperature, and the hydrogen partial pressure in the reactor. Thus the slow response of H_2 generation suggests that the membrane temperature did not change significantly, likely due to effective convective heating from the hot argon sweep gas.

The comparison of hydrogen yield efficiency in Figure 4.7d reveals that the split injection's detrimental effects were more significant than its positive effects on the reactor performance, with longer cycle times required to attain 85% hydrogen yield. Consequently, the anticipated benefit of time modulated fuel injection for volumetric power density was not realized in these constant volume experiments. When comparing performance at constant volume without any constraint on pressure for a reactor operating in the permeation limited regime, the immediate introduction of fuel achieves the highest hydrogen partial pressures and thus increases the permeation rate.

4.3.3.2 Constant, but different, reactor volume with split injection experiment

In fact, the maximum allowable pressure is a meaningful constraint for reactor operation since it is an important consideration in the design and operation of the reactor, in particular for membrane integrity [40]. Thus, a second set of fuel injection modulation experiments was conducted with the constraint of the same maximum pressure and total amount of fuel and results are shown in Figure 4.8.

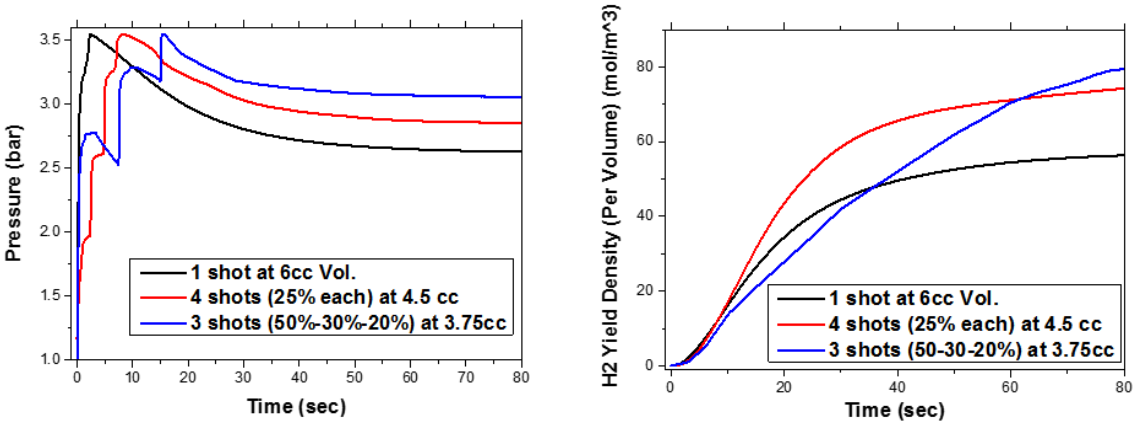

Figure 4.8 Results for time-modulated fuel injection experiments with constant, but different reactor volumes (6cc, 4.5cc, and 3.75cc): (a) pressure, and (b) H_2 yield density (per volume). Fuel was injected into the three different volume reactors differently to achieve the same maximum cycle pressure. A single injection was used for the large volume reactor (line in black), while smaller amount multiple injections spaced 3 sec (red) and 5 sec (blue) apart were used for the smaller volume reactors. Initially, the hydrogen generation rate is higher with the single shot/large volume operation as compared to the multi-shot/ small volume operation. However, because the smaller volume reactor maintains a higher pressure over most of the cycle, the smallest reactor displays much better hydrogen yield density (H_2 yield divided by volume).

All three experiments were performed at constant, but different, volumes to isolate the effect of split injection under constrained pressure on maximum required volume. For a single 14µL fuel injection experiment, a volume of 6cc was required to prevent pressure from exceeding 3.6×10^5 Pa (and temperature at 500K), while by injecting 3.5µL increments every 3 seconds the volume could be reduced by 25% to 4.5cc without exceeding 3.6×10^5 Pa. (and 3 shot injections with 7 µL- 4.2 µL - 2.8 µL spaced every 5 seconds requires 3.75cc reactor). Because of the smallest reactor volume, the pressure remained higher throughout the remainder of cycle resulting in higher cycle-averaged

pressure (recall that the peak maximum pressure is constrained to be the same for both cases under consideration). The enhancement of permeation rate due to the increased averaged pressure was able to compensate for the negative effect caused by delay in the fuel supply by multiple injection, with total cycle durations to achieve the same hydrogen yield (at 70% or higher) being similar. In addition, the mass transfer resistance is reduced with smaller reactor volume (bulk gas phase diffusion timescale is $\tau_D = H^2/D_{m,avg}$, where H is the size of the reactor, and $D_{m,avg}$ is the average of the multi-component mass diffusion coefficients, see chapter 5.4.3), therefore both fuel and produced hydrogen are more intact with catalyst and membrane with decreasing reactor height. Importantly, a significant improvement in volumetric power density is revealed as a result of combining time-modulated fuel introduction with reduced reactor volume as depicted in Figure 4.9.

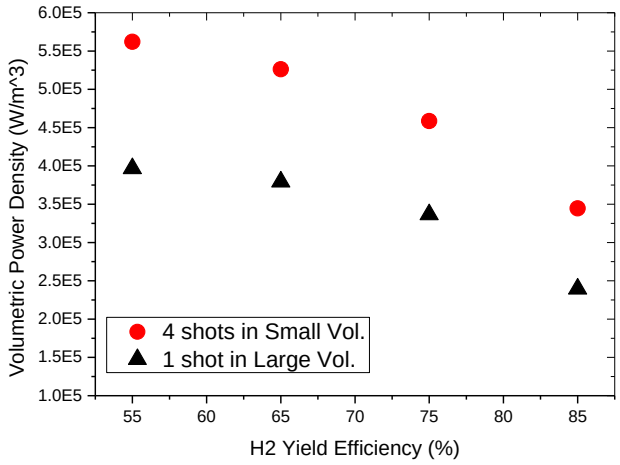

Figure 4.9 Comparison of volumetric power density for 4 shot injection in 4.5cc and single injection in 6cc fixed volume operations at various H2 yield efficiencies for the reactors operated under a constraint of the maximum peak pressure. Higher volumetric power density for multi injection run was achieved due to significant reduction in reactor volume. For 85% hydrogen yield efficiency, volumetric power densities were improved by 38% by splitting fuel injection into 4 shots and using a 25% smaller volume.

4.4 Conclusions

A variable volume membrane batch reactor with dynamically modulated liquid fuel introduction (CHAMP-DDIR) was experimentally characterized for hydrogen production via the methanol steam reforming reaction. The prototype CHAMP-DDIR consisted of an actively-controlled micro injector for liquid fuel atomization, a reactor chamber loaded with $Cu/ZnO/Al_2O_3$ catalyst for MSR and having a dynamically-modulated volume via piston motion controlled by a linear actuator, and Pd–Ag foil membrane for in situ 100% selective hydrogen extraction from the reaction products. The benefits of the two modes of CHAMP-DDIR operation, pulse-modulated fuel injection and batch reaction with actively maintained constant chamber pressure via dynamically-adjusted reactor volume, were demonstrated and their impact on performance was quantified. The experimental results showed that the required cycle time for achieving a target hydrogen yield can be substantially reduced by compressing the reactor volume during conversion cycle, due to enhanced permeation of hydrogen resulting from an ability to maintain an elevated reactor pressure despite hydrogen removal. In addition, pulse-modulated fuel injection experiments revealed that a significant reduction in required initial reactor volume can be realized with multi-shot split fuel introduction when reactor operation is dictated by a design constraint on the maximum allowable reactor pressure. Both the reduced cycle time and smaller reactor volume translate into substantially improved volumetric power density, which is of importance for portable and mobile applications of hydrogen based power sources. In addition, the enhanced power density and potential for hydrogen throughput control enabled by actively-modulated pressure demonstrate the value of CHAMP-DDIR for applications such as transportation, for which high power density and the ability to meet time varying power demands are important.

Lastly, it should be noted that in all experiments the batch reactor performance was evaluated for a single cycle, ignoring the time required to discharge the reactor content

(unreacted fuel and non-permeated products) between cycles. For the tested operations, the discharge time (~1s) could be realized using forced purge by inert argon gas and it was relatively short compared to total cycle time (35~65s) to be safely neglected in the analysis. However, under practical operating conditions, the penalty for the discharge down time may not be so negligible and quasi-steady performance values averaged over multiple cycles should be used to assess performance of a continuously operated reactor [14].

CHAPTER 5

COMPREHENSIVE MODEL

A comprehensive reactor model which carefully considers the effects of heat and mass transfer, including rigorous treatment of multi-component species transport is presented in this chapter. In order to establish a framework for discussion of results, the time evolution of reactor parameters in single cycle simulations (for constant volume and constant pressure operations) is first discussed in detail. Then, the model is validated against experimental results through comparison of predicted and measured hydrogen production rate, reactor pressure, and temperature. The experimentally validated model is used to identify the relationship between CHAMP-DDIR design and operating parameters, and to determine the rate-limiting process(es) that govern reactor output. In addition, heat and mass transfer effects on CHAMP-DDIR performance are investigated by comparing the predictions among multiple cases, using models of an increasing level of complexity for simulating the transport phenomena within the reactor.

5.1 1-D CHAMP-DDIR Reaction-Permeation-Transport Model

A comprehensive first principle reactor model that couples catalytic reactions, multispecies mass transport, heat transfer, and membrane permeation phenomena was developed and used to analyze the performance characteristics of CHAMP-DDIR. The model is one-dimensional and formulated for CHAMP-DDIR reactor schematically depicted in Figure 5.1. A porous catalyst layer of porosity ε_{cat}, density ρ_{cat}, and mass m_{cat} is integrated with a hydrogen selective membrane of thickness δ_{memb} at the bottom of reactor (at z=0). The volume of the reaction chamber varies as position of piston changes during a batch reaction cycle, i.e., the location of one boundary is time dependent, $z=H(t)$. At the permeate (bottom) side of the membrane, heated argon gas (at temperature, $T_{sweep,}$ and flow rate,

$\dot{N}_{sweep}$) flows to sweep the generated hydrogen out of the permeated zone at flow rate $\dot{J}_{H2,perm}$, while convectively heating the membrane. In the reaction chamber, the concentration of each gas species *i*, $c_i(z,t)$, temperature, $T(z,t)$, and pressure, $P(t)$, vary during the reaction cycle due to coupled transport, reaction and hydrogen permeation.

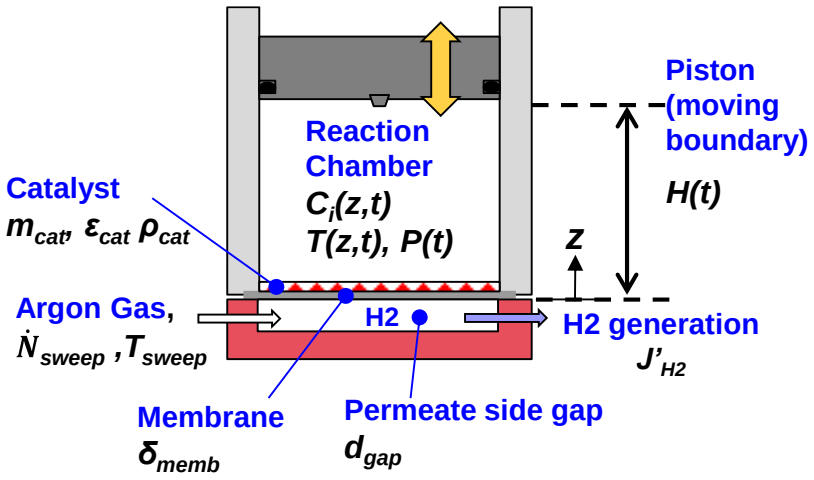

Figure 5.1 CHAMP-DDIR schematics, showing dimensions, process properties and major domains for model formulation.

5.1.1 Model assumptions

The comprehensive model is formulated based on the following simplifications: (i) at the temperatures and pressure under consideration, all components of mixture in the reactor can be treated as ideal gases, (ii) the Maxwell-Stefan formalism accurately describes the multispecies diffusive fluxes, (iii) at any given time, a uniform pressure exists in the reactor,[15] (iv) hydrogen permeation across the membrane is diffusion-limited, and the membrane surface coverage by other species in the reactor, which reduces the permeance, is accounted for via equilibrium equations assuming rapid adsorption and desorption [69], (iv) an effect of intra-particle diffusion and mass transport limitations within the thin catalyst layer is negligible and the temperature gradient within the catalyst layer is sufficiently small that a single effective catalyst temperature can be used, (v) rates of catalytic reactions are accurately described by Peppley's kinetic model, [68] and (vi) vaporization occurs instantly, due to being very fast as compared to the dominant process

time scales (bulk species diffusion and hydrogen permeation), after fuel is sprayed onto a heated catalyst in the reactor.[16]

For determining the mass transfer effect in the catalyst layer, Weisz-Prater[96] or Mears' criterion[97] were evaluated. Weisz-Prater criteria evaluates importance of internal mass transfer effect and Mears' criterion evaluates importance of external mass transfer effect. Both of them compared with relative timescale of chemical reaction for simplification of model and determination of reaction kinetics (e.g. intrinsic or apparent rates). For our analysis, internal mass transfer is neglected, whereas external mass transfer is included. The detailed calculations for Weisz-Prater and Mears' criterion are shown in Appendix F.

5.1.2 Conservation equations

Species concentrations are found by numerically solving the 1-D species transport equations, Eq. (5.1). The catalytic reforming reaction is incorporated into the boundary condition for the species transport equations, and thus there is no volumetric source term in Eq. (5.1):

$$\underbrace{\frac{\partial c_i}{\partial t}}_{\substack{\text{rate of change}\\ \text{in moles of species i}\\ \text{per unit volume}}} = - \underbrace{\frac{\partial}{\partial z}(c_i v)}_{\substack{\text{net rate of change}\\ \text{in moles of species i}\\ \text{per unit volume}\\ \text{by convection}}} - \underbrace{\frac{\partial}{\partial z} J_i}_{\substack{\text{net rate of change}\\ \text{in moles of species i}\\ \text{per unit volume}\\ \text{by diffusion}}} \tag{5.1}$$

In Eq (5.1), c_i is concentration of species i and v is molar average velocity. The diffusive flux of each species $\boldsymbol{J}_i$, relative to the molar average velocity, is determined by simultaneous solution of the Maxwell-Stefan multicomponent diffusion equations [81, 82]:

$$\nabla x_i = - \sum_{j=1, j\neq i}^{N} \frac{x_j J_i - x_i J_j}{c_T \mathbb{D}_{ij}} \qquad i=1, N \tag{5.2}$$

where x_i is mole fraction of species i , $\mathcal{D}_{ij}$ is the Maxwell-Stefan diffusivity between ith and jth species ([83, 84]), and c_T is total concentration given by summation of all individual species concentrations. N is the total number of species considered (=6), including methanol, steam, hydrogen, carbon dioxide, carbon monoxide and argon. Although Eq. (5.2) applies to all six species, the resulting six equations are not linearly independent. Therefore, following the standard method for multispecies diffusion described via the Maxwell-Stefan relations, the number of equations is reduced by one, and one species is eliminated, using the facts that, by definition, the sum of diffusive fluxes is zero, i.e., $J_N = -\sum_{i=1}^{N-1} J_i$, and the sum of the mole fractions is unity, i.e., $x_N = 1 - \sum_{i=1}^{N-1} x_i$. The resulting system of (N-1) equations can be written in a vector/matrix form as

$$c_T \left(\frac{d\vec{x}}{dz} \right) = -[B]\vec{J} \tag{5.3a}$$

where $\vec{x}$ is a column vector containing the mole fractions x_i as its N-1 elements, $\vec{J}$ is a column vector comprised of the species molar diffusive fluxes, and [B] is an (N-1) × (N-1) dimensional matrix [18]

$$[B] = \begin{cases} x_i \left(\frac{1}{\mathcal{D}_{iN}} - \frac{1}{\mathcal{D}_{ij}} \right) & i \neq j \\ \frac{1}{\mathcal{D}_{iN}} + \sum_{\substack{j=1 \\ j \neq i}}^{N} x_j \left(\frac{1}{\mathcal{D}_{ij}} - \frac{1}{\mathcal{D}_{iN}} \right) & i = j \end{cases} \tag{5.3b}$$

Vector that composed of diffusive flux for each species, $\boldsymbol{J}_i$, is found by taking inverse of [B] matrix from Eq. (5.3a)

$$\vec{J} = -c_T B^{-1} \frac{\partial}{\partial z} \left(\frac{\vec{c}}{c_T} \right) \tag{5.3c}$$

Then, the species molar fluxes can be compactly expressed as $\vec{N} = \vec{c}v - c_T B^{-1} \partial/\partial z\left(\vec{c}/c_T\right)$ where each element of the vector $\vec{N}$, N_i is the total molar flux of species *i*, and the species conservation equations, Eq. (5.4), can be rewritten as

$$\frac{\partial \vec{c}}{\partial t} = -\frac{\partial}{\partial z}\vec{N} \tag{5.4}$$

The spatially uniform pressure (due to fast mechanical equilibration on the time scale of sound wave propagation) in the non-isothermal reactor is also determined using Eq. (5.5), which is modified from ideal gas equation of state [13]

$$P = N_T R_u \Big/ \int_0^L \frac{dz}{T(z)} \tag{5.5}$$

where N_T is the total number of moles (per unit area) of gas in the reactor, R_u is the universal gas constant and $T(z)$ is the local temperature. The mole average velocity is given by the continuity equation based on transient evolution of the total concentration field,

$$\frac{\partial c_T}{\partial t} = -\frac{\partial}{\partial z}\left(c_T v\right) \tag{5.6}$$

Eq. (5.6) requires one boundary condition, either at the membrane (bottom) boundary, where $v_{z=0}$ is determined from a balance between molar fluxes due to reaction and permeation, or at the piston (top) boundary, where $v_{z=H}$ is specified by the imposed trajectory of the piston motion. As we have shown previously in chapter 3, the use of either boundary condition leads to identical results.

Lastly, the temperature profile in the reactor, *T(z),* is found through solution of the energy conservation equation.

$$\underbrace{\frac{\partial}{\partial t}\left(\sum_i c_i \bar{h}_i\right)}_{\substack{\text{time rate change}\\ \text{of energy in}\\ \text{unit volume}}} + \underbrace{\frac{\partial}{\partial z}\left(\sum_i (c_i v + J_i)\bar{h}_i\right)}_{\substack{\text{rate change of energy}\\ \text{due to species transport}}} = \underbrace{\frac{\partial}{\partial z}\left(k_{eff}\frac{\partial T}{\partial z}\right)}_{\substack{\text{rate change of}\\ \text{energy by}\\ \text{conduction}}} + \underbrace{\frac{Dp}{Dt}}_{\substack{\text{rate change of}\\ \text{energy by}\\ \text{compression}}} \tag{5.7}$$

In Eq. (5.7) $\bar{h}_i$ is molar enthalpy of species *i* and k_{eff} is effective thermal conductivity of the gas mixture, which is a function of local gas composition[85]. Changes in kinetic and potential energy, viscous dissipation, and radiation heat transfer are neglected. In our analysis, the Dufour effect, which is defined as energy flux due to a mass concentration gradient, is considered via the term $\frac{\partial}{\partial z}\left(\sum_i J_i \bar{h}_i\right)$; whereas the Soret effect, which is diffusional flux induced by temperature gradient, is neglected. This simplification is justified in in Appendix G. [82] For an ideal gas mixture and spatially isobaric condition, and using an effective temperature to calculate molar specific heats, $\bar{c}_{p,i}$ Eq. (5.7) becomes

$$\frac{\partial}{\partial t}\left(\sum_i c_i \bar{c}_{p,i} T\right) + \frac{\partial}{\partial z}\left(\sum_i (c_i v + J_i)\bar{c}_{p,i} T\right) = \frac{\partial}{\partial z}\left(k_{eff}\frac{\partial T}{\partial z}\right) + \frac{dp}{dt} \tag{5.8}$$

Equations (5.1) and (5.8) are the governing equations which describe the local conditions within the CHAMP-DDIR reactor when combined with the appropriate boundary and initial conditions to specify mode of operation.

5.1.3 Boundary conditions

The matrix system of differential equations (7) for species concentrations is second order in space (since the molar fluxes are defined through concentration derivatives) and thus requires boundary conditions at both the reactor top and bottom boundaries (Figures 5.1 and 5.2). At the top of the reaction chamber, *z=H(t)*, the boundary conditions for all species are those of impermeability, which yield

$$\boldsymbol{N}_{i,z=H} = c_i U_P \tag{5.9}$$

At the catalyst/membrane surface, *z*=0, the boundary conditions balance the molar fluxes with the catalytic reaction and hydrogen selective permeation through the membrane:

$$\boldsymbol{N}_{CH3OH,z=0} = \rho_{cat} m_{cat}(-r_{MSR} - r_{MD})$$
$$\boldsymbol{N}_{H2O,z=0} = \rho_{cat} m_{cat}(-r_{MSR} - r_{WGS})$$

$$\boldsymbol{N}_{CO2,z=0} = \rho_{cat} m_{cat}(r_{MSR} + r_{WGS}) \qquad (5.10)$$
$$\boldsymbol{N}_{H2,z=0} = \rho_{cat} m_{cat}(3r_{MSR} + r_{WGS} + 2r_{MD}) - J''_{H2,pern}$$
$$\boldsymbol{N}_{CO,z=0} = \rho_{cat} m_{cat}(-r_{WGS} + r_{MD})$$

The reaction rates (r_{MSR}, r_{WGS}, and r_{MD}) are the rates of methanol steam reforming, water gas shift, and methanol decomposition, i.e., Eqs. (2.1)-(2.3), respectively, and are given by Peppley's kinetic model. They are functions of catalyst temperature and the partial pressures of all species[68]. $J''_{H2,perm}$ is the hydrogen flux leaving the reaction chamber through the membrane, and is calculated using the model for hydrogen permeation across a Pd-Ag membrane presented by Israni et al.[69]

$$J''_{H2,perm} = \frac{D_{memb}}{\delta_{\text{memb}}} \theta (p_{ret,H2}^{0.5} - p_{perm,H2}^{0.5}) \qquad (5.11)$$

where $p_{ret,H2}$ is the partial pressure of hydrogen on the reactor (retentate) side of the membrane, $p_{perm,H2}$ is the partial pressure of hydrogen on the back (permeate) side of the membrane[19], D_{memb} is the diffusion coefficient for hydrogen atoms in the bulk Pd-Ag, and can be taken from literature, e.g., McLeod et al.[86]), and δ_{memb} is the membrane thickness. Israni's model, Eq. (14), assumes that diffusion of H atoms through Pd-Ag lattice is the rate limiting process for the transport of hydrogen across the membrane, i.e. permeation follows Sievert's Law, and accounts for the reduction of permeance due to competitive adsorption of CH_3OH, H_2O, CO_2, and CO on the membrane surface, through the permeation reduction factor, θ, which can range from 0 to 1 (it is unity when the membrane is exposed to pure hydrogen, and decreases with an increase in adsorption of non-H_2 species). The details for deriving θ and $p_{perm,H2}$ are discussed chapter 3 and Appendix B.

Similarly, for the energy conservation equation, two boundary conditions are required, one for each side of the domain. For the moving (piston) wall at the top of the reactor a constant

temperature condition can be used because the timescale for change in the piston surface temperature is slow (due to its high thermal mass) as compared to that for thin catalyst or membrane layers, so at $z=H(t)$

$$T_{z=H} = T_{wall}(\text{specified}) \tag{5.12}$$

The boundary condition at the bottom of reaction chamber, z=0, requires accurately accounting for the catalyst layer and selective membrane thermal masses and the thermal contact resistance between the catalyst and membrane. Therefore, energy balance is performed for the catalyst layer, as depicted in Figure 5.1, to obtain the time varying temperature of the catalyst, T_{cat}:

$$\underbrace{\left(\rho c_p\right)_{cat} d_{cat} \frac{dT_{cat}}{dt}}_{\text{Energy storage in the catalyst}} = \underbrace{-\frac{T_{cat}-T_{gas}}{R_{t,cond}}}_{\substack{\text{heat loss by} \\ \text{conduction into the gas}}} \underbrace{-\frac{T_{cat}-T_{memb}}{R_{t,cont}}}_{\substack{\text{heat gain via} \\ \text{heat transfer across} \\ \text{contact resistance to} \\ \text{membrane}}} \underbrace{-\rho_{cat} d_{cat} \sum_{j=1}^{Nrxn} \Delta H_j r_j}_{\substack{\text{heat sink/source due to} \\ \text{conversion of chemical to} \\ \text{thermal energy by reaction}}} \tag{5.13}$$

where d_{cat} is an effective thickness of the catalyst, k_{gas} is the effective conductivity of gas mixtures in the reactor at the chamber/catalyst interface, R_t is contact resistance between catalyst and membrane (taken from experimental study by Yovanovich [87]), ΔH_j is heat of reaction for reaction j (*MSR, MD, and WGS*), and r_j is the rate for j^{th} reaction. Similarly, an energy balance on the membrane yields the equation determining the membrane temperature T_{memb}:

$$\left(\rho c_p\right)_{memb} \delta_{memb} \frac{\partial T_{memb}}{\partial t} = -\frac{T_{memb}-T_{cat}}{R_t} - h_{m-s}(T_{memb}-T_{sweep}) \tag{5.14}$$

where δ_{memb} is the membrane thickness, and $h_{m\text{-}s}$ is the heat transfer coefficient of convective flow of heated sweep gas (Ar) over membrane on the permeate side, which is computed using the constant Nusselt number of 5.6 for fully developed laminar flow in the gap between membrane and heating block, i.e., $h_{m-s} = 5.6k_{Ar}/d_{gap}$. [88]

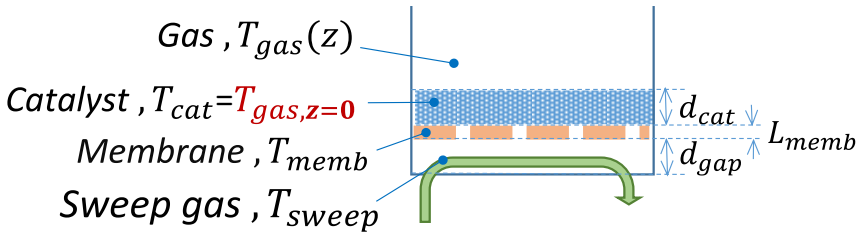

Figure 5.2 Schematic for deriving the energy balance boundary condition at z=0 (reaction/separation wall).

5.1.4 Initial conditions

Initial conditions for CHAMP-DDIR simulations cycle are based on the state immediately after the fuel is introduced into the reactor. As discussed in the model assumptions, the evaporation of fuel occurs instantaneously as compared to other, much slower processes in the reactor [16]. However, concentration and temperature distribution that accurately represent the actual conditions at the instant are not readily apparent, as evaporation of atomized fuel occurs both during the droplet transit from atomizing nozzle to catalyst and upon the contact on the catalyst surface. Therefore, we performed a numerical investigation of the impact of the initial conditions considering two limiting cases for species concentration resulting from droplets sprayed into a reaction chamber filled with argon: 55. The simulation results revealed that when the time scales for species diffusion in the reactor, reaction, and permeation are all of similar magnitude, the choice of an initial condition has a significant impact on the predicted reactor performance. On the other hand, when the time scale for reaction and/or permeation is much greater than the diffusion time scale, the choice of initial condition has little effect. For the result reported here, we have limited consideration to simulations when uniform initial molar fractions (with species concentrations match temperature profile) are assumed,

$$c_{i,0}(z) = c_{T,0}x_{i,0} = \frac{P_0}{RT_0(z)}x_{i,0} \tag{5.16}$$

where the initial species concentrations of species i at z is $c_{i,0}(z)$ are calculated based on total initial concentrations $c_{T,0}$ and initial molar fractions for species are

$$x_{CH_3OH,o} = x_{H_2O,o} = 0.5; \quad x_{CO_2,o} = x_{CO_2,o} = x_{CO,o} = 10^{-6} \quad (5.17)$$

The vanishingly small initial amounts of carbon dioxide, carbon monoxide, and hydrogen are provided to prevent singularities in numerical computations because these concentration appear as denominators in reaction rate expressions of Peppley kinetics.

The temperature profile prior to the fuel injection ($t=0^-$) is based on experimentally observed distribution, which shows an approximately linear decrease of 2K per 1mm along the reactor height from $T_{o-,z=0}$ at z=0 to yield $T_{o-,z=H_o} = T_{o-,z=0} - 2H_o$ (where units of H in $[mm]$ and T in $[K]$) at z=H.) Since instantaneous evaporation of injected (liquid) fuel is assumed, the temperature drop due to evaporation of fuel is taken into account at the beginning of the cycle and the initial temperature drop due to latent heat of evaporation is assumed to be supplied from capacitive thermal energy storage in the catalyst mass. As a result, the initial condition for temperature in the model is a discontinuous function:

$$\begin{aligned} &T_{o,z=0} = T_{o-,z=0} - \sum_{i=1}^{M,W} N_{i,o} u_{fg,i} \Big/ \left(\rho c_v\right)_{eff} \text{ at } z = 0 \\ &T_{o,z} = T_{o-,z=0} - 2z \text{ (where units of } \mathrm{H_{in}} \ [\mathrm{mm}] \text{ and } \mathrm{T_{in}} \ [\mathrm{K}]) \text{ for } 0 < z \le H_o \end{aligned} \quad (5.18)$$

$u_{fg,i}$ is internal energy change for vaporization, $N_{i,o}$ is initial number of moles of injected fuel, and $(\rho c_v)_{eff}$ is effective heat capacity of the porous catalyst layer. $T_{o-,z=0}$ is temperature at the catalyst/membrane surface (z=0) prior to injection (which is given).

5.1.5 Transformation of governing equations

The governing species transport equations, $\frac{\partial c_j}{\partial t} + \frac{\partial (c_j v)}{\partial z} = -\frac{\partial J_j}{\partial z}$ (Eq (5.1)), are spatially non-dimensionalized via the coordinate transformation, $z^* = \frac{z}{H(t)}$. This transformation allows for retaining of a fixed number of nodes in the numerical solution, with each inter-node spacing to shrink or grow in size based on the piston velocity, as z = 0 is transformed into the z^* = 0 point, and time varying piston position z= $H(t)$ is transformed into a fixed

z^* = 1. Using $\frac{\partial z^*}{\partial z} = \frac{1}{H(t)}$, and $\frac{\partial z^*}{\partial t} = \frac{-z}{[H(t)]^2} \cdot \frac{dH(t)}{dt} = \frac{-z^* U_p}{H(t)}$, the terms in Eq. (5.1) transform as follows:

$\frac{\partial c_j}{\partial t}$ becomes $\frac{\partial c_j}{\partial t} - \frac{z^* U_p}{H(t)} \frac{\partial c_j}{\partial z^*}$,

$\frac{\partial (c_j v)}{\partial z}$ becomes $\frac{1}{H(t)} \frac{\partial (c_j v)}{\partial z^*}$, and

$\frac{\partial J_j}{\partial z}$ becomes $\frac{1}{H(t)} \frac{\partial J_j^*}{\partial z^*}$,

where $U_p = \frac{dH(t)}{dt}$ is the piston velocity, and Maxwell-Stefan diffusive flux in the transformed coordinate system for species, J_j^* is j[th] element of the diffusive flux vector $\overrightarrow{J^*}$ where $\overrightarrow{J^*} = -\frac{1}{H(t)} c_T [B]^{-1} \frac{\partial}{\partial z^*} \left(\frac{1}{c_T} \vec{c} \right)$ and $\vec{c}$ is the species concentration vector. The resulting transformed species conservation equations

$$H(t) \frac{\partial c_j}{\partial t} - U_p z^* \frac{\partial c_j}{\partial z^*} + \frac{\partial}{\partial z^*} \left(c_j v + J_j^* \right) = 0 \tag{5.19a}$$

can be rewritten by applying chain rule, $H(t) \frac{\partial c_j}{\partial t} = \frac{\partial}{\partial t} \left(H(t) c_j \right) - U_p c_j$

and $U_p z^* \frac{\partial c_j}{\partial z^*} = U_p \frac{\partial}{\partial z^*} \left(z^* c_j \right) - U_p c_j$:

$$\frac{\partial}{\partial t} \left(H(t) c_j \right) + \frac{\partial}{\partial z^*} \left[c_j (v - U_p z^*) + J_j^* \right] = 0 \tag{5.19b}$$

Finally, Eq. (5.19b) is further simplified by recognizing $v - U_p z^*$ is the average molar velocity relative to the instantaneous local velocity of the moving dimensionless coordinate system, $v^* = v - U_p z^*$:

$$\frac{\partial}{\partial t} \left(H(t) c_j \right) + \frac{\partial}{\partial z^*} \left[c_j v^* + J_j^* \right] = 0 \tag{5.19c}$$

The energy conservation equation, starting with Eq. (8), $\frac{\partial}{\partial t}\left(\sum_j c_j \overline{c_{p_j}} T\right) + \frac{\partial}{\partial z}\left(\sum_j (c_j v + J_j) \overline{c_{p_j}} T\right) = \frac{\partial}{\partial z}\left(k_{eff} \frac{\partial T}{\partial z}\right) + \frac{dp}{dt}$, and following the same coordinate transformation from z to z* as above along with the chain rules

$\frac{\partial}{\partial t}\left(\sum_j c_j \overline{c_{p_j}} T\right) = \frac{\partial}{\partial t}\left(\sum_j c_j \overline{c_{p_j}} T\right) - \frac{z^* U_p}{H(t)} \frac{\partial}{\partial z^*}\left(\sum_j c_j \overline{c_{p_j}} T\right)$, and

$\frac{\partial}{\partial z}\left(\sum_j (c_j v + J_j) \overline{c_{p_j}} T\right) = \frac{1}{H(t)} \frac{\partial}{\partial z^*}\left(\sum_j (c_j v + J_j^*) \overline{c_{p_j}} T\right)$

energy conservation equation Eq. (5.8), can be transformed:

$$H(t) \frac{\partial}{\partial t}\left(\sum_j c_j \overline{c_{p_j}} T\right) + (-z^* U_P) \frac{\partial}{\partial z^*}\left(\sum_j c_j \overline{c_{p_j}} T\right) + \frac{\partial}{\partial z^*}\left(\sum_j (c_j v + J_j^*) \overline{c_{p_j}} T\right) = \frac{1}{H(t)} \frac{\partial}{\partial z^*}\left(k_{eff} \frac{\partial T}{\partial z^*}\right) + H(t) \frac{dp}{dt} \quad (5.20a)$$

which, using the chain rule to combine terms, $H(t) \frac{\partial}{\partial t}(\sum_j c_j \overline{c_{p_j}} T) = \frac{\partial}{\partial t}\left(H(t) \sum_j c_j \overline{c_{p_j}} T\right) - U_p(\sum_j c_j \overline{c_{p_j}} T)$ and $z^* U_P \frac{\partial}{\partial z^*}(\sum_j c_j \overline{c_{p_j}} T) = U_p \frac{\partial}{\partial z^*}\left(z^* \sum_j c_j \overline{c_{p_j}} T\right) - U_p(\sum_j c_j \overline{c_{p_j}} T)$, yields

$$\frac{\partial}{\partial t}\left(H(t) \sum_j c_j \overline{c_{p_j}} T\right) - U_P \frac{\partial}{\partial z^*}\left(z^* \sum_j c_j \overline{c_{p_j}} T\right) + \frac{\partial}{\partial z^*}\left(\sum_j (c_j v + J_j^*) \overline{c_{p_\iota}} T\right) = \frac{1}{H(t)} \frac{\partial}{\partial z^*}\left(k_{eff} \frac{\partial T}{\partial z^*}\right) + H(t) \frac{dp}{dt} \quad (5.20b)$$

Noting that coordinate transformation of the time derivative of pressure produces the z*-derivative of pressure, and this term is equal to zero because pressure is assumed to be uniform through the domain (therefore $\frac{dp}{dt}$ is in a total derivative form).

Eq. (5.20b) is put in its final form using v^* ($= v - U_p z^*$), the average molar velocity relative to the instantaneous local velocity of the moving dimensionless coordinate system:

$$\frac{\partial}{\partial t}\left(H(t)\sum_j c_j\overline{c_{p_j}}\,T\right)+\frac{\partial}{\partial z^*}\left(\sum_j\left(c_j v^*+J_j^*\right)\overline{c_{p_j}}\,T\right)=\frac{1}{H(t)}\frac{\partial}{\partial z^*}\left(k_{eff}\frac{\partial T}{\partial z^*}\right)+H(t)\frac{dp}{dt} \tag{5.20c}$$

The boundary conditions must also transformed. The boundary conditions for the species transport equations, Eqs. (5.9) and (5.10), are changed for the new coordinate z^*, with $\boldsymbol{N}_j^* = c_j v^* + J_j^*$, and for the reaction/permeation wall

$$\begin{aligned}
&\boldsymbol{N}^*_{CH3OH,z^*=0} = \rho_{cat} m_{cat}(-r_{MSR} - r_{MD})\\
&\boldsymbol{N}^*_{H2O,z^*=0} = \rho_{cat} m_{cat}(-r_{MSR} - r_{WGS})\\
\textit{at } z^*=0 \quad &\boldsymbol{N}^*_{CO2,z^*=0} = \rho_{cat} m_{cat}(r_{MSR} + r_{WGS})\\
&\boldsymbol{N}^*_{H2,z^*=0} = \rho_{cat} m_{cat}(3r_{MSR} + r_{WGS} + 2r_{MD}) - J''_{H2,pern}\\
&\boldsymbol{N}^*_{CO,z^*=0} = \rho_{cat} m_{cat}(-r_{WGS} + r_{MD})
\end{aligned} \tag{5.21}$$

and for the impermeable moving boundary,

$$\text{at } z^*=1, \quad \boldsymbol{N}^*_{i,z^*=1} = c_j U_P \tag{5.22}$$

Boundary conditions for energy conservation Eqs. (5.12 and 5.14) remain almost identical since no derivative terms in space are present:

$$\text{at } z^*=0, \quad \left(\rho c_p\right)_{memb}\delta_{memb}\frac{dT_{memb}}{dt} = -\frac{T_{memb}-T_{z^*=0}}{R_t} - h_{m-s}(T_{memb}-T_{sweep}) \tag{5.23}$$

and

$$\text{at } z^*=1, \quad T_{z^*=1} = T_{wall} \tag{5.24}$$

5.1.6 Numerical discretization

The transient spatially transformed equations, Eqs. (5.19 and 5.20) are discretized using a conservative finite volume method for numerical solution of the problem. Figure 5.3 illustrates the approach and notation used for discretization.

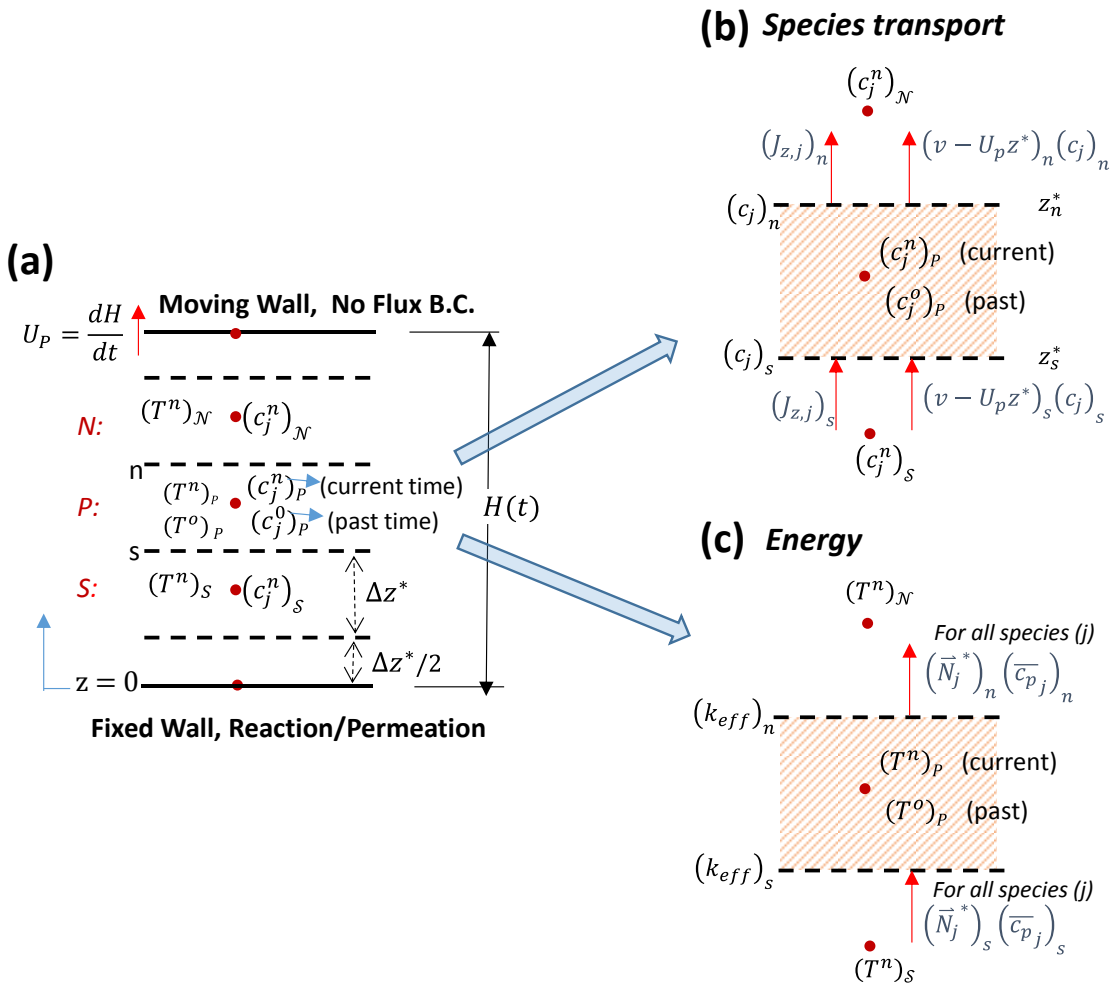

Figure 5.3 Notation for values of dependent variables and fluxes at a representative grid-point cluster for developing the finite difference equations. Three spatial elements are denoted as N, S, and P (North, South, and Point) and two time steps are n and o (current and previous/old time instants, respectively).

An implicit method is used for discretizing the diffusive fluxes based on species concentrations at the next time step to ensure stability of transient calculations, which yields the following finite difference approximation of the species transport equations:

$$\underbrace{\frac{\Delta z^*}{\Delta t}\left(H^n(c_j^n)_P - H^o(c_j^o)_P\right)}_{transient\ change\ in\ species} + \underbrace{\left(c_j^n\right)_n v_n^* - \left(c_j^n\right)_s v_s^*}_{advective\ flux} + \underbrace{\left(J_j^*\right)_n - \left(J_j^*\right)_s}_{diffusive\ flux} = 0 \qquad (5.25)$$

The Maxwell-Stefan diffusive flux in the transformed coordinate system, J_j^* is discretized with the central difference scheme and the flux for all species must be calculated together. (since the diffusive flux of each species is function of concentrations for all other species).

$$\left(\vec{J^*}\right)_n - \left(\vec{J^*}\right)_s =$$

$$-\left\{\frac{1}{H}(c_T)_n([B]^{-1})_n \frac{1}{\Delta z^*}\left(\left(\frac{\vec{c}}{c_T}\right)_N - \left(\frac{\vec{c}}{c_T}\right)_P\right) - \frac{1}{H}(c_T)_s([B]^{-1})_s \frac{1}{\Delta z^*}\left(\left(\frac{\vec{c}}{c_T}\right)_P - \left(\frac{\vec{c}}{c_T}\right)_S\right)\right\} \quad (5.26)$$

and for species *j*, $\left(J_j^*\right)_n - \left(J_j^*\right)_s$ is the j[th] element for the vector $\left(\vec{J^*}\right)_n - \left(\vec{J^*}\right)_s$.

For finding the diffusive flux, all species and the total concentrations are evaluated at the next time step. Similarly, the mole fractions used to evaluate the elements of matrix [*B*] are evaluated using the values at the next time step through iterative procedure.

The advective flux gradient term was approximated using the first order upwind scheme. The upwind scheme treats the value of c_i (or *T)* at an interface to be equal to the value of at the grid point on the upwind side (based on the sign of advection velocity) of the face in order to accurately capture the direction of advective transport of relevant scalars.[89] That is the advective term in Eq. (5.25) is numerically approximated as

$$\left(c_j^n\right)_n v_n^* - \left(c_j^n\right)_s v_s^*$$

$$= \left(\llbracket v_n^*, 0 \rrbracket \left(c_j^n\right)_P - \llbracket -v_n^*, 0 \rrbracket \left(c_j^n\right)_N\right) - \left(-\llbracket -v_s^*, 0 \rrbracket \left(c_j^n\right)_P + \llbracket v_s^*, 0 \rrbracket \left(c_j^n\right)_S\right)$$

(5.27)

where $\llbracket A, B \rrbracket$ denotes the greater of A and B.

(5.25)-(5.27) yields the discretized form of the species conservation equations:

$$\left[H^n\frac{\Delta z^*}{\Delta t}+[\![v_n^*,0]\!]-[\![-v_s^*,0]\!]+\frac{1}{H^n}\frac{(c_T)_n([B]^{-1})_n}{(c_T)_N\,\Delta z^*}+\frac{1}{H^n}\frac{(c_T)_s([B]^{-1})_s}{(c_T)_S\,\Delta z^*}\right]\left(c_j^n\right)_P$$

$$-\left[[\![-v_n^*,0]\!]+\frac{1}{H^n}\frac{(c_T)_n([B]^{-1})_n}{(c_T)_N\Delta z^*}\right]\left(c_j^n\right)_N-\left[[\![v_s^*,0]\!]+\frac{1}{H^n}\frac{(c_T)_s([B]^{-1})_s}{(c_T)_S\Delta z^*}\right]\left(c_j^n\right)_S=\frac{\Delta z^*}{\Delta t}H^o\left(c_j^o\right)_P \tag{5.28}$$

The energy conservation equation, Eq. (5.8), can be similarly discretized with using four terms for changing energy: transient changes, advection, conduction and varying pressure:

$$\underbrace{\frac{\Delta z^*}{\Delta t}\left(H^n\textstyle\sum_j^N\overline{c_{p_\iota}}\left(c_j^n\right)_P T_P^n\;-H^o\sum_j^N\overline{c_{p_\iota}}\left(c_j^o\right)_P T_P^o\;\right)}_{Transient\ Changes\ in\ energy}+$$

$$\underbrace{\textstyle\sum_j^N\left(\vec{N}_j^*\right)_n\;\overline{c_{p_j}}\,T_N^n-\sum_j^N\left(\vec{N}_j^*\right)_s\;\overline{c_{p_j}}\,T_S^n}_{Changes\ due\ to\ advection}+\underbrace{\frac{1}{H}\left(k_{eff,n}\frac{(T_N^n-T_P^n)}{\Delta z^*}-k_{eff,s}\frac{(T_P^n-T_S^n)}{\Delta z^*}\right)}_{Changes\ due\ to\ conduction}=$$

$$\underbrace{\frac{\Delta z^*}{\Delta t}(P^n-P^o)}_{\substack{varying\\pressure}} \tag{5.29}$$

Using the upwind approximation for advective terms in Eq. (5.29), the final discretized form of the energy conservation equation is obtained:

$$\left[H^n\frac{\Delta z^*}{\Delta t}\sum_j^N\left(c_j^n\right)_P\bar{c}_{p_j}+\frac{1}{H^n}\frac{k_{eff,n}+k_{eff,s}}{\Delta z^*}+\sum_j^N\bar{c}_{p_j}[\![\left(\vec{N}_j^*\right)_n,0]\!]-\sum_j^N\bar{c}_{p_j}[\![-\left(\vec{N}_j^*\right)_s,0]\!]\right](T^n)_P$$

$$-\left[\frac{1}{H^n}\frac{k_{eff,n}}{\Delta z^*}+\sum_j^N\bar{c}_{p_j}[\![-\left(\vec{N}_j^*\right)_n,0]\!]\right](T^n)_N-\left[\frac{1}{H^n}\frac{k_{eff,s}}{\Delta z^*}+\sum_j^N\bar{c}_{p_j}[\![\left(\vec{N}_j^*\right)_s,0]\!]\right](T^n)_S$$

$$=H^o\frac{\Delta z^*}{\Delta t}\textstyle\sum_j^N\left(c_j^o\right)_P\bar{c}_{p_j}(T^o)_P+\frac{\Delta z^*}{\Delta t}(P^n-P^o) \tag{5.30}$$

$k_{eff,interface}$ is an effective thermal conductivity at interface. Since the mixture composition in adjacent nodes is different, harmonic means of two *k's* based on linear distribution of nodal temperature is taken for the effective thermal conductivity [90]. $\bar{c}_{p_j}$ is the molar specific heat of species *j* evaluated at a given node temperature. The advective

energy flux gradient term was approximated using an upwind scheme. For each species, direction (sign) of $(N_j^*)_{interface}$ was evaluated to determine which the node (south or north) temperature value should be used in computing the advection term.

Several tests were conducted to validate the code: 1) the numerical solution of equations was shown to be independent of the mesh and time step using a discretization of 100 nodes and time step of 0.005 seconds (error is less than 0.05% in total hydrogen yield after cycle), 2) the total mass of each element (H, C, and O) was monitored to ensure that the calculations did not violate mass conservation (errors for element counts were less than 0.05% during a cycle). 3) total energy (enthalpy) was conserved when integrating all energy inputs/outputs over an entire reactor domain which are generated/consumed due to chemical reactions, applied through heat and work, stored in the reaction chamber, and removed from the reactor via hydrogen permeation.

5.1.7 Solution procedure

Figure 5.4 depicts the methodology which was used to solve the set of coupled governing equations. The reaction rates and H_2 permeation are solved for semi-implicitly by iteratively using the temperature, pressure and concentrations at the current step. These values are found by solving the pressure, total concentration, molar velocity, and total energy/individual species concentration equations sequentially, starting with c_j, T and P from the previous timestep. The updated values for current step c_j, T and P values are then fed back to the iterative loop until they no longer change from cycle to cycle. Once satisfactory convergence is obtained, the simulation moves on to the next time step.

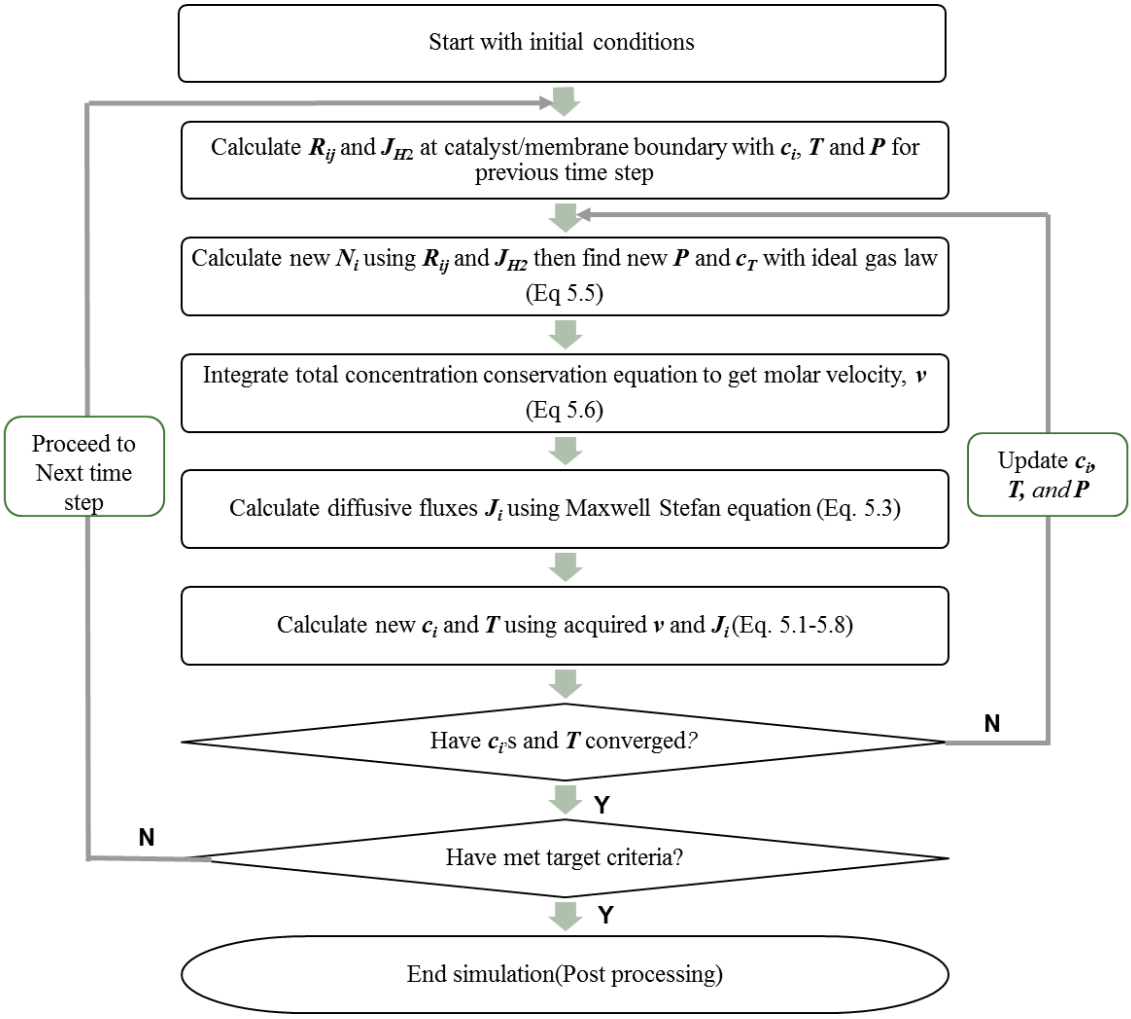

Figure 5.4 Solution procedure for combined transport-permeation-kinetic CHAMP-DDIR model simulations.

5.2 Representative Simulation Results

At the start of a cycle, the injected methanol-water mixture is assumed to immediately evaporate and for all resulting gaseous species to perfectly mix with argon (inert Ar is used for initial purge of the reactor and prior to start of operation). Methanol and steam diffuse to the catalyst surface where they react to produce hydrogen, carbon dioxide, and carbon monoxide. Hydrogen permeates out through the membrane, located at z=0, and when piston moves, the resulting change in volume causes a local, proportional, change in the concentration of each species. The temporal evolution of the species concentrations during representative CHAMP-DDIR cycles, which are obtained from the model simulation, are

depicted in Figures 5.5 and 5.6 for constant volume operation and Figures 5.7 and 5.8 for constant pressure operation (maintained by dynamically adjusting the piston motion), and using the parameters given in Table 5.1, which are based on those of the prototype reactor [91].

Table 5.1 Baseline parameters for reactor model simulations.

Model parameters	**Value [units]**
Initial reactor size, H_{init}	0.020 [m]
Membrane thickness, δ_{memb}	1×10^{-5} [m]
Membrane diffusion coeffient, D_{memb}	1.02×10^{-7} [mol/m-s-bar$^{0.5}$]
Catalyst layer thickness, d_{cat}	1×10^{-3} [m]
Density of catalyst, ρ_{cat}	1300 [kg/m^3]
Sweep gas flow path gap, d_{gap}	1×10^{-3} [m]
Specific surface area of catalyst, S_A	102×10^3 [m^2/kg]
Contact resistance between catalyst and membrane, R_t	2.0×10^{-4} [m^2-K/W]

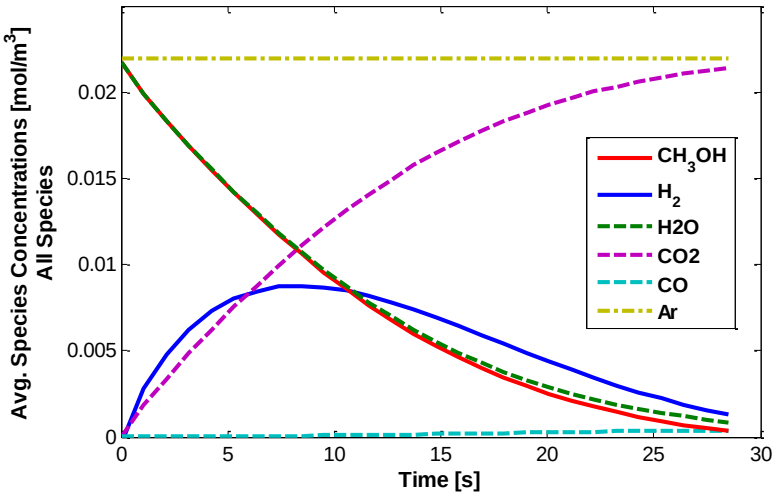

Figure 5.5 Temporal variation of the volume average species concentrations during *constant volume operation.*

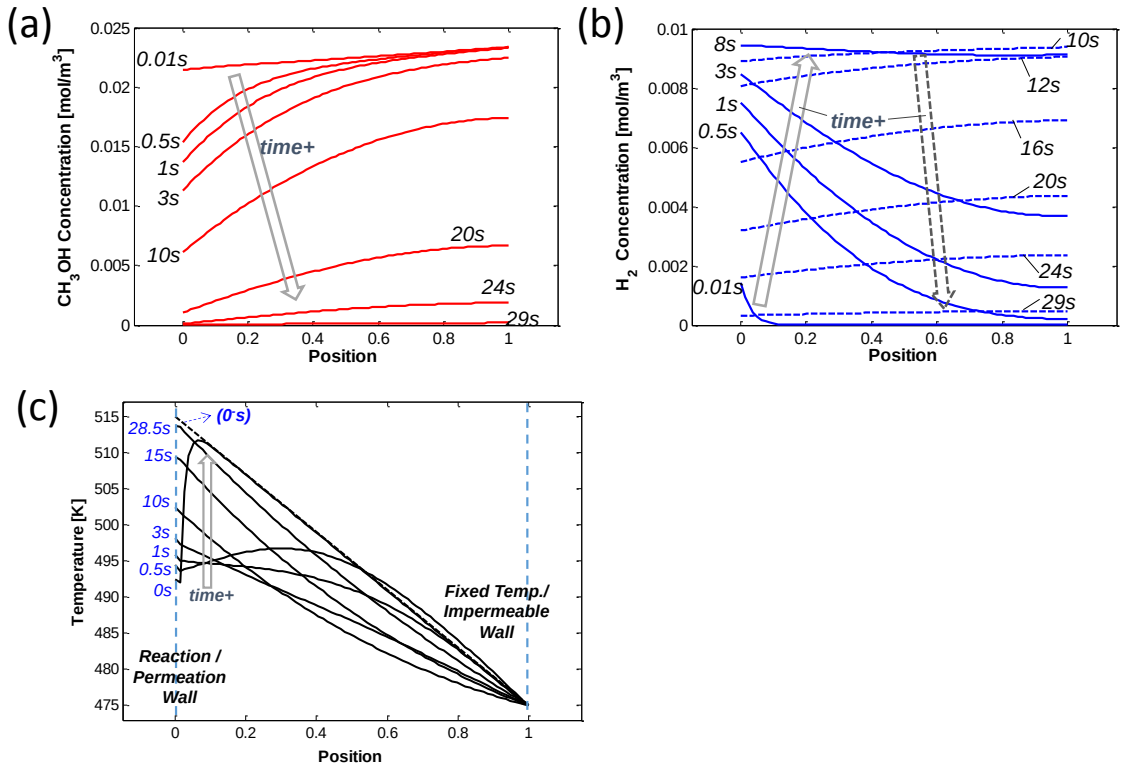

Figure 5.6 Spatial temperature and molar concentration changes during representative simulation. For position in x-axis of plots, 0 is the reaction and permeation wall where catalyst and membrane are collocated, and 1 is the impermeable wall.

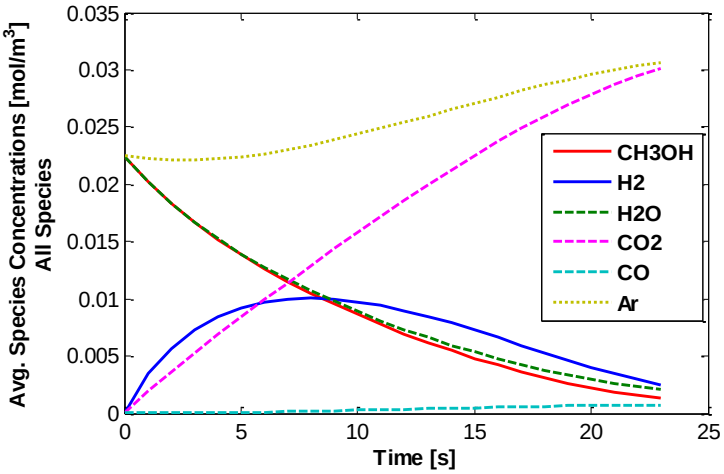

Figure 5.7 Temporal variation of the volume average species concentrations during *constant pressure operation*. The changes in species concentration are caused by reaction and permeation, as well as the reactor volume change required to maintain constant pressure at 300kPa.

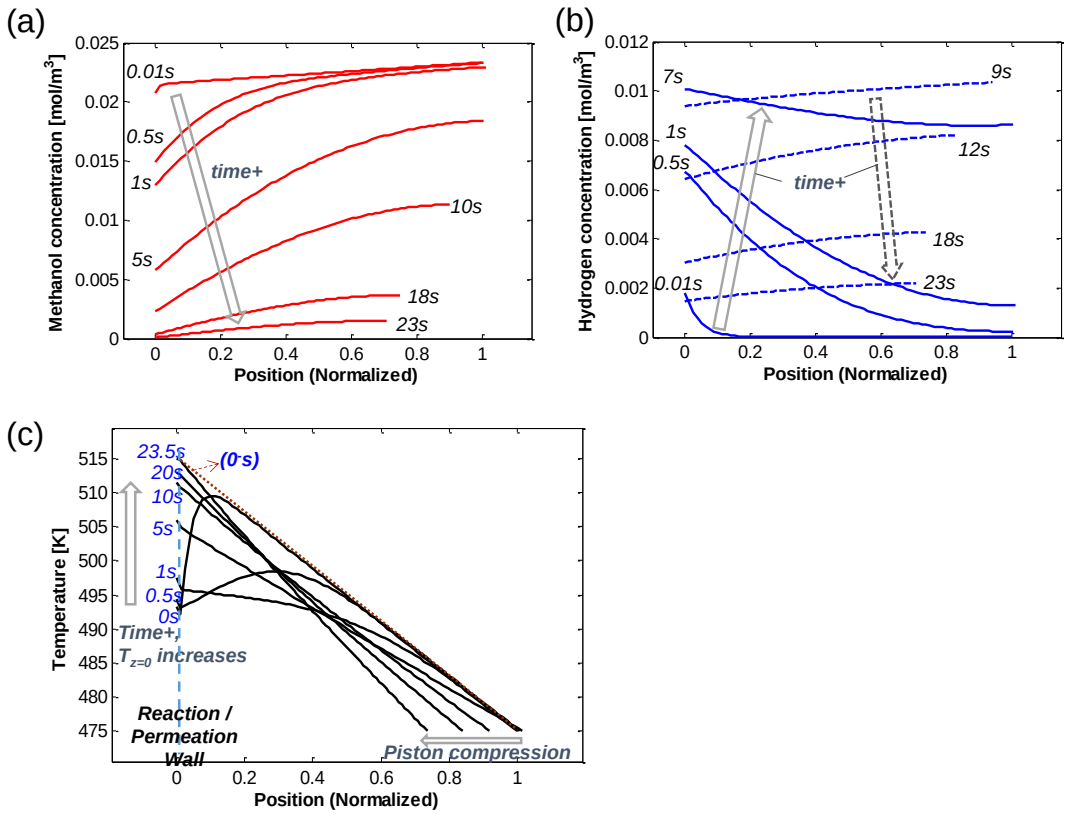

Figure 5.8 Spatial molar concentration of (a) methanol and (b) hydrogen, and (c) temperature changes during representative simulation. For the position in x-axis of plots, their values are normalized by dividing with initial reactor height (the reaction/permeation wall (left end) is always 0 and position of the piston/impermeable wall (right end) varies as height changes.)

Figures 5.5 and 5.7 show volume-average species concentrations within the reaction chamber for all six species (CH_3OH, H_2O, H_2, CO_2, CO, and Ar), resulting from the coupled reaction, transport, and permeation processes. Argon gas, which is used for purging the dead volume of the reaction chamber prior to a cycle, is neither participating in the reactions nor permeating, so its total number of moles does not vary, but, in Figure 5.7 (constant pressure operation), its concentration increases as reactor volume compresses to maintain the pressure at constant. As the reaction cycle proceeds, concentrations of methanol and water (reactants) decrease and carbon dioxide and carbon monoxide (unpermeated products) increases due to the combined effects of the methanol steam reforming, water gas shift, and methanol decomposition reactions described by Eqs. (2.1)-

(2.3), as well as changing reactor volume. The concentration of hydrogen initially rises due to net generation by the reactions, then decreases as its permeation rate exceeds generation rate. The spatial profiles of methanol and hydrogen concentrations, and temperature are depicted in Figures 5.6 and 5.8 for the same representative constant volume and constant pressure simulation cycles respectively. At the beginning of the cycle, the methanol concentration near the catalyst drops rapidly with a corresponding rapid increase in hydrogen at the reaction/separation wall (z=0). At the same time, the produced hydrogen permeates out of the membrane, and also diffuses across the reaction chamber.

Since CHAMP-DDIR's major practical advantages stem from variable volume operation (and realistic CHAMP-DDIR operation will be in the variable volume mode), the rest of discussion will focus on the results for constant pressure operation (Figures 5.7 and 5.8). When hydrogen generation rate is equal to permeation rate (at t~7s in Figure 5.6b), the hydrogen concentration at the membrane reaches its maximum value for the cycle. Hydrogen yield reaches 90% after 23s, while fuel conversion greater than 90% achieved at 17.5s (and 99.5% conversion at 23s). The delay between reaching 90% methanol conversion and 90% hydrogen yield is the result of reduced hydrogen permeation rate as hydrogen partial pressure in the reactor falls (even if total pressure was maintained at constant with compression, the hydrogen partial pressure decrease lead to decreased permeation per Eq. (5.12).

The reaction chamber temperature prior to fuel injection (at $t=0^{--}$, dashed line in Figure 5.8c) was arbitrarily assumed to linearly vary from 515K at *z=0* (heated wall) to 475K at *z=H(t)*. Since instantaneous evaporation of fuel is assumed, the temperature drop due to evaporation of fuel is fully taken into account at the beginning of the cycle for the catalyst/membrane wall as an instant discontinuity imposed at *z=0* boundary. The magnitude of temperature decrease at the fuel evaporation boundary is found by dividing the latent heat of evaporation required to vaporize the injected fuel $\sum_{i=1}^{M,W} N_i u_{fg,i}$ by

effective heat capacity of catalyst $(\rho c_v)_{eff}$. At the beginning of cycle, the catalyst draws heat both from the heated membrane and from the hot gas in the reaction chamber, which increase the catalyst temperature despite the high rates of the net endothermic reaction. As the cycle proceeds, the temperature of the catalyst is driven by the combined effects of the heats of reaction and the heat input (through the membrane) from the high temperature sweep gas at the permeate side, and temperature profile throughout the reactor is determined by the energy conservation equation, Eq. (5.8). Because the rate of the heat input from the sweep gas exceeds what is needed for the endothermic reaction, the catalyst temperature increases continuously. Ultimately a steady state linear profile is reached (if piston becomes stationary), with most of the heat entering from the hot argon sweep gas being lost through the piston.

5.3 Experimental Validation of Model

A prototype CHAMP-DDIR reactor has been previously used to demonstrate the validity of the variable volume batch reactor concept with direct injection of liquid fuel and hydrogen separation with a selective Pd/Ag membrane (Chapter 4). Here we use the results of experimental characterization of the prototype reactor to validate the CHAMP-DDIR model. The previously introduced idealized model (Chapter 3), which ignored the mass/heat transfer effects, could not accurately predict the actual behavior of CHAMP-DDIR when large gradients are present in local species concentrations or temperature. Also, the idealized model lacks the capability to properly predict the effect of changes in arrangement and relative location of heat source, moving wall (piston), and reaction and permeation zones. The comprehensive model developed in this chapter is thus better representation of the realistic conditions able to provide solutions to above cases (where idealized model cannot be used). Once a first principles (non-empirical) model has been experimentally validated, it can be used to investigate reactor performance outside of the

experimentally accessible parameter space. This makes it a highly valuable design tool for reactor optimization.

Figure 5.9 shows comparison of model prediction (in red solid line) and experimental data (in black dashed line) for a single CHAMP-DDIR cycle. The simulated cycle starts with the reaction chamber filled with gaseous fuel and argon mixture (assuming instant evaporation of liquid fuel on injection) at 280 kPa. Pressure increases initially even without compression because MSR and MD reactions, Eqs. (2.1) and (2.2), produce more moles of products than they consume of reactants, but within about 4 seconds it attains its maximum value as the rate of hydrogen permeation begins to exceed the net rate of molar production due to reaction, necessitating piston motion to compress the reactor volume and maintain elevated pressure. Piston motion continues in the simulations until 90% hydrogen yield is reached. In the experiments, piston motion was controlled by linear actuator with a feedback signal from pressure transducer to maintain its pressure at 318 kPa to match the maximum reactor pressure observed during the constant volume experiment with the same initial conditions. The model predictions and experimentally measured reactor pressure, catalyst temperature, hydrogen yield and rate and hydrogen yield efficiencies are plotted together for comparison in Figure 5.9.

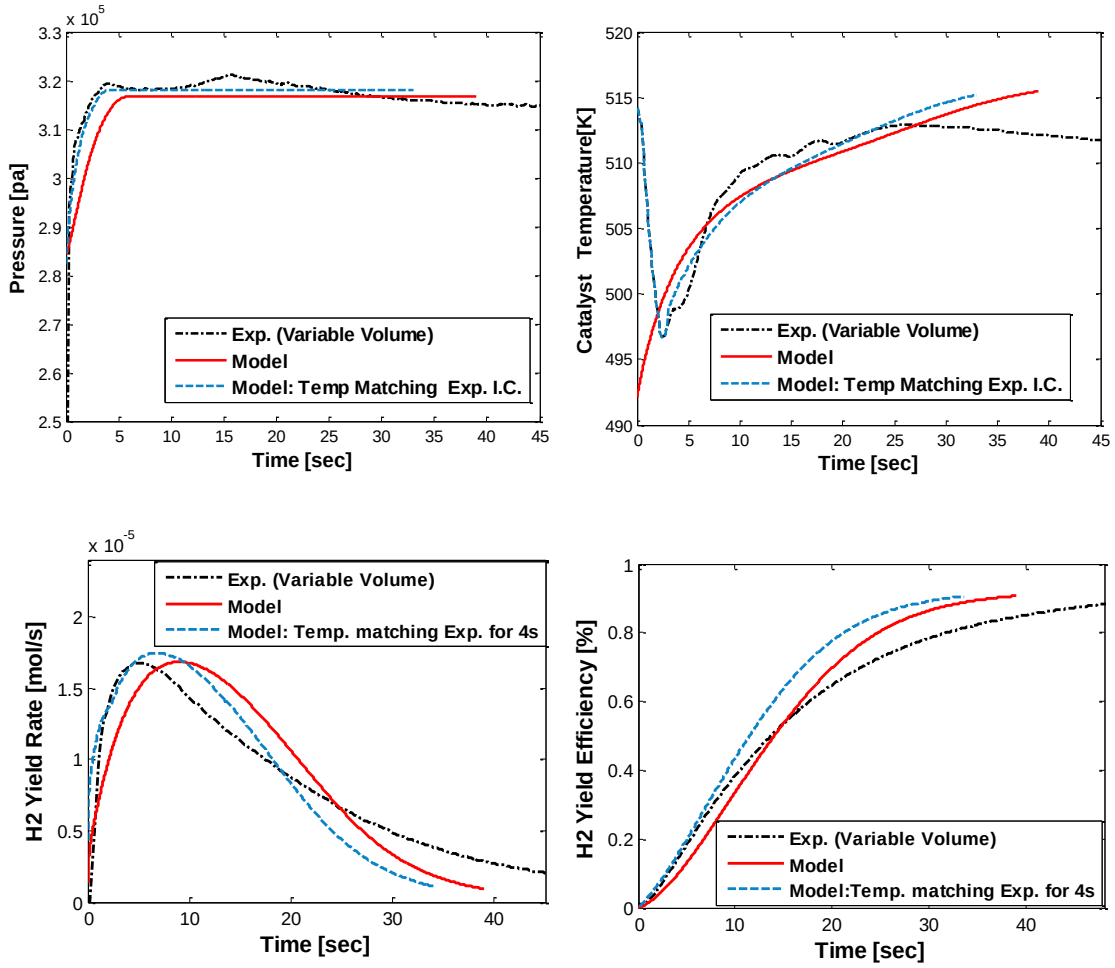

Figure 5.9 Experimental results (black dashed line) and model predictions (red solid line) for transient profiles of (a) reactor pressure, (b) catalyst temperature, (c) hydrogen yield rate, and (d) hydrogen yield efficiency. Model predictions using the temperature profiles observed in experiments for initial 4s are plotted in blue dashed line to assess the impact of misprediction of temperature during early part of the cycle on reactor performance.

Comparing the model prediction and experimentally measured parameters, the trends in baseline hydrogen yield rate and efficiency and catalyst temperature, which were determined by reaction and permeation as well as mass/heat transfer within the reaction chamber, are as expected (thus, validating the present understanding of the key operating principles of the reactor.)

In addition to correctly predicting qualitative behavior, of equal interest is the ability of the reactor model to predict the performance of the real reactor quantitatively. Comparing the

hydrogen yield rates between experiments and simulation results, two major differences are observed. The hydrogen generation rate predicted by model is 1) lower at the start of cycle, and 2) higher at the later stage of cycle compared to that from the experimental data. One of the potential causes for slower hydrogen production at the beginning is a discrepancy in the predicted transient temperature evolution, in particular in the predicted catalyst temperature. The assumption of instant evaporation of liquid fuel with all energy of vaporization supplied by the catalyst results in a prediction that the catalyst temperature begins at the lowest temperature observed through the entire cycle, 492 K. On the other hand, the experimentally observed catalyst temperature displays a non-instantaneous and slightly smaller temperature drop, with the minimum temperature occurring at ~ 4 s, and the temperature decreasing only to 497 K. During the first four seconds, there is about a 10 K difference between the model predicted and experimentally observed catalyst temperature, with the model results being the lower of the two. This temperature difference would result in about a 30% decrease in predicted methanol steam reforming rate due to exponential dependence of reaction rates on temperature, and is the primary source of the lower hydrogen generation rate observed in the model predictions at early times as compared to the experiment. This is demonstrated by performing a simulation in which the catalyst temperature is imposed (not computed) during the first 4 seconds of the simulation using the experimentally observed values. The resulting predictions are depicted using blue dashed lines in Figure 5.9, and it is clear that the higher initial catalyst temperatures result in a predicted hydrogen yield rates much more quantitatively consistent with the observed rates.

After the initial rise in hydrogen yield rate, the subsequent experimentally observed drop in hydrogen yield rate is faster than the model predicts, and hydrogen production continues for a longer period of time as a result. It is believed that the discrepancy in predicted and observed hydrogen yield rate is rooted in the treatment of hydrogen permeation. The membrane permeance model used in the simulations was obtained using steady-state

measurements[69], and thus is only valid if competitive adsorption is very fast and all species attain equilibrium coverage on the membrane. Accounting for the dynamic impact of competitive membrane coverage by non-hydrogen species via an adsorption/desorption kinetics model would provide for more accurate treatment. Unfortunately, no such description or experimental data have been reported in the literature, so we used the equilibrium coverage values that are available (Appendix B). Another source of error in the model may be the simplified treatment of the removal of permeated hydrogen on the backside of membrane by sweep gas. As shown in Figure 5.10, the sweep gas enters at the outer diameter of the cylindrical gap between membrane and permeation block, swirls along the periphery, and exits with hydrogen through the center and the complex flow and variation in local mass transfer performance may be inadequately represented using a constant mass transfer coefficient in the current 1-D model. As a result, the spatially average permeated side hydrogen partial pressure, i.e., $P"_{perm,H2}$ in Eq. (5.12), might be higher in the experimental reactor than predicted, leading to slower actual permeation rates. The suggestions for improving models to match with experimental results are discussed in chapter 6 for future work.

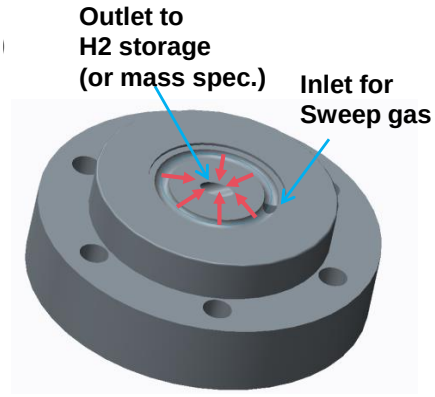

Figure 5.10 Permeation block showing the swirl/sweep geometries. The sweep gas enters through inlet at the outer diameter of the cylindrical gap between membrane and permeation block, swirls along the periphery, and exits with hydrogen through outlet at the center.

5.4 Characteristic Timescales and Rate Limiting Steps

In order to establish a design methodology for this new class of reactors, it is important to first understand the underlying processes determining reactor performance. These processes include (liquid) fuel evaporation, reaction, transport, and permeation, which are all coupled in the transient operation of CHAMP-DDIR. Each of these processes is associated with its own timescale which is defined as the time required for the system to reach a new steady-state if the source of disturbance is a process of interest, while other processes are assumed to remain unchanged/frozen at their predefined state.

5.4.1 Reaction timescale

The rate of consumption of methanol roughly follows an exponential decay, $\exp\left[-t/\tau_{Rxn}\right]$, where τ_{Rxn} is the reaction characteristic time constant. (When $t=\tau_{Rxn}$ the methanol conversion is approximately $1-1/e$. $1/e$ is known as *e-folding time*.) Therefore the characteristic time scale for the reaction, τ_{Rxn}, will be defined as the time required for methanol conversion to reach 63.2% or $1-1/e$. To calculate τ_{Rxn}, it is assumed that diffusion and permeation are much faster than the reaction, i.e. $\tau_{Perm}, \tau_{Diff} << \tau_{Rxn}$. Thus, the partial pressures (species concentrations) of all species in the reactor are uniform and for hydrogen, retentate side partial pressure, $p_{H2,ret}$ always equals to the permeate side pressure, $p_{H2,perm}$.

5.4.2 Permeation timescale

The rate of removal of hydrogen by permeation through the membrane can also be assumed to follow an exponential decay, $\exp\left[-t/\tau_{Perm}\right]$, where τ_{Perm} is the permeation characteristic time constant. Similarly to reaction time scale, when t= τ_{Perm}, the hydrogen yield efficiency is 63.2% of its maximum achievable hydrogen yield. The τ_{Perm} is found by assuming

permeation timescale is much slower compared to reaction (MSR), thus the membrane is immediately exposed to an equilibrium mixture of 3:1 hydrogen to carbon dioxide. Therefore the characteristic time scale for permeation, τ_{Perm}, is defined as the time required for the hydrogen yield to reach 63% of the maximum possible hydrogen yield, when the reactor is initially filled with a 3:1 H_2:CO_2 mixture at $P_{initial}$. The calculation also considers the reduction of permeance (as expressed by permeation reduction factor, θ in Eq 3.7) as due to competitive adsorption of CH_3OH, H_2O, CO_2, and CO on the membrane surface.

5.4.3 Diffusion timescale

The diffusion timescale for bulk gas is defined as $\tau_{diff} = H^2 / D_{m,avg}$, where H is the size of the reactor, and $D_{m,avg}$ is the average of multi-component mass diffusion coefficients($D_{i,m}$'s) found via the semi-empirical equation of Gillilland [74]. Since the diffusion coefficient of a species *i* through the mixture, $D_{i,m}$ varies with composition, as well as molar flux of each component, Eq. 5.31 was used to find an approximate value for the $D_{i,m}$. Assuming that species A, for example, is diffusing through a stagnant mixture of A, B, C, D, and E,

$$D_{A,m} = \frac{1-x_A}{x_B/D_{AB}+x_C/D_{AC}+x_D/D_{AD}+x_E/D_{AE}} \tag{5.31}$$

For characterization of the diffusion timescale during the reaction cycle, x_i's are the representative mixture composition in the reactor corresponding to 50% methanol conversion.

5.4.4 Fuel droplet evaporation timescale

From study of Varady and Fedorov [16, 17, 56], the fuel droplet evaporation in DDIR can occur in two modes: (1) in-transit during the fuel droplets traveling from the fuel injector to the catalyst layer and (2) on the catalyst surface after forming a thin liquid fuel layer. For mode (1) the droplet evaporation time scale is given by $\tau_{evap,drop} = \frac{R_{drop}^2}{K}$, where R_{drop} is an initial radius of a droplet, and K is the evaporation constant [70]. The details of

K is discussed in the previous section 3.2.3. For film-based evaporation, mode (2), evaporative time scale is defined by $\tau_{evap,film} = \frac{\rho_l h_{film}^2 h_{fg}}{k_g(T_\infty - T_S)}$ where h_{film} is the film thickness and T_S is saturation temperature. [72]

5.4.5 Rate limiting process from timescale analysis

The timescales of all four processes (reaction, diffusion, permeation, and evaporation) are calculated for representative CHAMP-DDIR's operating conditions used in experiments. Figure 5.11 illustrates the variation of these timescales for temperature ranging 473 to 553K. For reaction timescales, which plotted in solid lines, two catalyst loadings (proportional to thickness of catalyst layer) with d_{cat}=0.25mm and 1mm were used for comparison. Among all processes, reaction timescale has the most significant dependence on temperature (its slope is highest for varying temperature). For hydrogen permeation timescale, the thickness of membrane was varied 10μm and 25μm and plotted in dash lines. The size of the reaction chamber, H, was taken to be 10mm and 20mm for diffusion timescale characterization, and the results are are plotted as dotted lines. Lastly, the evaporation timescale is computed by treating the entire amount of injected fuel is vaporized from a thin layer (this is expected based on the original DDIR study by Varady [16, 17]). For the operating ranges in plot, timescale for evaporation is the fastest and other three processes are all in the similar order, which is 2 order slower than evaporation timescale. Therefore, the evaporation of liquid fuel can be assumed to occur instantaneously on the time scale of typical CHAMP-DDIR experimental cycle.

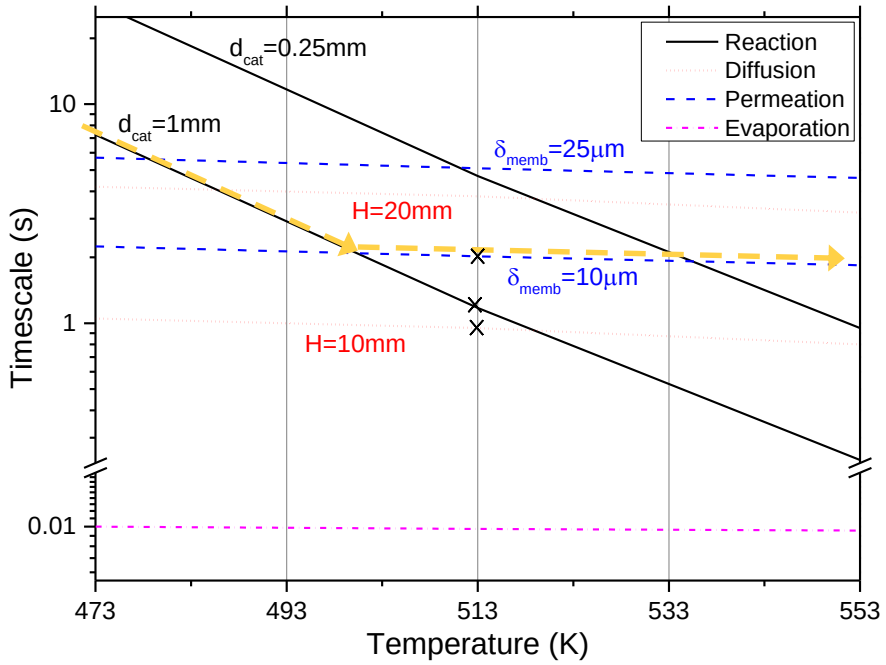

Figure 5.11 Timescales for reaction (solid lines), permeation (long dash line), diffusion (short dash line), and evaporation (mixed dot-dash line) versus temperature between 473K and 553K.

The thick dashed line with arrow in the Figure 5.11 shows the transition of rate limiting processes while temperature varying from 473K to 553K and $H=10mm$, $\delta_{memb}=10\mu m$, and $d_{cat}=1mm$. Following the arrow line, when temperature reaches 500K, the reactor performance is changed from a condition of reaction kinetics limited to a condition of hydrogen permeation limited performance. A typical operating point ($T=513K$, $H=10mm$, $\delta_{memb}=10\mu m$, and $d_{cat}=1mm$) used in experiments is marked by **x** on the set of curves. For this condition, the diffusion timescale is 1.0 second, the reaction timescale is 1.25 seconds, and the permeation timescale is 1.95 seconds. The timescale for operation of a cycle then is dictated by permeation, which is the longest. However, all the timescales are fairly well matched implying that no one process is exclusively rate limiting. For example, even though diffusion has the shortest characteristic time, it is by no means negligible.

5.5 Theoretical Analysis Using Comprehensive Model

Using the experimentally validated model, a comprehensive theoretical assessment of CHAMP-DDIR's behavior has been performed. The main purpose of the analysis is to determine the extent to which heat and mass transfer within the reactor affect reactor performance, especially focusing on volumetric power density.

5.5.1 Effect of mass transfer limitations

One of the goals for development of the comprehensive CHAMP-DDIR model is to determine when, if ever, a simple Fickian description of mass transfer is adequate, and also to determine under which conditions mass transfer limitations play no significant role. These questions have been addressed by comparing the results of three simulation cases: (1) the reactor constituents are perfectly mixed and no internal mass transfer limitations exists (corresponding to an assumption of infinite diffusion coefficients), (2) mass transport is described using an effective binary diffusion coefficient for each species and Fickian description[19], and (3) diffusion is described using the Maxwell-Stefan formalism, i.e., Eq. (5). Figure 5.12 compiles the results of these simulations in a manner that highlights the key findings.

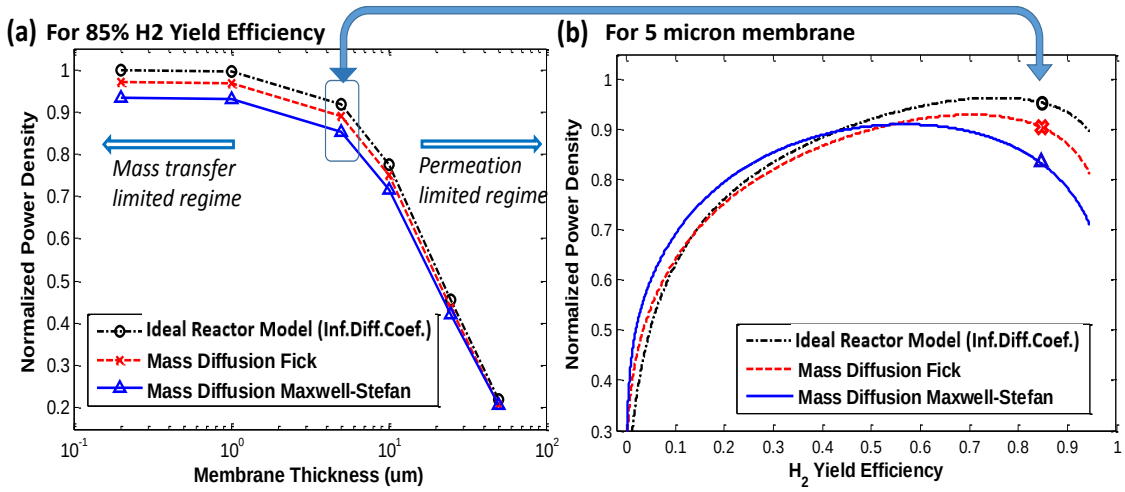

Figure 5.12 Effect of mass transfer on volumetric power density. (a) Normalized power density for 85% hydrogen yield efficiency with varying membrane thickness from 0.5 to 5 micrometers and (b) Normalized power density trajectories vs hydrogen yield efficiency as it evolves during a cycle with 5 micrometer thick membrane. The normalization was done against the maximum power density computed for the plotted range, which was at 0.5 μm membrane with ideal reactor model. All simulations are for the fixed volume reactor with no piston motion during the reaction cycle.

Figure 5.12 depicts the volumetric power density predictions over wide range of membrane thicknesses (0.5 ~ 50 μm), at 85% hydrogen yield efficiency during the constant volume operation (reactor chamber height = 1 cm) for the three different mass transfer models. By decreasing the membrane thickness, the reactor performance is changed from a condition of permeation limited, in which the internal mass transfer model has little to no effect, to a condition of internal bulk mass transfer limited performance. The results in Figure 5.12a indicate that in all cases where bulk mass transfer plays a role, the predictions of the multi-component Maxwell-Stefan formulation differ from those of the simple Fickian diffusion formulation by about 5%. Furthermore, the multi-component Maxwell-Stefan formulation predicts a greater impact of bulk species transport limitation, and thus implies a transition from the permeation limited regime at a greater membrane thickness than the Fickian model indicates. Therefore, a simple Fickian diffusion model may lead to inaccuracies in design and optimal sizing of the reactor components.

In Figure 5.12b, power densities for simulation with a 5 μm thick membrane are plotted as a function of instantaneous hydrogen yield efficiency as the reactor proceeds through the operation cycle. The existence of a tradeoff between power density and hydrogen yield efficiency, such that maximizes power density requires loss of hydrogen yield efficiency, has been previously reported [19]. The results in Figure 5.12b indicate that this tradeoff is accentuated when the more accurate Maxwell-Stefan model is used. An interesting result apparent in Figure 5.12b is that the Maxwell-Stefan model, which results in greater mass transfer resistance for species transport, predicts higher power density at low hydrogen yield efficiencies than either of the two less accurate models. This result is due to the increased resistance to mass transfer within the reactor preventing hydrogen that is being produced from diffusing away from the membrane early in the cycle, leading to higher partial pressures of hydrogen driving increased permeation. Later in the cycle, the impact of higher mass transfer resistances on the rate of fuel supply to the catalyst begin to dominate leading to a decrease in hydrogen production, and towards the end of cycle, hydrogen that has spread throughout the reactor diffuses back to the membrane more slowly when mass transfer resistances are greater.

The results depicted in Figure 5.12 are predictions made when simulating fixed reactor volume operation in order to independently assess the effect of the mass transfer models. An impact of mass transfer depends on the relative importance of internal (bulk) species transport resistances to the membrane resistance to hydrogen permeation and the external mass transfer resistance for permeated hydrogen removal by the sweep gas. The internal resistance to species diffusion in the gas phase is altered discretely by changing the initial reactor chamber height for constant (but different) volume operation, and also changes continuously during variable volume operation.

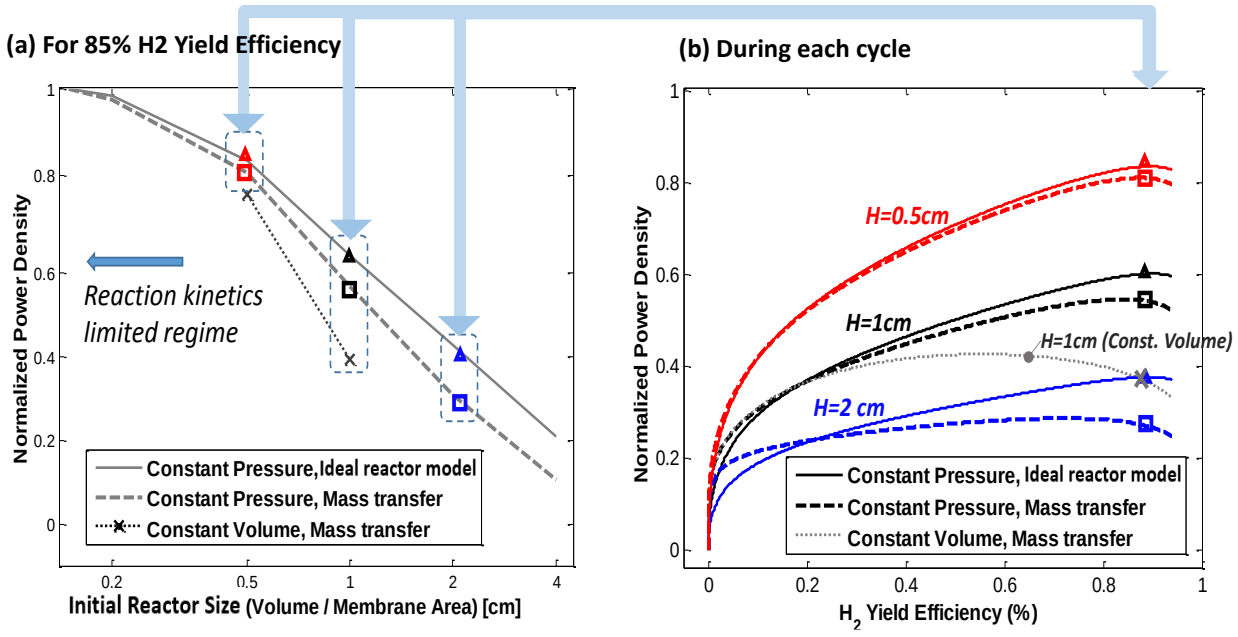

Figure 5.13 Effect of internal (bulk) mass transfer on volumetric power density with constant pressure and constant volume operations while varying (a) reactor size (initial height) at 85% yield and (b) hydrogen yield efficiency during various cycles. The normalization was done by the maximum power density computed for the plotted range, which was at 0.1cm initial reactor height with ideal reactor model.

To demonstrate these effects, Figure 5.13 depicts results of simulations with constant volume operation, and also simulations in which volume was varied to maintain a constant pressure. Figure 5.13 depicts predicted volumetric power density at 85% hydrogen yield efficiency using (1) the Maxwell-Stefan formulation for constant volume operation, (2) for operation with varying volume to maintain constant pressure, and (3) for a perfectly mixed reactor without internal (bulk) mass transfer and with varying volume to maintain constant pressure. For these three conditions, the power density at 85% hydrogen yield efficiency has been predicted for different reactor heights (initial reactor height for the varying volume simulations) ranging from 0.2 cm to 4 cm, and with all other parameters kept the same (Table 5.1). The constant pressure operation simulations are performed using a reactor pressure of 350 kPa. In all cases, the volumetric power density is highest for the smallest reactor size, and decreases with increasing reactor height primarily due to loss of effective membrane area for permeation per unit volume of the reactor. As shown above,

the inclusion of internal (bulk) mass transfer resistance reduces power density at a fixed (high) hydrogen yield efficiency, and, as expected, this effect becomes more pronounced as reactor height increases. For the same physical reason, an additional benefit of varying volume operation is revealed by this analysis, namely, that reducing the reactor height not only maintains elevated pressure to drive higher permeation rates, but it also reduces internal mass transfer resistance. The impact of the latter effect is greater when there is a higher initial reactor size.

In Figure 5.13b, power densities are plotted as a function of hydrogen yield efficiency during the cycle for different initial reactor heights, for constant volume and constant pressure operation, and with and without inclusion of internal mass transfer resistances. Figure 5.13b depicts volumetric power density while varying hydrogen yield efficiency for the constant pressure mode of operation for three initial reactor heights (0.5cm, 1cm, and 2cm) and compares these to the constant volume cycle for the reactor with fixed 1cm height. An important insight from this plot is that with varying volume to maintain constant reactor pressure, which is higher than the cycle-averaged value for the constant volume mode, the tradeoff observed for constant volume operation (Figure 5.12b), wherein high hydrogen yield efficiency comes at the cost of sub-optimal power density, is nearly eliminated. When the reactor volume is compressed to increase pressure the permeation is enhanced, and the cycle time required to achieve a prescribed hydrogen yield is reduced. As a result, the time delay between hydrogen production and permeation is also reduced. In order words, the trajectory of reactor volume, which changes from highest at the beginning to smallest at the end of cycle, accentuates the benefits of variable volume operation, since volume compression (to keep elevated pressure) occurs in sync with the time when less transport resistance is desired. This aspect is a unique fundamental advantage of a CHAMP-class reactors, which is very attractive feature especially for portable applications

For a larger reactor, in which internal mass transfer resistance becomes important, the benefit of increased pressure on permeation is slightly mitigated by increased internal mass transfer resistance, as diffusion coefficient is inversely proportional to pressure [92]. Figure 5.13 portrays again the results that due to the increased mass transfer resistance within a large reactor, the differences between the predictions using the Maxwell-Stefan model and those obtained with the ideal model are accentuated.

5.5.2 Effect of heat transfer in the reactor chamber

Temperature affects the reactor performance primarily through (i) the temperature dependence of rates of chemical reactions, (ii) the temperature dependence of membrane permeability, and (iii) the effect of temperature on pressure in the reactor. The first two factors depend on the local temperatures of the catalyst and membrane, respectively, and the latter depends upon an average gas temperature in reaction chamber (Figure 5.14) rather than details of the temperature distribution. Operating CHAMP-DDIR with higher temperature at the catalyst/membrane layer is favorable for enhancing the endothermic MSR reaction, and for increasing hydrogen permeation at the membrane, whose permeability has an Arrhenius-type temperature dependence, and also promotes rapid evaporation of the liquid fuel. In addition, a higher average temperature in the reaction chamber leads to increased pressure, which enhances the driving force for hydrogen permeation through the membrane. On the other hand, the energy penalty for maintaining the reactor temperature, which negatively impacts power density, increases with temperature [19]. Clearly, a useful reactor model must properly account for all relevant thermal effects. A major purpose of the thermal analysis performed on the CHAMP-DDIR reactor is determination of the impact of different assumptions on the performance predictions, to guide result interpretation and to enable a physically sound description of key phenomena governing performance, without unnecessary and perhaps misleading excessive detail.

In order to assess the impact of the thermal model on performance predictions, simulations were run with three approaches to dynamic temperature profile determination in the reactor, and the results are depicted in Figure 5.14a. Predictions obtained using the comprehensive thermal energy model described by Eqs.(5.7)-(5.8) are presented along with simulation results in which a linear temperature profile is imposed (the steady state temperature case). These are compared to an ideal (infinite thermal diffusivity) case, analogous to the perfectly mixed reactor model for mass transfer, in which the temperature is spatially uniform but varying in time to impose energy conservation. The temperature distributions obtained through simulations solving the discretized energy conservation equation, are plotted in Figure 5.14(b), along with the imposed temperature distributions for the other two cases. Power density calculation (Eq. (2.1)) requires an energy input, which is the time integral of heat input to the reactor plus the network to compress the reactor volume. For the power density comparison shown in Figure 5.14(a), the energy inputs, E_{in}, needed for Eq. (2.1), are found differently for each model: i) the steady-state, linear temperature profile model calculates energy input using an overall energy balance, i.e., the external heat input is the required heat for fuel vaporization and heating plus the total heat of reactions, ii) the lumped, uniform temperature model assumes a constant heat input rate (total required heat input for evaporation and reactions divided by cycle time), and iii) the fully discretized model finds the heat input by integrating the derived boundary heat flux at the reactor bottom. For all three models the work input is found by integrating the boundary work numerically.

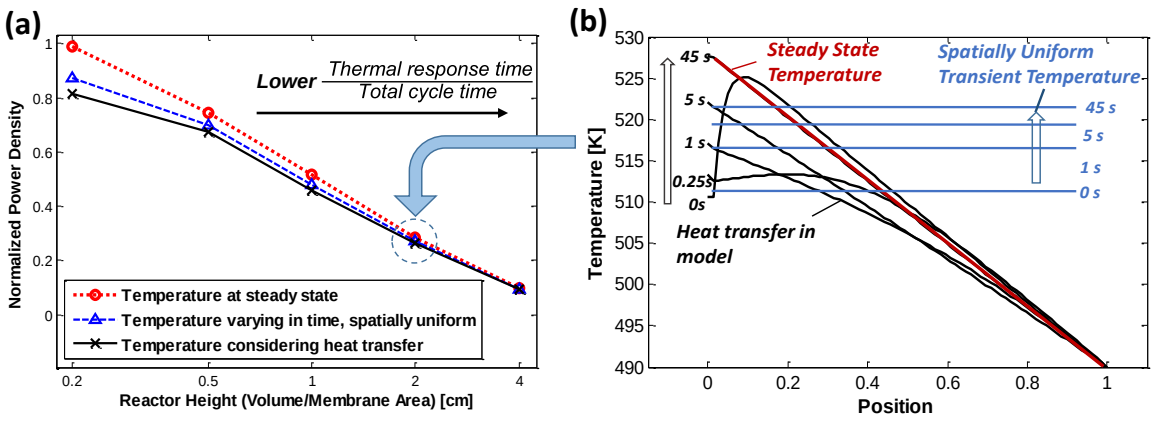

Figure 5.14 Comparison of different approaches to incorporate thermal effects in the CHAMP-DDIR model. Effects of heat transfer on volumetric power density is evaluated by applying three different temperature conditions for constant volume operation mode with a varying reactor size (height). (a) Normalized power density for three model while varying reactor height and (b) time evolution of temperature in a 2cm reactor using the thermal model prediction and two approximations for spatial temperature distribution (linear and uniform) (x-axis shows normalized position between the catalyst =0 and piston =1 boundaries).

The results assuming time-independent (instant steady-state) linear temperature profile predict higher power densities primarily because this model maintains a higher temperature at the catalyst/membrane wall and therefore imposes higher reaction and hydrogen permeation rates, as seen in Figure 5.14(b). When comparing the power densities for the two thermally transient cases, the assumption of spatially uniform (but time varying) temperature results in a slightly higher value compared to the predictions using a model based on the energy equation. This is because of the higher average temperature in the reactor when temperature is assumed to be spatial uniform, as seen in Figure 5.14(b), which leads to higher pressure in the reaction chamber and thus a higher driving force for hydrogen permeation during the cycle.

The comparison of model performance predictions shown in Figure 5.14(a) indicates that predicted volumetric power density has significant dependence on the both the spatial and temporal variations of temperature for lower reactor height (or higher specific membrane area per unit reactor volume), but as reactor height increases the temperature dependence

diminishes. This effect is dictated by relative magnitude of the thermal response time scale of the catalyst/membrane as compared to the total cycle time. The membrane/catalyst thermal transient is largely independent of reactor size because the heat is supplied from outside the reactor through the membrane directly into the catalyst, while the cycle time is affected by the mass transfer resistances which increase with reactor height. Thus, for larger reactors whose behavior is dominated by bulk species transport the impact of thermal dynamics becomes largely insignificant as long as the elevated temperature required for fast reaction kinetics and permeation is maintained at the catalyst and membrane surfaces. As a result, performance predictions using different models become very similar for larger reactors.

An additional insight regarding the role of temperature in predicted reactor performance as revealed by Figure 5.14 is that the impact of differences bulk gas thermal behavior becomes less, rather than more, important, as the internal (bulk) thermal resistance is increased, i.e., with increased reactor height. This trend is somewhat counterintuitive and is opposite to that seen when considering the effects of mass transfer. The reason for this different behavior is again due to the fact that heat transfer within the reactor plays little role in dictating reactor performance. Rather, the impact is dominated by the local catalyst and membrane temperatures, and otherwise gas phase temperature within the reactor only impacts reactor pressure in an average sense, as seen in Eq. (5.5).

5.6 Conclusions

A comprehensive reaction-transport-permeation model for simulation of methanol steam reforming for hydrogen generation in variable volume membrane batch reactor with direct liquid fuel injection (CHAMP-DDIR) was developed. The model is validated against experimental results through comparison of predicted and measured hydrogen production rate, reactor pressure, and temperature. The experimentally validated model is then used to

assess the mass and heat transfer effects (separately) by comparing predictions from models with increasing levels of complexity (in modeling of transport phenomena), as well as to identify the relationships between CHAMP-DDIR design and operating parameters and the rate-limiting processes that govern reactor performance in terms of power density and hydrogen yield efficiency.

The specific conclusions of the theoretical analysis include:

- Inclusion of the mass transfer effects to the model is important when predicting a performance of CHAMP-DDIR operating in the bulk mass transfer limited regime (e.g. with thinner membrane, higher specific membrane area, and higher catalyst loading).
- The reactor performance is changed from a condition of permeation limited to internal mass diffusion limited by decreasing the membrane thickness.
- The multi-component Maxwell-Stefan formulation predicts a greater impact of internal mass transfer limitation, and thus implies a transition from the permeation limited regime at a greater membrane thickness than the Fickian model indicates.
- With CHAMP-DDIR's variable volume operation, reducing the reactor height not only maintains elevated pressure to promote higher permeation rates, but it also reduces internal mass transfer resistance which plays a significant role. In addition, the trajectory of reactor volume, which changes from highest at the beginning to smallest at the end of cycle, accentuates the benefits of variable volume operation, since volume compression (to keep elevated pressure) occurs in sync with the time when less transport resistance is desired. This aspect is a unique fundamental advantage of a CHAMP-class reactors.
- The impact of differences in the details of the thermal model becomes less important, as the internal thermal resistance is increased (with increased reactor height), a trend that is opposite to that seen when considering the effects of mass

transfer models. The reason for this different behavior is that heat transfer within the reactor affects performance only in an integral sense through impact on the reactor pressure, which is minor as compared to the effect of the local catalyst and membrane temperatures that directly govern the rate of reactions and hydrogen permeation.

CHAPTER 6

CONCLUSIONS AND RECOMMENDATIONS FOR FUTURE WORK

A direct liquid fuel injection/variable volume reactor integrated with a hydrogen selective membrane (CHAMP-DDIR) described in this thesis is a promising new concept for hydrogen production in portable and distributed applications. The CHAMP-DDIR reactor performance has been first analyzed using simplified transport models with which conditions for maximum performance, e.g. highest volumetric power density, were identified. Supporting the theoretical analysis, experimental characterization of a working bench-scale test reactor was performed. A prototype laboratory-scale reactor demonstrated the ability to realize performance improvement, while also indicating a need for more a rigorous model for accurate exploration of the design and operation space. Consequently, a comprehensive reactor model which carefully considers the effects of heat and mass transfer, including rigorous treatment of multi-component species transport was developed. The model was validated against experimental results through comparison of predicted and measured reactor operational parameters. This experimentally validated model was used to identify the relationship between CHAMP-DDIR's design/operating parameters and the rate-limiting processes that govern reactor output (among fuel evaporation, catalytic reactions, heat/mass transport, and hydrogen permeation.)

Both theoretical and experimental analyses reveal that significant practical improvement in the volumetric power density can be achieved primarily as a result of two unique factors enabled by CHAMP-DDIR: 1) time-modulated fuel injections enables higher reaction/permeation rates by preventing the large temperature drop that accompanies a single batch liquid fuel injection, as well as allowing for reduction in a required reactor volume (by carefully matching the rates of fuel addition and product

removal due to hydrogen permeation), and 2) volume modulation during a batch cycle to control reactor total pressure, thus providing enhanced driving force for the permeation process and maintaining the hydrogen throughput of the reactor at an increased level.

This thesis work has led to a number of fundamental insights and important recommendations about the design and operation of CHAMP-DDIRs for methanol steam reforming. The original contributions to the field of portable fuel reforming and catalytic microreactor design are summarized below along with a summary of the important conclusions from the theoretical and experimental studies and suggestions for future studies on CHAMP-DDIR class reactors.

6.1 Original Contributions

6.1.1 Fundamental science

- Development of CHAMP-DDIR concept, which combines the variable volume operation of CHAMP (CO_2/H_2 Active Membrane Piston) with direct injection of liquid fuel of DDIR (Direct Droplet Impingement Reactor), synergistically exploits a diverse set of reaction engineering principles, resulting in an novel approach to portable/mobile fuel reforming aiming to achieve the maximum volumetric power density as well as on-demand dynamic variation in hydrogen throughput without sacrificing fuel conversion efficiency.
- CHAMP-DDIR utilizes the concept of multifunctional reactors in which 1) the dynamically controlled fuel injector acts as both a precise liquid feed pump and fuel atomizer, 2) heated porous catalyst/separation membrane layer acts as the liquid vaporizer as well as reaction/permeation zone, 3) variable volume of the reactor chamber plays important roles in controlling thermodynamic conditions during reaction cycle, and 4) hydrogen selective membrane removes hydrogen in situ during the operation cycle so that reaction rates can be enhanced by shifting the reaction

equilibrium in a favorable direction via removing reaction product while providing pure hydrogen stream (ideally to be utilized by a fuel cell).

- A physics-based comprehensive model of CHAMP-DDIR is developed, which considers the coupled process of 1) dynamic introduction of fuel, 2) liquid fuel evaporation, 3) catalytic reaction, 4) hydrogen permeation at membrane, and 5) heat transfer and multicomponent species transport in the gas phase. This provides a comprehensive framework to investigate the influence of operating parameters on reactor performance. In this thesis, the model is applied to methanol steam reforming process, but the developed simulation tools and methodology can be extended to other type of fuels or reaction pathways/systems.
- A laboratory-scale CHAMP-DDIR prototype was developed, consisting of a variable volume piston-cylinder reactor chamber, an actively-controlled fuel (atomizing) injector, hydrogen selective membrane and catalyst to steam reform methanol. The experimental apparatus allows for demonstration of two distinct modes of CHAMP-DDIR operation, pulse-modulated fuel injection and batch reaction with dynamically-adjusted reactor volume. The benefits of the CHAMP-DDIR concept were successfully demonstrated through many different fuel injection and pressure modulation conditions and their impact on performance were quantified. More importantly, the experimental apparatus played an essential role in development and validation of theoretical models of CHAMP-DDIR with increasing complexity. The measured values such as hydrogen permeation rate, pressure, and temperature were found to be good qualitative agreement with comprehensive CHAMP-DDIR model predictions. Quantitative predictions of the reactor operation have been also demonstrated for specific periods of the total CHAMP-DDIR operating cycle, and opportunities for further enhancements of the modeling capabilities have been identified and critically assessed.

6.1.2 Engineering practice

- The reactor design principles and operating regime map(s) for the CHAMP-DDIR fuel reformer were formulated based on a parametric study of key design variables using the theoretical model developed, which resulted in identification of the optimal operating points.
- Utility of dynamic modulation of fuel injection in CHAMP-DDIR has been experimentally demonstrated for achieving an improved performance (power density) of the cyclically operated batch reactors.
- Substantial benefits of dynamic control of reactor pressure and its impact on enhancing apparent reaction kinetics and in-situ hydrogen transport/separation have been established through complimentary theoretical analysis and experiments.

6.2 Summary of Conclusions

Based on the combined experimental observations and simulations results, several conclusions can be drawn about feasibility and potential of a new concept of high power density fuel reforming reactor.

- In practically realized fuel reforming systems, such as commonly used continuous-flow reactors, transport limitations are critically important and often substantially reduce the power density of fuel-to-hydrogen conversion. The CHAMP-DDIR class of reactors provides effective means for managing these challenges by directly delivering a fuel mixture to the catalyst surface for rapid flash volatilization and on-a-spot reaction (DDIR) as well as reducing the diffusion distance for desired product(s) transport from the reaction zone to separation/utilization site (CHAMP). Collectively, this results in a possibility to dramatically increase hydrogen production rate and thus improve the volumetric power density, approaching an ideal limit set by the intrinsic reaction kinetics and membrane separation efficiency.

- CHAMP-DDIR's capability to modulate reactor volume during a batch cycle allows for controlling reactor pressure to provide enhanced driving force for the permeation process, resulting maintaining the hydrogen throughput of the reactor at an increased level. This aspect naturally enables dynamic control of hydrogen throughput and control of residence time.
- Improvement in volumetric power density can be made when variable volume operation is combined with modulated fuel introduction, because multiple fuel injections enable higher reaction/permeation rates by preventing a large temperature drop resulting from evaporation of a large quantity of fuel introduced in a single injection, and taking advantage of dynamic volume compression during a batch cycle to reduce the reactor volume and to maintain an elevated reactor pressure beneficial for both reaction and permeation rates.
- A tradeoff exists between power density and hydrogen yield (fuel utilization). Hence, power density should be evaluated in the context of a constraint imposed by a minimal acceptable hydrogen yield.
- Volumetric power density increases monotonically with increasing pressure and catalyst loading and decreasing membrane thickness, especially in the permeation-limited regime. An optimal reactor temperature, with respect to volumetric power density, exists within the allowed temperature range of the catalyst (e.g. maximum power density occurs around 555K when varying temperature between 475 and 575K and pressure between 3-6 bar) due to competing temperature effects: MSR reaction and hydrogen permeation rates increase with temperature (positive effects), but the required reactor volume and heat input also increase (negative effects) with temperature.
- Inclusion of the mass transfer effects to the model is important when predicting a performance of CHAMP-DDIR operating in the bulk mass transfer limited regime (e.g. with thinner membrane, higher specific membrane area, and higher catalyst loading).

The multi-component Maxwell-Stefan formulation predicts a greater impact of internal mass transfer limitation, and thus implies a transition from the permeation limited regime at a greater membrane thickness than the Fickian model indicates.

- With CHAMP-DDIR's variable volume operation, reducing the reactor chamber size not only maintains elevated pressure to promote higher permeation rates, but it also reduces internal mass transfer resistance which plays a significant role. In addition, the trajectory of reactor volume, which changes from highest at the beginning to smallest at the end of cycle, accentuates the benefits of variable volume operation, since volume compression (to keep elevated pressure) occurs in sync with the time when less transport resistance is desired. This aspect is a unique fundamental advantage of a CHAMP-class reactors.
- The impact of differences in the details of the thermal model becomes less important, as the internal thermal resistance is increased (with increased reactor height), a trend that is opposite that seen when considering the effects of mass transfer models. The reason for this different behavior is that heat transfer within the reactor affects performance only in an integral sense through impact on the reactor total pressure, which is minor as compared to the effect of the local catalyst and membrane temperatures that directly govern the rate of reactions and hydrogen permeation.

6.3 Recommendations for Future Work

Some of the discussed conclusions above make the CHAMP-DDIR an attractive alternative design for portable fuel reforming, motivating further research into this class of reactors with several suggestions.

6.3.1 Enhancement of modeling approach

In chapter 5, the comprehensive model predictions were compared with measured parameters during experiment with the CHAMP-DDIR prototype. The comparison showed

good agreements for qualitative behavior and clearly demonstrate the benefits of distinct mode of CHAMP-DDIR operations: control of reactor volume/pressure and dynamic modulation of fuel introduction. However, when closely comparing quantitative data from the experiment and simulation, there is obviously a room for improvement for the model.

1) ***Multi-dimensional effects***: The comprehensive model is developed in 1D with simplifying assumptions that i) side walls are perfectly insulated, ii) injected fuel is evenly spread over the catalyst layer, iii) hydrogen concentration in permeate side of membrane is spatially uniform by perfect mixing with sweep gas, and iv) uniform heat flux applied from bottom of reaction chamber. These idealized conditions may not be realistic in the experimental reactor. For example, the side wall of the reaction chambers (which were made in two versions with stainless steel and glass) will conduct heat from the bottom reactor block on which the chamber sits (Figures 2.3 and 4.1), causing radial temperature gradient by conjugate heat transfer. The area for fuel droplet impingement is determined by position and characteristics of a spray nozzle (spray angle and shape, droplet size and distribution). The multi-dimensional effects are very important, since uneven distribution of fuel causes local hot/cold spot formation on the catalyst layer to decrease reaction rates or fuel droplets end up in the side wall results in the loss of the discussed advantages from the DDIR aspect.

2) ***Transient fuel evaporation model*:** The current model's assumption of instant evaporation of liquid fuel with all energy of vaporization supplied by catalyst results in misprediction of temperature and concentration of fuel at the early stage of cycle. The assumed initial temperature calculated with instant temperature drop by latent heat of fuel evaporation wholly supplied by the capacitive thermal energy storage in the catalyst mass, and the initial species concentrations assumed to be distributed evenly in space with uniform molar fractions may need to be modified to include transient effects. For example, temperature profile can be better represented by considering i) partial evaporation of fuel droplets during transit from the tip of nozzle to catalyst surface and ii) transient temperature

drop/recovery occurring over extended area (not just at catalyst layer). Additionally, the finite thickness of the catalyst layer may need to be accounted for when considering the zone where fuel evaporation takes place. This requires physics based model of droplet and film evaporation (e.g. by extension of steady state analysis of Varady and Fedorov [] to consider transient effects) which accounts for droplet size, density, velocity, catalyst layer, and fuel film thicknesses. [16]. In addition, higher dimension (2D or 3D) models would improve the prediction by including local temperature and species concentration non-uniformities in the catalyst layer.

3) ***Hydrogen at permeate side of membrane*:** Another source of error in the model may be the simplified treatment of the removal of permeated hydrogen on the backside of membrane by sweep gas. In the current model, based on relatively fast diffusional permeation/mixing time relative to the sweep gas residence time when it is in contact with the membrane, it is assumed that the permeated hydrogen is perfectly mixed with a sweep gas[19] as depicted in Figure 6.1a. However, in the prototype reactor (Figure 6.1b), the sweep gas enters at the periphery of the cylindrical gap between membrane and permeation block, swirls along the outer diameter, and exits with hydrogen through the center. This complex flow and variation in local mass transfer performance may be inadequately represented using a constant mass transfer coefficient in the current 1-D model. As a result, the spatially average permeated side hydrogen partial pressure might be higher in the experimental reactor than predicted, leading to slower actual permeation rates. For improving model to match experimental data, the assumption of perfect mixing may have to be relaxed. Figure 6.1c illustrates schematics of a more realistic condition on the permeate side of membrane. It shows that close to the sweep gas inlet, concentration of argon is higher while the opposite side of inlet holds high H_2 concentration. The locally high hydrogen partial pressure due to stagnant hydrogen can cause ineffective utilization of membrane area as well. In order for models to capture this effect, multi-dimensional analysis is required.

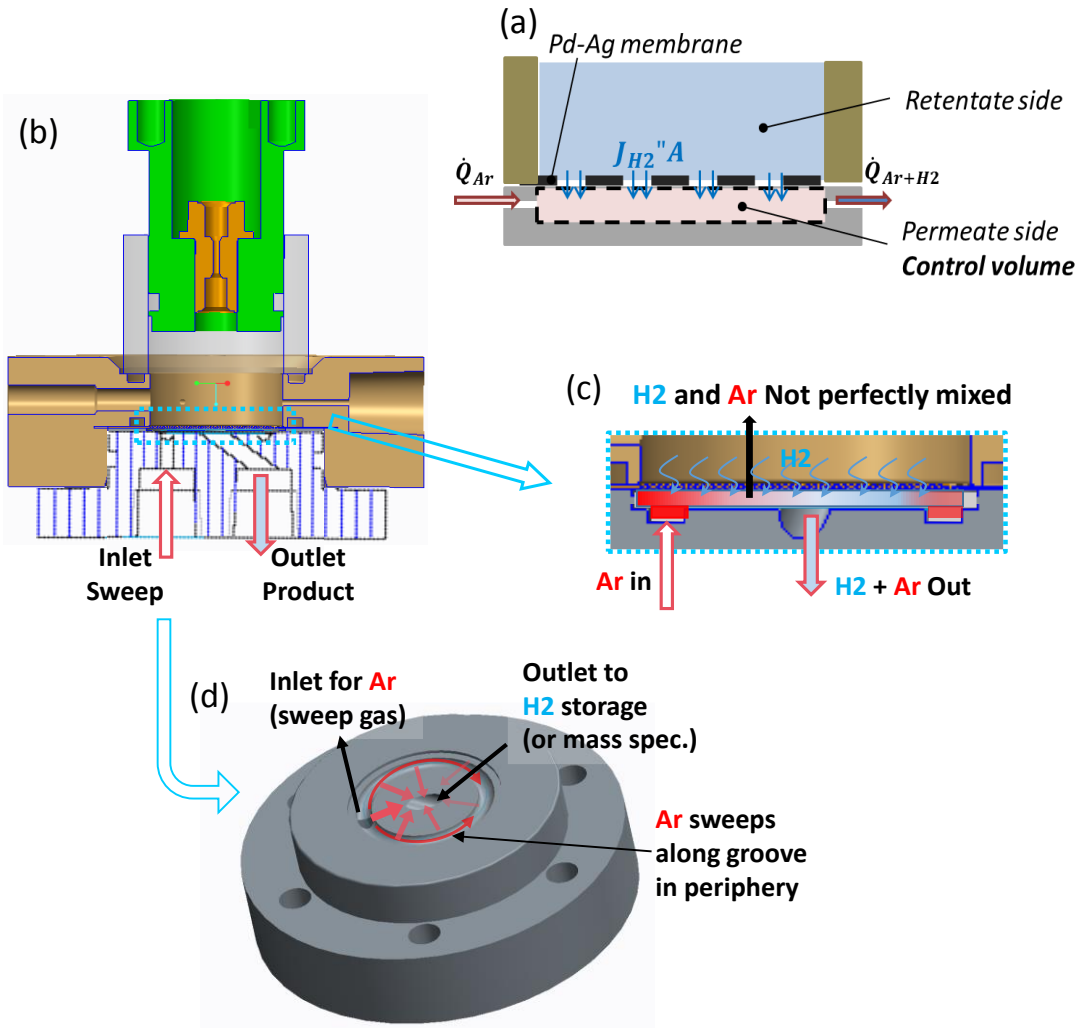

Figure 6.1 The sweep gas enters at the outer diameter of the cylindrical gap between membrane and permeation block, swirls along the periphery, and exits with hydrogen through the center. (a) full assembly of the reactor prototype, (b) current model consideration for hydrogen and argon concentration at the permeate side of membrane (perfectly mixed condition), (c) realistic condition to be considered for improving model, and (d) 3-D view of permeation block showing argon swirl/sweep geometries.

4) ***Transient effect of hydrogen permeation at membrane:*** In Eq. 3.7 for permeated hydrogen mass flux $J_{H2,perm} = {D_{memb}}/{\delta_{\text{memb}}}\ \theta_{avg}(p_{ret,H2}^{0.5} - p_{perm,H2}^{0.5})$, the multiplier, θ_{avg}, accounts for the reduction of permeance due to the surface adsorption of non-H_2 species (CH_3OH, H_2O, CO_2, and CO). The membrane permeance ($D_{memb}\theta_{avg}$) used in our model was found from the membrane permeation model by Israni et. al[69]. Since, this permeation model

was obtained using steady-state measurements, it is only valid if competitive adsorption is very fast and all species attain equilibrium coverage on the membrane. Accounting for the dynamic impact of competitive membrane coverage by non-hydrogen species via an adsorption/desorption kinetics model would provide for more accurate treatment. Unfortunately, since transient effects of adsorption for non-H_2 species on Pd-Ag membrane surface are not known (no such description or experimental data have been reported in the literature), time average value, θ_{avg}, was used in our current model after taking average of $\theta(t)$ over a reaction cycle. The usage of θ_{avg} can be justified as a good approximation for cycle averaged performance. Based on several studies of hydrogen permeation through Pd alloy membrane [93-95], the time scale for adsorption of H atom onto Pd-alloy surface is faster than that for diffusion in membrane considering the conditions (10 μm membrane and 525K) for the simulated CHAMP-DDIR. Since diffusion time scale is ~0.0006 sec (from $\tau_D = \frac{\text{membrane thickness}^2}{\text{mass diffucion coefficient for H in Pd}-\text{Ag}}$), which is much faster than the reaction time scale in CHAMP-DDIR cycle, the dissociative adsorption of hydrogen can be assumed to be even faster process. Unknown is how fast non-hydrogen species adsorb on the membrane surface. If it is a fast process (similar to hydrogen absorption), then the time varying $\theta(t)$ in the current model can be justified for H_2 pemeation flux calculation in CHAMP-DDIR. On the contrary, if it is a slow process, then for the first few cycle(s), adsorption of hydrogen will be dominant over other species and actual hydrogen permeation rate will be higher than the prediction using $\theta(t)$. However, after a long exposure of membrane to non-hydrogen species over many cycles of batch operation, a plausible approximation would be to use the time averaged $\theta(t)$ over the cycle, θ_{avg}. Comparison of model predictions with sets of controlled permeation experiments would be one good way to validate the approximation.

5) ***Mass transfer effect in the catalyst layer:*** The current model assumes the thickness of catalyst layer is infinitesimally thin, so that gradients in temperature and species

concentration could be neglected and their lumped values could be used. The validity of this assumption should be carefully evaluated first. The configuration of the catalyst layer with current model and the experimental DDIR were designed to minimize thermal gradients and concentration gradients in the bed and inside the catalyst particles. The criteria of Mears were used to ensure that temperature gradients and axial dispersion were negligible. The Weiss-Prater criterion was used to ensure that there were no significant internal mass transfer gradients. The detailed calculation are shown in Appendix F. However, take into consideration of the thicker catalyst layer (which scale up with the reactor size), inter-/intra- particle mass transfer effect need to be included in the model

6.3.2 Further optimization of the reactor design for system level

The developed CHAMP-DDIR comprehensive model serves as a tool to understand the dynamics of the coupled reaction, permeation, and transport processes. For example, the transition between reaction limited, permeation limited and diffusion limited regimes have been mapped out and important insights and design rules were identified.

For the next step, optimization of the reactor as part of the whole power generation/energy conversion system, and not just an isolated, stand-alone fuel processing unit can be carried out. For example, CHAMP-DDIR can be incorporated with a fuel cell and designed for a certain target power output. The generated pure hydrogen can be fed to the anode of the fuel cell placed in an intimate contract to the permeate side of the fuel reformer membrane. Since a single CHAMP-DDIR have fluctuation in hydrogen production rate during a cycle as well as a down-time (exhaust and refill) time between cycles, to provide a stable or continuous hydrogen stream, multiple stacks of reaction chambers can be operated in parallel with optimized sequences (similar to configurations of an internal combustion engine).

6.3.3 Modeling of autothermal operation

Extension of CHAMP-DDIR model to autothermal reaction of methanol should be straightforward given appropriate kinetics data [98], which is far more sparse than that for steam reforming. What is particularly appealing about this reaction is that the heat for vaporizing and heating the liquid is produced directly at the point of contact with the catalyst without the need for external heat input. Reactor sizing and aspect ratio take on a more important role as mixing of the vaporized feed at the interface with input air must occur while the heat produced from the exothermic reaction must be effectively spread over the catalyst bed. Autothermal reforming reactors would be particularly suited for applications requiring high power densities since none of the useful energy produced in the form of hydrogen would be wasted for heating. However, integration of a hydrogen separation membrane is crucial to for producing a fuel cell feed of sufficient purity.

6.3.4 Free piston dual chamber CHAMP-DDIR

Dual-chamber CHAMP-DDIR can be explored to further improve performance of a baseline CHAMP- DDIR by eliminating the overhead associated with the active control of the reactor volume. The main idea behind the dual-chamber design is the elimination of dead volume by designing a reactor in which the reforming reaction occurs on both sides of the piston. Figure 6.2 shows the simplified configuration of the Dual Chamber CHAMP-DDIR. Assuming a quasi-equilibrium process, the motion of the piston is defined by a mechanical balance of pressures in both chambers. In other words, because the piston moves freely, the pressure in the left and right chambers must be the same at each instant of time in the limit of quasi-equilibrium operation.

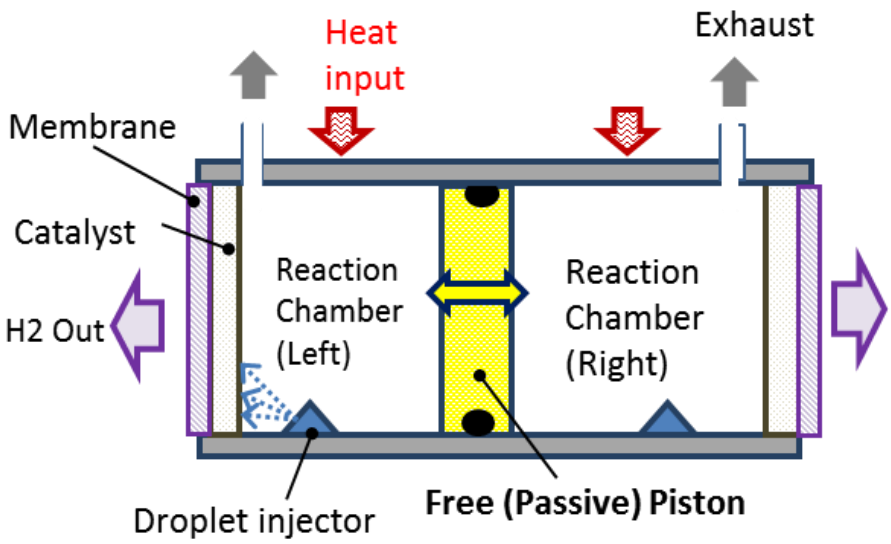

Figure 6.2 Free Piston Dual Chamber CHAMP-DDIR

A key operational characteristic of the free-piston/dual-chamber CHAMP-DDIR is that in both chambers, the reaction occurs in a cycle with the same trajectory of pressure and volume time evolution, but a half-period phase lag exists between the cycles in the two chambers. Figure 6.3 shows a simplified diagram of the four-step cycle used for the free piston/dual-chamber reactor. Figure 6.4 shows a qualitative example of pressure and reactor volume evolution corresponding to each step in Figure 6.3. The first step depicted in Figure 6.3 is fuel injection onto the heated catalyst in the left chamber. As volume in the left chamber increases, the free piston compresses the right chamber (which is in the middle of its cycle) and pressure rises in both chambers to the maximum pressure of the cycle. At this point in the cycle, the reaction rate in the left chamber is high due to the preponderance of reactants, whereas in the right chamber, the elevated pressure reinvigorates lagging reaction and permeation that would have otherwise been observed in a constant volume batch reactor in the latter half of its operating cycle. The volume of the left chamber reaches its maximum at step 2, and the piston comes to rest momentarily, as the time rate of change of the total number of moles in the chambers are equal to one another. As hydrogen permeation rate increases over production rate in the left chamber, the piston starts to shift

towards the left. Simultaneously, the cycle in the right chamber is nearing completion. The remaining gases in the right chamber are exhausted, thus completing the half cycle, and preparing the right chamber for fuel introduction. Steps 3 and 4 follow from steps 1 and 2, *mutatis mutandum*.

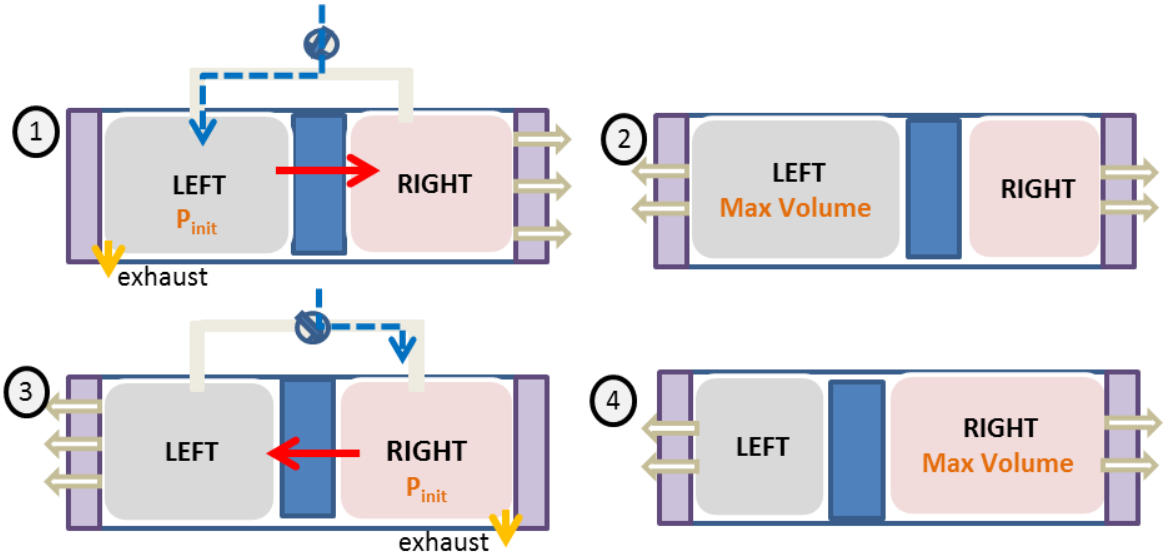

Figure 6.3 Four steps of free-piston dual-chamber CHAMP-DDIR cycle. 1) Left chamber, exhaust remainder – intake reactants – reaction with high reaction rate. Piston shifts to right. 2) Maximum volume for left chamber during reaction-permeation on both side. 3) Right chamber, exhaust non-permeated products - intake reactants. Piston shifts to left. 4) Maximum volume for right chamber.

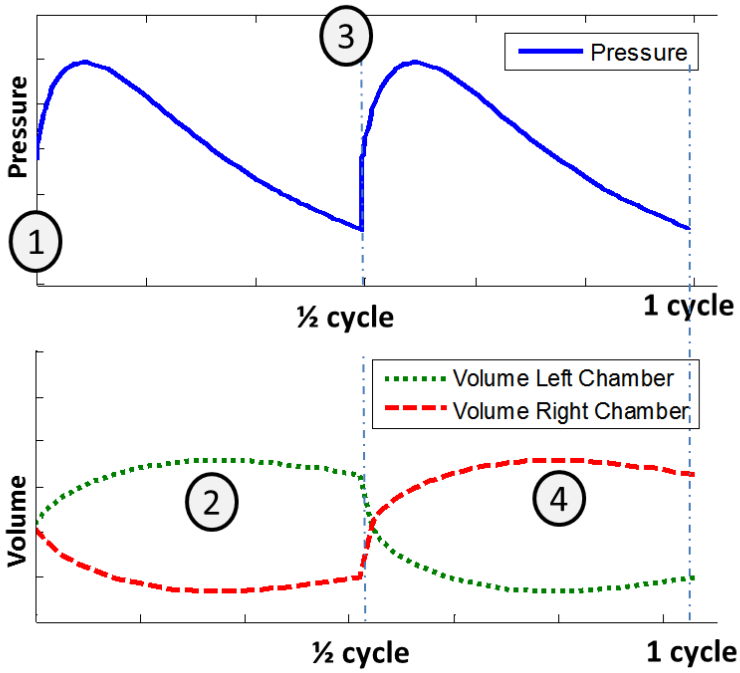

Figure 6.4 Pressure (top), and volume (bottom) evolution with time for free-piston dual-chamber CHAMP-DDIR. The free piston keeps pressure in the left and right chambers equal in the limit of quasi-equilibrium operation. Under constant temperature operation, total pressure and chamber volume profiles are dictated by the changing number of moles of gas in the chambers, which results from the combined effects of catalyzed steam reforming reactions and selective product permeation.

In addition to the potential improvement in power density, there are other practical benefits to the dual-chamber/ free-piston CHAMP-DDIR. By having a passive piston, design is simplified with fewer parts. No active control of the piston is required. Furthermore, the seal for the passive piston is against a balanced pressure, and any gases that leak past the seal do not escape the reactor.

APPENDIX A

SYSTEM DENSITY, BALANCE OF PLANT (BOP) COMPONENTS, AND THERMAL MANAGEMENT CONSIDERATIONS IN CHAMP-DDIR SYSTEM

The CHAMP-DDIR system's balance of plant (BOP) consists of fuel tank, fuel injector/pumps, valves, piston actuator, insulation, etc. It is understood that including their mass/volume and efficiencies will alter quantitative results on mass- and volume-based power density calculation. However, we do not include those in our results, because the overarching focus this study is to find the optimal conditions that would lead to maximization of the volumetric density of fuel to hydrogen conversion specifically in CHAMP-DDIR (rather than quantitative comparison that with other reactor design) with an implicit assumption that the BOP components are not bottlenecks in achieving high power density hydrogen generation and can be selected to support a chosen reactor design/operation. Nevertheless, one of the key compelling features of combining CHAMP and DDIR concepts is to exploit multi-functionality of components, including BOP for minimizing the system volume/mass. For example, fuel tank which holds liquid fuel (water-methanol mixture) at room temperature can be small, the fuel injectors are integrated into the piston (Figure 3.1 in chapter 3), surfaces requiring insulation can be relatively small since aspect ratio (Gap Height/Reactor Lateral Extent) is low for CHAMP-DDIR (as compared to the CF reactor designs). Most importantly, DDIR eliminates the need for an external evaporator, which is often one of the bulkiest and most difficult to stably operate BOP component. All of these design aspects positively contribute to enhance the overall system density of CHAMP-DDIR.

Thermal management is a fundamental concern for any reactor which requires an elevated temperature operation; however it is much less so for the transient CHAMP-class reactors

as compared to the conventional CF reactors. It is in fact one of the key fundamental advantages of CHAMP-DDIR that it supplies heat with time (rather than space) domain control, thus allowing for precise "dosing" of heat supply to the reactor zone locally where it is most needed, without excessive overheating of an entire reactor structure (which results in elevated heat losses in conventional CF reactors). Further, the "tablet" form factor of a typical CHAMP-DDIR design with low aspect ratio (i.e., the gap height vs. lateral extent) minimizes the specific (per unit volume) area of the external walls, which are main conduits for heat losses from the reactor chamber.

APPENDIX B

MEMBRANE PERMEATION MODEL: FINDING PERMEANCE REDUCING FACTOR ON RETENTATE SIDE AND PARTIAL PRESSURE OF HYDROGEN ON THE PERMEATE SIDE

B-1. Finding θ_{avg} (multiplier for reduction effect on H2 permeance due to Non-H2 species)

In Eqs. 3.7 and 5.11 for permeated hydrogen mass flux $J"_{H2} = \theta_{avg} Q \left({P_{ret,H2}}^{0.5} - {P_{perm,H2}}^{0.5} \right)$, the multiplier, θ_{avg}, accounts for the reduction of permeance due to the surface adsorption of non-H_2 species (CH_3OH, H_2O, CO_2, and CO). In the published model by Israni et. al. [69], instead of θ_{avg}, $(\theta_V + \theta_H)$ is used, where θ_V is the fraction of vacant surface adsorption sites (potentially available for H atoms) and θ_H is the fraction of surface sites already occupied by H atoms. $(\theta_V + \theta_H)$, which is 1 when membrane is exposed to pure hydrogen, decreases with an increase in adsorption of non-hydrogen species.

The multiplier $(\theta_H + \theta_V)$ is semi-empirically calculated based on steady-state behavior (so, strictly speaking the original Israni's model cannot be directly applied for dynamically varying CHAMP-DDIR operation). Since transient effects of adsorption for non-H_2 species on Pd-Ag membrane surface are not known, time average value, θ_{avg}, is used in the model after taking average of $(\theta_H + \theta_V)$ over a reaction cycle.

The usage of θ_{avg} can be justified as a good approximation for cycle averaged performance. Based on several study of hydrogen permeation through Pd alloy membrane [93-95], the time scale for adsorption of H atom onto Pd-alloy surface is faster than that for diffusion in membrane considering the conditions (10 μm membrane and 525K) for the simulated CHAMP-DDIR. Since diffusion time scale is ~0.0006 sec (from $\tau_D =$

$\frac{\text{membrane thickness}^2}{\text{mass diffucion coefficient for H in Pd}-\text{Ag}}$), which is much faster than the reaction time scale in CHAMP-DDIR cycle, the adsorption of H atom can be assumed to be even faster process. Unknown is how fast non-hydrogen species adsorb on the membrane surface. If it is a fast process (similar to H absorption), then the time varying $(\theta_H + \theta_V)$ from the original model can be used for H_2 flux calculation in CHAMP-DDIR. On the contrary, if it is a slow process, then for the first few cycle(s), adsorption of H atom will be dominant over other species and actual hydrogen permeation rate will be higher than the prediction using $(\theta_H + \theta_V)$. However, after a long exposure of membrane to non-hydrogen species over many cycles of batch operation, a plausible approximation would be to use the time averaged $(\theta_H + \theta_V)$ over the cycle θ_{avg}. Further experiments are required to assess the validity of this treatment.

B-2. Hydrogen Flux due to Partial Pressure on Permeate Side

The partial pressure of hydrogen on the permeate side, $P_{perm,H2}$, used in Eq. (5.11), is found by considering species mass conservation for a control volume at the permeate side of membrane (Figure B). Based on relatively fast diffusional permeation/mixing time relative to the sweep gas residence time when it is in contact with the membrane, we assume that the permeated hydrogen is perfectly mixed with a sweep gas and treat the problem as quasi-steady state to obtain

$$J_{H2}"A = \dot{Q}_{Ar+H2}\left(P_{perm,H2}/RT\right)$$

which requires that the permeation rate of hydrogen through the membrane is equal to the rate of hydrogen leaving the control volume as a gaseous mixture with argon.

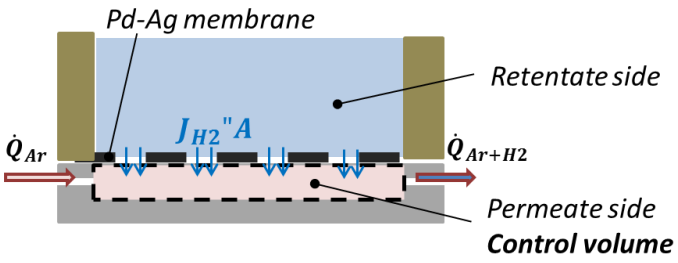

Figure B. Schematics of CHAMP-DDIR membrane region for hydrogen permeation model. The hydrogen flux across the membrane, J''_{H2}, is found through simultaneous solution of Eqs. (S5) and (S10). In Eq. (S5), the membrane permeance, Q, is found using $Q = \frac{Q_o}{\delta_{\text{memb}}} exp(-\frac{E_H}{RT})$, [42] with Q_o and E_H obtained from experimental data of pure hydrogen permeation test using linear regression: Q_o =1.78e-07 $\left[\frac{mol}{m \cdot s \cdot pa^{0.5}}\right]$; and, E_H =10.8 $[\frac{kJ}{mol}]$

APPENDIX C

TIME SCALE ANALYSIS FOR FUEL DROPLET EVAPORATION

Based on the original DDIR study by Varady and Fedorov[16, 17, 56], the fuel droplet evaporation in DDIR can occur in two modes: (1) in-transit during the fuel droplet traveling from the fuel injector to the catalyst layer and 2) on the catalyst surface after forming a thin liquid fuel layer. For mode (1) the droplet evaporation time scale is given by

$$\tau_{evap,drop} = \frac{R_{drop}^2}{K}$$

where R_{drop} is an initial radius of a droplet, and K is the evaporation constant, which can be either heat transfer or mass transfer limited [70]. For heat transfer limited evaporation,

$$K = \frac{k_g}{\rho_l C_{p,g}} Nu_d ln\left(\frac{c_{p,g}(T_g - T_d)}{h_{fg}} + 1\right)$$

And for the mass transfer limited case,

$$K = \frac{\rho_g D_g}{\rho_l} Sh_d ln\left(\frac{1-y_{f,\infty}}{1-y_{f,s}}\right)$$

Where ρ_l and ρ_l are density of liquid and gas, respectively, $C_{p,g}$ is specific heat of gas, k_g is thermal conductivity of gas, h_{fg} is latent heat of evaporation, and $D_g$is gas diffusion coefficient. The dimensionless heat and mass transfer coefficients are estimated from the correlations of Ranz and Marshall, $\mathrm{Nu_d} = 2 + 0.552\mathrm{Re_d^{1/2}}\,\mathrm{Pr_d^{1/3}}$ and $\mathrm{Sh_d} = 2 + 0.552\mathrm{Re_d^{1/2}}\,\mathrm{Sc_d^{1/3}}$, respectively.

For thin film evaporation, mode (2), time scale is defined by

$$\tau_{evap,film} = \frac{\rho_l h_{film}^2 h_{fg}}{k_g(T_\infty - T_S)}$$

where h_{film} is the film thickness and T_S is saturation temperature. [72]

The representative fuel injection conditions in the reactor used in our simulations are as follows: gas temperature 475K, transit distance 2cm, 10μL injection over 1.76cm^2 area with an average droplet diameter 50μm, and thermophysical properties are $k_{g,w}$ =0.0383 W/m-K, $\rho_{l,w}$ = 996.6 kg/m^3, $\rho_{g,w}$ =1.27 kg/m^3, $c_{p,g,w}$ =1.9 kJ/kg-K, $h_{fg,w}$ =2257 kJ/kg, $k_{g,m}$ = 0.0417 W/m-K, $\rho_{l,m}$ = 784.6 kg/m^3, $\rho_{g,m}$ =0.419 kg/m^3, $c_{p,g,m}$ =1.9 kJ/kg-K, $h_{fg,m}$=1102 kJ/kg, resulting in dimensionless numbers Re_d~5, Pr_d~ 0.1, Sc_d~0.1.

Using the above conditions, evaporation time scales can be estimated for both methanol and water (the results for the evaporating methanol-water mixture are bracketed by computations for methanol and water as limiting cases).

Time scale for droplet evaporation (~0.5 sec), which is mass transfer limited, is substantially longer than droplet flight time (~0.002 sec), therefore evaporation as a thin film will be the dominant mode. In that case, evaporation time scales are $\tau_{evap,film,H2O}$ = 0.0031sec and $\tau_{evap,film,CH3OH}$ =0.00011sec. As all of the estimated evaporation time scales are in the order of 10^{-4} and much smaller that the CHAMP reaction cycle time (~10s sec), evaporation of fuel can be justifiably treated as instantaneous.

APPENDIX D

NUMERICAL SOLUTION METHODS FOR IDEAL MODEL

D-1. Numerical solution methods – Idealized model (No Heat and Mass Transfer Effects)

For numerical solution of the model equations, each equation given in *Eq.* (3.12a)-(3.12e) in chapter 3 was explicitly integrated forward in time. For example, the number of moles of methanol in the reactor at the n+1 time step is approximated as $(N_{\mathrm{CH3OH}}^{(n+1)} - N_{\mathrm{CH3OH}}^{(n)}) / \Delta t = \rho_{cat} A d(-r_{SR} - r_{MD})^{(n)}$. The rate expressions are highly non-linear initially, when the concentration of products is very small, therefore a short time step (0.001 s) was required in order to achieve time step independent results. The implementation of the kinetic expressions was validated by setting the membrane permeability to zero and reproducing the results presented by Peppley et al.[34, 68] in terms of methanol conversion versus residence time.

D-2. Numerical solution methods – Mass transfer, time varying temperature model

For numerical solution of model equations in chapter 3,

$$\frac{\partial C_i}{\partial t} + \frac{\partial (C_i v)}{\partial z} = D_i \frac{\partial^2 C_i}{\partial z^2} \qquad (3.15)$$

an implicit method was used for discretizing the diffusive fluxes based on species concentrations at the next time step to ensure stability of transient calculations, which yields the following finite difference approximation of the species transport equations. The time derivative for a given species concentration at each node location, was approximated by the forward difference method, that is, $\frac{\partial C_j}{\partial t} = \frac{(C_j^n)_P - (C_j^o)_P}{\Delta t}$ where index 'n' refers to the

current (new) time and 'o' refers to the past (old) time step (Figure D). The advective flux gradient term was approximated using a first order upwind scheme, which is written as,

$$\frac{\partial(C_j \mathrm{v})}{\partial z} = \frac{\left(c_j^n\right)_n v_n - \left(c_j^n\right)_s v_s}{\Delta z} = \frac{\left([\![v_n,0]\!]\left(c_j^n\right)_P - [\![-v_n,0]\!]\left(c_j^n\right)_N\right) - \left(-[\![v_s,0]\!]\left(c_j^n\right)_P + [\![v_s,0]\!]\left(c_j^n\right)_S\right)}{\Delta z}.$$

The diffusion term was approximated using the central difference scheme:

$$\frac{\partial^2 C_j}{\partial z^2} = \frac{\left(c_j^n\right)_{\mathrm{N}} - 2(C_j^n)_{\mathrm{P}} + (C_j^n)_S}{\Delta z^2}.$$

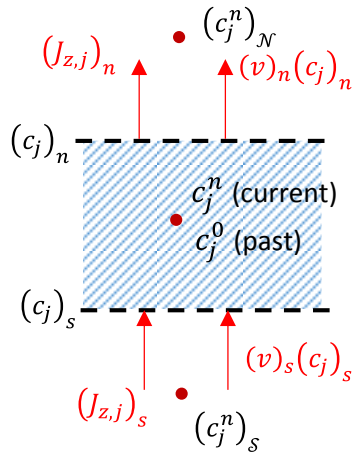

Figure D. Notation for values of dependent variables and fluxes at a representative grid-point cluster for developing the finite difference equations. Three spatial elements are denoted as N, S, and P (North, South, and Point) and two time steps are *n* and *o* (current and previous/old time instants, respectively).

The resulting set of equations for each species at the given time step was expressed in matrix form as, $[K]\overrightarrow{C} = \vec{r}$. where K is N×N coefficient matrix, and $\overrightarrow{C^n}$ and $\vec{r}$ are N×1 vectors. Matlab was used to find solutions iteratively for these implicitly discretized equations.

APPENDIX E

IMPACT OF THE INITIAL CONDITIONS CONSIDERING TWO LIMITING CASES FOR SPECIES CONCENTRATION

A numerical investigation of the impact of the initial conditions was performed considering two limiting cases for species concentration resulting from droplets sprayed into a reaction chamber filled with argon: 1) a uniform mixture of water, methanol and argon assuming rapid mixing during evaporation; and, 2) stratified gas layers resulting from rapid vaporization of the fuel on the catalyst creating a methanol/ water vapor layer in the reactor bottom near the catalyst/membrane surface in mechanical equilibrium with a compressed argon layer above it (i.e. no mixing during evaporation).

For case 1), molar fractions of all species at the initial stage are assumed to be uniform in space while the species concentrations vary due to non-uniform temperature. This initial condition was used for all simulation results presented in chapter 5 and the associated pressure and temperatures are found. For case 2), the bottom layer is composed of fuel (mole fractions of methanol and water are both 0.5) and the top layer is argon only. The size (volume per unit area of the membrane) of the two layers, and the temperature of each, are found by assuming the prefilled argon is isentropically compressed by instant expansion of the evaporating fuel in an adiabatic process. The energy conservation ($\Delta U_{cv} = Q_{cv} - W_{cv} = 0$) in the gas domain including argon, fuel and catalyst can be written as followings

$$m_{cat} c_{p,cat}(T_{cat1} - T_{cat0}) + \sum_{\substack{i=H2O, \\ CH3OH}} N_i[u_{fg,i} + \overline{c_{v,i}}\left(T_{fuel_{sat},i,1} - T_{liq,i,0}\right)] +$$

$$N_{Ar}\overline{c_{v,Ar}}\left(T_{Ar,1} - T_{Ar,o}\right) = 0$$

Subscripts, 0 is for the state prior to fuel evaporation, and 1 is immediately after the evaporation. For finding volume of each layer ($V_{fuel,1}$, $V_{Ar,1}$), temperature ($T_{fuel\_sat,1}$, $T_{Ar,1}$), pressure (P_1, spatially uniform within the reactor), equation of state must be used with the thermodynamic relationship between properties for isentropic process.

$$\frac{P_1}{P_0} = \left(\frac{V_0}{V_{Ar,1}}\right)^{\gamma}$$

The simulation results revealed that when the time scales for species/thermal diffusion in the reactor, reaction, and permeation are all of similar magnitude, the initial condition has a non-negligible impact on the predicted reactor performance. In Fig E-1, when reactor height is 0.2cm, the predictions from two models with different initial conditions show about 6% difference in power density. On the other hand, when the time scale for reaction and/or permeation is much greater than the diffusion time scale, the choice of initial condition has little effect. This is the case with experimental reactor under operating conditions (reactor height > 1 cm). Since there is little difference in the predictions of the two limiting cases for the reactor size under consideration, the initial condition can be chosen for convenience, and in all simulations reported in this dissertation the perfectly mixed reactor initial condition (case 1) was used due to simplicity of its implementation.

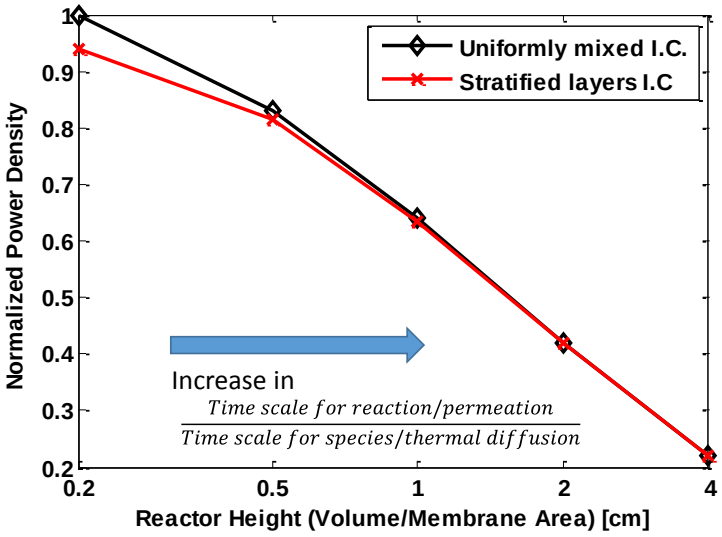

Figure E-1. Power density predictions as a function of reactor height (constant volume operation) using two different initial conditions: uniform mixture of species vs. stratified gas layers of fuel and argon. The difference between two model predictions is negligible so long as the time scales for reaction and permeation exceed that of species/thermal diffusion.

APPENDIX F

EVALUATION OF MASS TRANSFER EFFECT IN THE CATALYST LAYER

The Weisz-Prater criterion, C_{W-P}, is used to estimate the influence of internal mass diffusion on the rate of reaction $\Re$: [96]

$$C_{W-P} = \frac{-\Re \rho_c R_P^2}{C_s D_{eff}}$$

If $C_{W-P} \ll 1$ there are no diffusion limitations and consequently no concentration gradient exists within the pellet. η is an effectiveness factor, ρ_c is catalyst density, R_p is the catalyst particle radius, C_s is species surface concentration, and D_{eff} is effective diffusivity. Using values from the baseline simulation in Figure 5.9 (which are also similar to the respective parameter values for the experimental CHAMP-DDIR operation), i.e., ρ_c*=1300 kg/m*^{3}, R_p*=100* μ*m,* D_{eff} *= 6.5e-5 m*^{2}*/s,* C_s*=10 mol/m*^{3}, and $\Re$*=0.0105 mol/kg,* the Weisz-Prater criterion, $C_{W\text{-}P}$, is about *2e-4*; therefore, internal diffusion limitation can be neglected.

The Mears' criterion uses the measured rate of reaction $\Re$ to check if mass transfer from the bulk gas phase to the catalyst surface can be neglected. Mass transfer effects can be neglected if

$$-\frac{\Re(1-\phi)\rho_c R_p n}{k_c C_b} < 0.15$$

where n is the reaction order, R_p is the catalyst particle radius, C_b is the reactant bulk concentration, k_c is mass transfer coefficient, and ϕ is bed porosity. [97] Using the same values used for Figure 5.9, i.e., ρ_c*=1300 kg/m*^{3}*,* R_p*=100* μ*m,* D_{eff} *= 6.5e-5 m*^{2}*/s,* C_b*=10 mol/m*^{3}, and $\Re$*=0.0105 mol/kg,* ϕ*=0, n=3, and* k_c *=* D_{eff}*/H,* with *H = 0.02 m*, the Mears' criterion has a value of about 0.13, very close to the cut off value. This is in agreement with simulations, which show a small but important effect of external mass diffusion from the bulk gas to the catalyst surface.

APPENDIX G

DUFOUR AND SORET EFFECTS

In the energy conservation equation (Eq. 5.7) for the comprehensive model, the Dufour effect, which is defined as energy flux due to a mass concentration gradient, is included as $\frac{\partial}{\partial z}\left(\sum_i J_i \bar{h}_i\right)$. On the other hand, in the species mass conservation equation, Eqs. (5.1) and (5.2), the Soret effect, which is diffusional flux induced by temperature gradient, is neglected. In this Appendix, the importance of both effects is discussed.

The importance of the Dufour effect is determined by comparing the relative magnitude of advective energy flux to that of diffusive energy flux. Comparison of two energy flux components in the representative simulation in Figure 5.9, shows that the relative magnitude of the two effects varies during the transient operation, with both being of similar order at the beginning of the cycle, and the Dufour term's contribution becoming less important later in the cycle. It is because of the importance of the Dufour effect in the beginning of the cycle that this term must be included in the analysis.

The importance of the Soret effect can be estimated by comparison of the diffusive flux due to the concentration gradient to the flux induced by the temperature gradient. Both terms are retained in the expression for Fickian diffusive flux with the Soret effect in Eq. (G1) [82]:

$$J_A = -cD_{AB}\left[\underbrace{\nabla x_A}_{\substack{\text{diffusive flux by} \\ \text{concentration gradient}}} + \underbrace{k_T \nabla \ln T}_{\substack{\text{flux induced by} \\ \text{temperature gradient}}}\right] \qquad \text{(Eq. G1)}$$

In Eq. (G1) k_T is the thermal diffusion ratio, which is a function of species, mole fraction, and temperature. Typical values of k_T for gaseous species are no greater than 0.1. Because the Lewis number for gases is order 1, the characteristic length for thermal diffusion and

mass diffusion are similar, so the Soret effect can be neglected provided $T\Delta x_A/(k_T \Delta T) \gg 1$. Mole fraction changes are ~ 1, and in this work, T ~ 500K, and the maximum ΔT is ~ 50K, resulting in $T\Delta x_A/(k_T \Delta T) \sim 100$. Therefore the contribution of the Soret effect can be neglected for simplification of the species mass conservation equations.

REFERENCES

[1] Flipsen, S. F. J., Power sources compared: The ultimate truth? *Journal of Power Sources* **2006,** 162, (2), 927-934.

[2] Broussely, M.; Archdale, G., Li-ion batteries and portable power source prospects for the next 5-10 years. *Journal of Power Sources* **2004,** 136, (2), 386-394.

[3] Girishkumar, G.; McCloskey, B.; Luntz, A. C.; Swanson, S.; Wilcke, W., Lithium - Air Battery: Promise and Challenges. *Journal of Physical Chemistry Letters* **2010,** 1, (14), 2193-2203.

[4] Winter, M.; Brodd, R. J., What are batteries, fuel cells, and supercapacitors? *Chemical Reviews* **2004,** 104, (10), 4245-4269.

[5] Dyer, C. K., Fuel cells for portable applications. *Journal of Power Sources* **2002,** 106, (1-2), 31-34.

[6] Hertz, J. L.; Tuller, H. L., Electrochemical characterization of thin films for a micro-solid oxide fuel cell. *Journal of Electroceramics* **2004,** 13, (1-3), 663-668.

[7] Palo, D. R.; Holladay, J. D.; Rozmiarek, R. T.; Guzman-Leong, C. E.; Wang, Y.; Hu, J. L.; Chin, Y. H.; Dagle, R. A.; Baker, E. G., Development of a soldier-portable fuel cell power system Part I: A bread-board methanol fuel processor. *Journal of Power Sources* **2002,** 108, (1-2), 28-34.

[8] Holladay, J. D.; Wainright, J. S.; Jones, E. O.; Gano, S. R., Power generation using a mesoscale fuel cell integrated with a microscale fuel processor. *Journal of Power Sources* **2004,** 130, (1-2), 111-118.

[9] White, C. M.; Steeper, R. R.; Lutz, A. E., The hydrogen-fueled internal combustion engine: a technical review. *International Journal of Hydrogen Energy* **2006,** 31, (10), 1292-1305.

[10] Ogden, J. M.; Steinbugler, M. M.; Kreutz, T. G., A comparison of hydrogen, methanol and gasoline as fuels for fuel cell vehicles: implications for vehicle design and infrastructure development. *Journal of Power Sources* **1999,** 79, (2), 143-168.

[11] Demirdöven, N.; Deutch, J., Hybrid Cars Now, Fuel Cell Cars Later. *Science* **2004,** 305, (5686), 974-976.

[12] Ferreira-Aparicio, P.; Benito, M. J.; Sanz, J. L., New Trends in Reforming Technologies: from Hydrogen Industrial Plants to Multifuel Microreformers. *Catalysis Reviews* **2005,** 47, (4), 491-588.

[13] Ogden, J. M., Prospects for building a hydrogen energy infrastructure. *Annual Review of Energy and the Environment* **1999,** 24, (1), 227-279.

[14] Damm, D. L.; Fedorov, A. G., Comparative assessment of batch reactors for scalable hydrogen production. *Industrial & Engineering Chemistry Research* **2008,** 47, (14), 4665-4674.

[15] Damm, D. L.; Fedorov, A. G., Batch Reactors for Hydrogen Production: Theoretical Analysis and Experimental Characterization. *Industrial & Engineering Chemistry Research* **2009,** 48, (12), 5610-5623.

[16] Varady, M. J.; Fedorov, A. G., Fuel Reformation and Hydrogen Generation with Direct Droplet Impingement Reactors: Model Formulation and Validation. *Industrial & Engineering Chemistry Research* **2011,** 50, (16), 9502-9513.

[17] Varady, M. J.; Fedorov, A. G., Fuel Reformation and Hydrogen Generation with Direct Droplet Impingement Reactors: Parametric Study and Design Considerations for Portable Methanol Steam Reformers. *Industrial & Engineering Chemistry Research* **2011,** 50, (16), 9514-9524.

[18] Yun, T. M.; Kottke, P. A.; Anderson, D. M.; Fedorov, A. G., Experimental investigation of hydrogen production by variable volume membrane batch reactors with modulated liquid fuel introduction. *International Journal of Hydrogen Energy* 40, (6), 2601-2602.

[19] Yun, T. M.; Kottke, P. A.; Anderson, D. M.; Fedorov, A. G., Power Density Assessment of Variable Volume Batch Reactors for Hydrogen Production with Dynamically Modulated Liquid Fuel Introduction. *Industrial & Engineering Chemistry Research* **2014,** 53, (47), 18140-18151.

[20] Holladay, J. D.; Wang, Y.; Jones, E., Review of developments in portable hydrogen production using microreactor technology. *Chemical Reviews* **2004,** 104, (10), 4767-4789.

[21] Kim, T., Micro methanol reformer combined with a catalytic combustor for a PEM fuel cell. *International Journal of Hydrogen Energy* **2009,** 34, (16), 6790-6798.

[22] Mitsos, A.; Chachuat, B.; Barton, P. I., What is the design objective for portable power generation: Efficiency or energy density? *Journal of Power Sources* **2007,** 164, (2), 678-687.

[23] Kaisare, N. S.; Lee, J. H.; Fedorov, A. G., Operability analysis and design of a reverse-flow microreactor for hydrogen generation via methane partial oxidation. *Industrial & Engineering Chemistry Research* **2005,** 44, (22), 8323-8333.

[24] Damle, A. S., Hydrogen production by reforming of liquid hydrocarbons in a membrane reactor for portable power generation - Model simulations. *Journal of Power Sources* **2008,** 180, (1), 516-529.

[25] Lindstrom, B.; Pettersson, L. J., Hydrogen generation by steam reforming of methanol over copper-based catalysts for fuel cell applications. *International Journal of Hydrogen Energy* **2001,** 26, (9), 923-933.

[26] Westerterp, K. R., Multifunctional Reactors. *Chemical Engineering Science* **1992,** 47, (9-11), 2195-2206.

[27] Agar, D. W., Multifunctional reactors: Old preconceptions and new dimensions. *Chemical Engineering Science* **1999,** 54, (10), 1299-1305.

[28] Blomen, L. J. M. J.; Mugerwa, M. N., *Fuel cell systems*. Plenum Press: New York, 1993; p xix, 614 p.

[29] Haryanto, A.; Fernando, S.; Murali, N.; Adhikari, S., Current Status of Hydrogen Production Techniques by Steam Reforming of Ethanol: A Review. *Energy & Fuels* **2005,** 19, (5), 2098-2106.

[30] Chen, Z.; Yan, Y.; Elnashaie, S. S. E. H., Catalyst deactivation and engineering control for steam reforming of higher hydrocarbons in a novel membrane reformer. *Chemical Engineering Science* **2004,** 59, (10), 1965-1978.

[31] Kolb, G., The Chemistry of Fuel Processing. In *Fuel Processing*, Wiley-VCH Verlag GmbH & Co. KGaA: 2008; pp 17-55.

[32] Agrell, J.; Birgersson, H.; Boutonnet, M., Steam reforming of methanol over a Cu/ZnO/Al2O3 catalyst: a kinetic analysis and strategies for suppression of CO formation. *Journal of Power Sources* **2002,** 106, (1-2), 249-257.

[33] Idem, R. O.; Bakhshi, N. N., Production of Hydrogen from Methanol .1. Catalyst Characterization Studies. *Industrial & Engineering Chemistry Research* **1994,** 33, (9), 2047-2055.

[34] Peppley, B. A.; Amphlett, J. C.; Kearns, L. M.; Mann, R. F., Methanol-steam reforming on Cu/ZnO/Al2O3. Part 1: The reaction network. *Applied Catalysis a-General* **1999,** 179, (1-2), 21-29.

[35] Holladay, J. D.; Jones, E. O.; Phelps, M.; Hu, J. L., Microfuel processor for use in a miniature power supply. *Journal of Power Sources* **2002,** 108, (1-2), 21-27.

[36] Sa, S.; Silva, H.; Brandao, L.; Sousa, J. M.; Mendes, A., Catalysts for methanol steam reforming-A review. *Applied Catalysis B-Environmental* **2010,** 99, (1-2), 43-57.

[37] Mitsos, A.; Chachuat, B.; Barton, P. I., Methodology for the design of man-portable power generation devices. *Industrial & Engineering Chemistry Research* **2007,** 46, (22), 7164-7176.

[38] Palo, D. R.; Holladay, J. D.; Rozmiarek, R. T.; Guzman-Leong, C. E.; Wang, Y.; Hu, J.; Chin, Y. H.; Dagle, R. A.; Baker, E. G., Fuel processor development for a soldier-portable fuel cell system. *Microreation Technology* **2001**, 359-367.

[39] Mitsos, A.; Palou-Rivera, I.; Barton, P. I., Alternatives for micropower generation processes. *Industrial & Engineering Chemistry Research* **2004,** 43, (1), 74-84.

[40] Harold, M. P.; Nair, B.; Kolios, G., Hydrogen generation in a Pd membrane fuel processor: assessment of methanol-based reaction systems. *Chemical Engineering Science* **2003,** 58, (12), 2551-2571.

[41] Nair, B. K. R.; Harold, M. P., Hydrogen generation in a Pd membrane fuel processor: Productivity effects during methanol steam reforming. *Chemical Engineering Science* **2006,** 61, (19), 6616-6636.

[42] Israni, S. H.; Nair, B. K. R.; Harold, M. P., Hydrogen generation and purification in a composite Pd hollow fiber membrane reactor: Experiments and modeling. *Catalysis Today* **2009,** 139, (4), 299-311.

[43] Shu, J.; Grandjean, B. P. A.; Vanneste, A.; Kaliaguine, S., Catalytic Palladium-Based Membrane Reactors - a Review. *Canadian Journal of Chemical Engineering* **1991,** 69, (5), 1036-1060.

[44] Lin, Y. M.; Rei, M. H., Study on the hydrogen production from methanol steam reforming in supported palladium membrane reactor. *Catalysis Today* **2001,** 67, (1-3), 77-84.

[45] Gallucci, F.; Paturzo, L.; Basile, A., Hydrogen recovery from methanol steam reforming in a dense membrane reactor: Simulation study. *Industrial & Engineering Chemistry Research* **2004,** 43, (10), 2420-2432.

[46] Yu, X. H.; Tu, S. T.; Wang, Z. D.; Qi, Y. S., On-board production of hydrogen for fuel cells over Cu/ZnO/Al2O3 catalyst coating in a micro-channel reactor. *Journal of Power Sources* **2005,** 150, 57-66.

[47] Karim, A.; Bravo, J.; Gorm, D.; Conant, T.; Datye, A., Comparison of wall-coated and packed-bed reactors for steam reforming of methanol. *Catalysis Today* **2005,** 110, (1-2), 86-91.

[48] Pan, L. W.; Wang, S. D., Methanol steam reforming in a compact plate-fin reformer for fuel-cell systems. *International Journal of Hydrogen Energy* **2005,** 30, (9), 973-979.

[49] de Wild, P. J.; Verhaak, M. J. F. M., Catalytic production of hydrogen from methanol. *Catalysis Today* **2000,** 60, (1-2), 3-10.

[50] Arana, L. R.; Schaevitz, S. B.; Franz, A. J.; Schmidt, M. A.; Jensen, K. F., A microfabricated suspended-tube chemical reactor for thermally efficient fuel processing. *Journal of Microelectromechanical Systems* **2003,** 12, (5), 600-612.

[51] Kaisare, N. S.; Stefanidis, G. D.; Vlachos, D. G., Millisecond Production of Hydrogen from Alternative, High Hydrogen Density Fuels in a Cocurrent Multifunctional Microreactor. *Industrial & Engineering Chemistry Research* **2009,** 48, (4), 1749-1760.

[52] Salge, J. R.; Dreyer, B. J.; Dauenhauer, P. J.; Schmidt, L. D., Renewable hydrogen from nonvolatile fuels by reactive flash volatilization. *Science* **2006,** 314, (5800), 801-804.

[53] Ahmed, S.; Krumpelt, M., Hydrogen from hydrocarbon fuels for fuel cells. *International Journal of Hydrogen Energy* **2001,** 26, (4), 291-301.

[54] Froment, G. F.; Bischoff, K. B., *Chemical reactor analysis and design*. Wiley: 1979.

[55] Deluga, G. A.; Salge, J. R.; Schmidt, L. D.; Verykios, X. E., Renewable hydrogen from ethanol by autothermal reforming. *Science* **2004,** 303, (5660), 993-997.

[56] Fedorov, A. G., Varady, M., and Degertekin, F. L. Droplet Impingement Chemical Reactors and Methods of Processing Fuel. U.S. Patent No. 7,909,897, 2011.

[57] Anderson, D. M.; Kottke, P. A.; Fedorov, A. G., Thermodynamic analysis of hydrogen production via sorption-enhanced steam methane reforming in a new class of variable volume batch-membrane reactor. *International Journal of Hydrogen Energy* **2014,** 39, (31), 17985-17997.

[58] Fedorov, A. G. a. D., D. L. Hydrogen-Generating Reactors and Methods. U.S. Patent No. 7,981,171, 2011.

[59] Varanasi, K. K.; Clack, H. L.; Miller, R. S., On preferential diffusion of binary component liquid droplets evaporating in a two-phase mixing layer. *International Journal of Multiphase Flow* **2004,** 30, (10), 1235-1257.

[60] Alleborn, N.; Raszillier, H., Spreading and sorption of a droplet on a porous substrate. *Chemical Engineering Science* **2004,** 59, (10), 2071-2088.

[61] Rohsenow, W. M., Rohsenow Pool-Boiling Correlation. *Journal of Heat Transfer* **1972,** 94, (2), 255-&.

[62] Berenson, P., Film-boiling heat transfer from a horizontal surface. *Journal of Heat Transfer (US)* **1961,** 83.

[63] Dunn, S., Hydrogen futures: toward a sustainable energy system. *International Journal of Hydrogen Energy* **2002,** 27, (3), 235-264.

[64] Lutz, A. E.; Bradshaw, R. W.; Keller, J. O.; Witmer, D. E., Thermodynamic analysis of hydrogen production by steam reforming. *International Journal of Hydrogen Energy* **2003,** 28, (2), 159-167.

[65] Cao, C. S.; Xia, G.; Holladay, J.; Jones, E.; Wang, Y., Kinetic studies of methanol steam reforming over Pd/ZnO catalyst using a microchannel reactor. *Applied Catalysis a-General* **2004,** 262, (1), 19-29.

[66] Asprey, S. P.; Wojciechowski, B. W.; Peppley, B. A., Kinetic studies using temperature-scanning: the steam-reforming of methanol. *Applied Catalysis a-General* **1999,** 179, (1-2), 51-70.

[67] Lee, J. K.; Ko, J. B.; Kim, D. H., Methanol steam reforming over Cu/ZnO/Al2O3 catalyst: kinetics and effectiveness factor. *Applied Catalysis a-General* **2004,** 278, (1), 25-35.

[68] Peppley, B. A.; Amphlett, J. C.; Kearns, L. M.; Mann, R. F., Methanol-steam reforming on Cu/ZnO/Al2O3 catalysts. Part 2. A comprehensive kinetic model. *Applied Catalysis a-General* **1999,** 179, (1-2), 31-49.

[69] Israni, S. H.; Harold, M. P., Methanol Steam Reforming in Pd-Ag Membrane Reactors: Effects of Reaction System Species on Transmembrane Hydrogen Flux. *Industrial & Engineering Chemistry Research* **2010,** 49, (21), 10242-10250.

[70] Turns, S., *An Introduction to Combustion: Concepts and Applications w/Software*. McGraw-Hill Companies,Incorporated: 1999.

[71] Ranz, W.; Marshall, W., Evaporation from drops. *Chem. Eng. Prog* **1952,** 48, (3), 141-146.

[72] Burelbach, J. P.; Bankoff, S. G.; Davis, S. H., Nonlinear Stability of Evaporating Condensing Liquid-Films. *Journal of Fluid Mechanics* **1988,** 195, 463-494.

[73] Bird, R. B.; Stewart, W. E.; Lightfoot, E. N., Role of Transport Phenomena in Chemical-Engineering Teaching and Research - Past, Present, and Future. *Abstracts of Papers of the American Chemical Society* **1979**, (Apr), 35-&.

[74] Chachuat, B.; Mitsos, A.; Barton, P. I., Optimal design and steady-state operation of micro power generation employing fuel cells. *Chemical Engineering Science* **2005,** 60, (16), 4535-4556.

[75] Sa, S.; Silva, H.; Sousa, J. M.; Mendes, A., Hydrogen production by methanol steam reforming in a membrane reactor: Palladium vs carbon molecular sieve membranes. *Journal of Membrane Science* **2009,** 339, (1-2), 160-170.

[76] Choi, Y.; Stenger, H. G., Water gas shift reaction kinetics and reactor modeling for fuel cell grade hydrogen. *Journal of Power Sources* **2003,** 124, (2), 432-439.

[77] Twigg, M.; Spencer, M., Deactivation of Copper Metal Catalysts for Methanol Decomposition, Methanol Steam Reforming and Methanol Synthesis. *Topics in Catalysis* **2003,** 22, (3-4), 191-203.

[78] Jewett, D.; Makrides, A., Diffusion of hydrogen through palladium and palladium-silver alloys. *Trans. Faraday Soc.* **1965,** 61, 932-939.

[79] Uemiya, S.; Matsuda, T.; Kikuchi, E., Hydrogen Permeable Palladium Silver Alloy Membrane Supported on Porous Ceramics. *Journal of Membrane Science* **1991,** 56, (3), 315-325.

[80] Basford, J. A.; Boeckmann, M. D.; Ellefson, R. E.; Filippelli, A. R.; Holkeboer, D. H.; Lieszkovszky, L.; Stupak, C. M., Recommended Practice for the Calibration of Mass Spectrometers for Partial-Pressure Analysis. *Journal of Vacuum Science & Technology a-Vacuum Surfaces and Films* **1993,** 11, (3), A22-A40.

[81] Krishna, R.; Wesselingh, J. A., Review article number 50 - The Maxwell-Stefan approach to mass transfer. *Chemical Engineering Science* **1997,** 52, (6), 861-911.

[82] Bird, R. B.; Stewart, W. E.; Lightfoot, E. N., *Transport Phenomena*. Wiley: 2007.

[83] Hirschfelder, J. O.; Curtiss, C. F.; Bird, R. B.; Mayer, M. G., *Molecular theory of gases and liquids*. Wiley New York: 1954; Vol. 26.

[84] Krishna, R.; Wesselingh, J., The Maxwell-Stefan approach to mass transfer. *Chemical Engineering Science* **1997,** 52, (6), 861-911.

[85] Cheung, H.; Bromley, L. A.; Wilke, C. R., Thermal conductivity of gas mixtures. *AIChE Journal* **1962,** 8, (2), 221-228.

[86] McLeod, L. S.; Degertekin, F. L.; Fedorov, A. G., Determination of the rate-limiting mechanism for permeation of hydrogen through microfabricated palladium–silver alloy membranes. *Journal of Membrane Science* **2009,** 341, (1–2), 225-232.

[87] Yovanovich, M. M., Four decades of research on thermal contact, gap, and joint resistance in microelectronics. *Components and Packaging Technologies, IEEE Transactions on* **2005,** 28, (2), 182-206.

[88] Kays, W.; Crawford, M.; Weigand, B., *Convective Heat & Mass Transfer W/ Engineering Subscription Card*. McGraw-Hill Companies,Incorporated: 2005.

[89] Pattekar, A. V.; Kothare, M. V., A microreactor for hydrogen production in micro fuel cell applications. *Journal of Microelectromechanical Systems* **2004,** 13, (1), 7-18.

[90] de Carvalho, N. F.; Marchi, C. H.; de Toledo Perstchi, C., Methods for calculating the thermal conductivity at the control-volume surfaces. **2013**.

[91] Yun, T. M.; Kottke, P. A.; Anderson, D. M.; Fedorov, A. G., Experimental investigation of hydrogen production by variable volume membrane batch reactors with modulated liquid fuel introduction. *International Journal of Hydrogen Energy*, (0).

[92] Cussler, E. L., *Diffusion: Mass Transfer in Fluid Systems*. Cambridge University Press: 1997.

[93] Ward, T. L.; Dao, T., Model of hydrogen permeation behavior in palladium membranes. *Journal of Membrane Science* **1999,** 153, (2), 211-231.

[94] McLeod, L. S.; Degertekin, F. L.; Fedorov, A. G., Non-ideal absorption effects on hydrogen permeation through palladium-silver alloy membranes. *Journal of Membrane Science* **2009,** 339, (1-2), 109-114.

[95] McLeod, L. S.; Degertekin, F. L.; Fedorov, A. G., Determination of the rate-limiting mechanism for permeation of hydrogen through microfabricated palladium-silver alloy membranes. *Journal of Membrane Science* **2009,** 341, (1-2), 225-232.

[96] Weisz, P.; Prater, C., Interpretation of measurements in experimental catalysis. *Adv. Catal* **1954,** 6, (143), 49.

[97] Mears, D. E., Tests for Transport Limitations in Experimental Catalytic Reactors. *Industrial & Engineering Chemistry Process Design and Development* **1971,** 10, (4), 541-547.

[98] Chan, S. H.; Wang, H. M., Thermodynamic and kinetic modelling of an autothermal methanol reformer. *Journal of Power Sources* **2004,** 126, (1-2), 8-15.